INFLUENCE OF MICROSTRUCTURE IN ROLLING CONTACT FATIGUE OF BEARING STEELS WITH INCLUSIONS

A Thesis
Presented to
The Academic Faculty

By

Erick Shaw Alley

In Partial Fulfillment
Of the Requirements for the Degree
Doctor of Philosophy in Mechanical Engineering

Georgia Institute of Technology

May 2009

INFLUENCE OF MICROSTRUCTURE IN ROLLING CONTACT FATIGUE OF BEARING STEELS WITH INCLUSIONS

Approved by:

Dr. Richard W. Neu, Advisor
George W. Woodruff School
of Mechanical Engineering
Georgia Institute of Technology

Dr. David L. McDowell
George W. Woodruff School
of Mechanical Engineering
Georgia Institute of Technology

Dr. Min Zhou
George W. Woodruff School
Of Mechanical Engineering
Georgia Institute of Technology

Dr. Ken Gall
School of Materials Science
and Engineering
Georgia Institute of Technology

Dr. Arun M. Gokhale
School of Materials Science
and Engineering
Georgia Institute of Technology

Dr. E. Buddy Damm
Timken Research Center
The Timken Company

Date Approved: April 3, 2009

This thesis is dedicated to my father, Lindsey D. Alley. No better father could a son have asked for.

ACKNOWLEDGEMENTS

The author would like to express his gratitude to many who have helped make the completion of this work possible.

First, I would like to thank my advisor, Dr. Richard Neu, for his support and guidance in all phases of this research project. I would also like to thank Dr. David McDowell, Dr. Min Zhou, Dr. Arun Gokhale, Dr. Ken Gall, and Dr. E. Buddy Damm, for serving as my committee members. I would also like to thank the staff of the Woodruff School for assisting me with many logistical issues during my time at Georgia Tech, especially Cecelia Jones for travel logistics, and Terry Keita and Glenda Johnson for graduate forms and procedural guidance.

I would like to thank my fellow graduate students for both their academic assistance and their friendship. Rajesh Prassanavenkatesan helped in understanding ABAQUS material subroutines, and we have collaborated on work from this project and a project in which he has studied the fatigue behavior of gear steels. Jeremy Dawkins, Mike Hirsch, Zach Moore, Brian Nishimoto, Ming Zhang, Rob Kupkovitz, and other lab-mates have also provided me with guidance and friendship during my time here at Georgia Tech.

I would like to acknowledge the support of the NSF (I/UCRC) Center for Computational Materials Design, a joint venture of partner institutions Penn State and Georgia Tech, and our mentor, Timken Research Center. Many personnel from Timken have aided in my completion of this project, including Buddy Damm, Peter Glaws, Krich Sawamiphakdi, Matt Wilmer, Patrick Anderson, and Xiaolan Ai. This work was also

partially supported by the National Center for Supercomputing Applications under grant MSS070018N and utilized cobalt and abe.

This project would also not have been possible without the love and support of my wonderful family. My father Lindsey, mother Carolynn, and brother Kevan have provided me with much support over the years in order to give me the chance to pursue my goals. My extended family has also given me much support, and I thank Clint, Diane, Lindsey, Marisa, Julia, Caroline, Riley, Carole, Greg, Ashley, Cathleen, Julia, Taylor, Jessie, Robb, Rochelle, Big Dave, Carol, Ramsay, Noble, Alex, Marjeanne, and Norma Lee for having been there for me so many times.

I would also like to recognize my close friends who, through thick and thin, have stood by me during both good and trying times, and are like family to me: Matthew, Dale and Lori, Emily, Ken and Michelle, Andy and Jamie, Syed, Celeste, Rob, Jaimie, Tom, Dana, and Nohealani.

Most of all, I would like to thank God for all the blessings He has bestowed upon both myself and my family, and for giving me the abilities needed to complete this thesis.

TABLE OF CONTENTS

ACKNOWLEDGEMENTS iv

LIST OF TABLES ix

LIST OF FIGURES x

NOMENCLATURE xvi

SUMMARY xxvi

CHAPTER 1: INTRODUCTION 1

CHAPTER 2: BACKGROUND 6

2.1 Direction Conventions and Nomenclature 6

2.2 Microstructural Characteristics in Rolling Contact Fatigue 8

2.3 Rolling Contact Fatigue Models 12

2.3.1 Empirical Models 12

2.3.2 Finite Element Models 13

2.4 Contact Mechanics 14

2.5 Crystal Plasticity Formulation 17

2.6 Transformation Plasticity 19

2.7 Fatigue Indicator Parameters 23

CHAPTER 3: METHODOLOGY 26

3.1 Goals 26

3.2 Geometric Finite Element Models 27

3.2.1 Large-scale Model 29

3.2.2 Small-scale Volume Element Model 34

3.2.3 Sub-model 41
3.2.4 Geometric Model Testing with J_2 Plasticity 43
3.3 Advanced Material Modeling 53
3.3.1 Series 41XXX Steels 53
3.3.2 Multi-phase material representation 59
3.3.3 Two-Phase Micro-Plasticity Material Model 61
3.3.4 Algorithmic Treatment 62
3.3.4.1 Algorithm Inputs and Preliminary Calculations 65
3.3.4.2 Transformation Iterations 68
3.3.4.3 Crystal Plasticity Iterations 75
3.3.4.4 Updates for Future Time Steps and Outputs 81
3.3.5 Experimental Calibrations of Material Model 84
3.3.5.1 Virtual Test Models 85
3.3.5.2 Matching the Model to Test Data 93
3.3.5.3 Calibrated Material Parameters 104
CHAPTER 4: DEMONSTRATION CASES 107
4.1 Inclusion Orientation Effects Study 107
4.2 Retained Austenite Effects Study 116
CHAPTER 5: CONCLUSIONS 144
5.1 Advances and Innovations 144
5.2 Recommendations for Future Work 146
APPENDIX A: MARTENSITIC CRYSTAL PLASTICITY SLIP SYSTEMS 150
APPENDIX B: AUSTENITIC TRANSFORMATION SYSTEMS 152

REFERENCES 153

VITA 158

LIST OF TABLES

Table 1. Volume element mesh sizing for tetrahedral elements. 36

Table 2. Geometric model testing parameters. 44

Table 3. Stress-plastic strain points for J_2 plsaticity with linear isotropic hardening 45

Table 4. Heat treatment schedule for 41100 steels to achieve 13%, 22%, and 35% initial retained austenite. 56

Table 5. List of input parameters for UMAT. 65

Table 6. Option gcn choices 67

Table 7. User output variables at each integration point in ABAQUS. 82

Table 8. State variable storage order for each integration point 83

Table 9. Calibrated material model parameters. 104

Table 10. Dimensions of zones and mesh for inclusion orientation study. 109

Table 11. Dimensions of zones and mesh for retained austenite study 117

Table 12. Transformation parameters for each used initial volume fraction of retained austenite. 119

LIST OF FIGURES

Figure 1. Typical roller bearing assembly. 1

Figure 2. Virtual CCMD Studio..... 4

Figure 3. Coordinate system naming conventions. 6

Figure 4. Inclusion orientation nomenclature. 7

Figure 5. Butterfly wings [2]. 8

Figure 6. White etching near inclusion [53]. 9

Figure 7. Stringers of inclusions. 10

Figure 8. Microtexture and spalling for the cases of (a) 3.3 GPa at 45 ˚C for 15 x 10^8 revolutions, (b) 4.8 GPa at 55 ˚C for 2 x 10^8 revolutions, and (c) 3.3 GPa at 90 ˚C for 1 x 10^8 revolutions [56]. 11

Figure 9. Hertzian stress components as a function of x-location within the subsurface space at a given depth of y=0.5a [21]. 15

Figure 10. (a) Plastic shear stress amplitude over a roller pass, and (b) orthogonal shear stress-strain cycle over the roller pass [21]. 16

Figure 11. Crystal Plasticity Multiplicative Decomposition..... 17

Figure 12. Transformation direction and habit plane normal [16]..... 20

Figure 13. Additional applications of developed model. 27

Figure 14. Schematic depicting the relative sizes of the three model scales. 28

Figure 15. Large-scale model setup. 29

Figure 16. Contact pressure application scheme..... 30

Figure 17. Pressure strip simulated pass. 30

Figure 18. Large-scale model y-normal stress distribution. 31

Figure 19. Large-scale model Tresca stress distribution. 32

Figure 20. Tetrahedral meshing Tresca stress distribution. 33

Figure 21. Small-scale volume element scheme [21]. 35

Figure 22. Volume element load applications. 36

Figure 23. Loading application points for a simulated bearing pass. 38

Figure 24. Inclusion region in volume element model. 40

Figure 25. Plasticity region in volume element model. 41

Figure 26. Sub-model setup with non-uniform tractions applied. 42

Figure 27. Inclusion dimension nomenclature for (a) cylindrical, (b) square, and (c) rectangular inclusion shapes. 44

Figure 28. End effects of 3-D model on effective plastic strain. 46

Figure 29. ERPSI in the x-y plane for 1st, 2nd, 3rd passes for a rectangular, parallel orientation inclusion. 47

Figure 30. Effective plastic strain for rectangular parallel inclusion, cut on x and z-planes. 48

Figure 31. Effective plastic strain for cylindrical parallel inclusion, cut on x and z-planes. 48

Figure 32. In-plane plastic shear strain for rectangular parallel inclusion, after 3rd pass. 49

Figure 33. In-plane plastic shear strain for cylindrical parallel inclusion, after 3rd pass. 49

Figure 34. X-Y plastic shear strain on 35 degree angled cut, after 3rd pass. 50

Figure 35. ERPSI by shape and orientation. 51
Figure 36. Third-pass ERPSI accumulation for a vertically oriented cylindrical inclusion. 52
Figure 37. Lath martensite grain structure. 53
Figure 38. Stress-strain responses of various 41XXX steel varieties. 54
Figure 39. Micrograph of 4145 series steel. 55
Figure 40. 41100 heat treatments. 57
Figure 41. Micrograph of 41100 series steel with 13% initial retained austenite 58
Figure 42. Micrograph of 41100 series steel with 22% initial retained austenite 58
Figure 43. Micrograph of 41100 series steel with 35% initial retained austenite 59
Figure 44. Hierarchy of iterations containing transform and plasticity. 62
Figure 45. Flow diagram for user material routine UMAT. 64
Figure 46. Euler angle definitions between local lattice coordinates and global coordinates. 66
Figure 47. Orientation scheme for virtual test model. 85
Figure 48. Periodic boundary condition scheme 87
Figure 49. Effective total strain distribution at 1% total strain in a sample containing 35% initial RA during virtual tensile test 89
Figure 50. Volume fraction transformation at 1% total strain in a sample containing 35% initial RA during virtual tensile test 90
Figure 51. Virtual shear test model setup. 91
Figure 52. Effective inelastic strain distribution at 2.5% simple shear strain in a sample containing 35% initial RA during virtual shear test. 92

Figure 53. Volume fraction evolution at 2.5% simple shear strain in a sample containing 35% initial RA during virtual shear test..... 93
Figure 54. Calibration of 4145 steel. 95
Figure 55. Two-phase crystal plasticity model calibration to 41100 steel containing different amounts of retained austenite..... 97
Figure 56. Volumetric transform strain comparison for 41100 steel..... 98
Figure 57. Volume fraction transform amounts of the virtual test models..... 100
Figure 58. Compression response of 41100 steel with different amounts of retained austenite. 101
Figure 59. Simple shear test of the virtual models..... 103
Figure 60. Critical driving stress - initial volume fraction relationship..... 105
Figure 61. Transform hardening coefficient - initial volume fraction relationship. 106
Figure 62. Out-of-plane inclusion orientation for the orientation effect study..... 108
Figure 63. Equivalent plastic strain accumulation over three passes for (a) 15 degrees, (b) 30 degrees, (c) 45 degrees, (d) 60 degrees, (e) 75 degrees, and (f) 90 degrees orientations..... 111
Figure 64. Third-pass ERPSI for (a) 15 degrees, (b) 30 degrees, (c) 45 degrees, (d) 60 degrees, (e) 75 degrees, and (f) 90 degrees orientations..... 113
Figure 65. Third-pass ERPSI versus out-of-plane orientation of inclusion..... 114
Figure 66. Fatemi-Socie parameter for third pass versus out-of-plane orientation of inclusion..... 115
Figure 67. Plastic strain response for (a) J_2 fine mesh, p_0 = 2.68GPa, (b) J_2 block mesh, p_0 = 2.68GPa, (c) Crystal plasticity block mesh, p_0 = 2.026GPa. 118

Figure 68. Third-pass ERPSI for 0% initial volume fraction of retained austenite. 120
Figure 69. Third-pass ERPSI for 13% initial volume fraction of retained austenite. 121
Figure 70. Third-pass ERPSI for 22% initial volume fraction of retained austenite. 122
Figure 71. ERPSI vs. initial volume fraction of retained austenite. 123
Figure 72. Third-pass Fatemi Socie parameter for 0% initial volume fraction of retained austenite. 124
Figure 73. Third-pass Fatemi Socie parameter for 13% initial volume fraction of retained austenite. 125
Figure 74. Third-pass Fatemi Socie parameter for 22% initial volume fraction of retained austenite. 126
Figure 75. Fatemi-Socie parameter vs. initial volume fraction of retained austenite. 127
Figure 76. Volumetric transform strain for 13% initial volume fraction of retained austenite. 128
Figure 77. Volumetric transform strain for 22% initial volume fraction of retained austenite. 129
Figure 78. Volumetric transform strain vs. initial volume fraction of retained austenite. 130
Figure 79. Volume fraction transformed for 13% initial volume fraction of retained austenite. 131
Figure 80. Volume fraction transformed for 22% initial volume fraction of retained austenite. 132

Figure 81. Volume fraction transformed vs. initial volume fraction of retained austenite. 133
Figure 82. Von Mises effective residual stress for 0% initial volume fraction of retained austenite. 134
Figure 83. Von Mises effective residual stress for 13% initial volume fraction of retained austenite. 135
Figure 84. Von Mises effective residual stress for 22% initial volume fraction of retained austenite. 136
Figure 85. Von Mises effective residual stress vs. initial volume fraction of retained austenite. 137
Figure 86. Hydrostatic residual stress for 0% initial volume fraction of retained austenite for (a) x-plane normal cut view, and (b) z-plane normal cut view. 138
Figure 87. Hydrostatic residual stress for 13% initial volume fraction of retained austenite for (a) x-plane normal cut view, and (b) z-plane normal cut view. 139
Figure 88. Hydrostatic residual stress for 22% initial volume fraction of retained austenite for (a) x-plane normal cut view, and (b) z-plane normal cut view. 140
Figure 89. Hydrostatic residual stress vs. initial volume fraction of retained austenite. 141
Figure 90. Carbon content variation scheme for possible use with the sub-model. 147

NOMENCLATURE

Abbreviations

2-D	Two-dimensional
3-D	Three-dimensional
ECPSR	Effective cyclic plastic strain range
ERPSI	Effective ratcheting plastic strain increment
FE	Finite element
FIP	Fatigue indicator parameter
FSP	Fatemi-Socie parameter
RA	Retained austenite
RCF	Rolling contact fatigue
VF	Volume fraction

Symbols (English)

A_{dir}	Kinematic hardening coefficient
A_{dyn}	Dynamic recovery coefficient
a	Half-contact width
a_1	Life-adjustment factor for probability of failure
a_2	Life-adjustment factor for bearing steel cleanliness
a_3	Life-adjustment factor for lubrication
b	Fatigue strength exponent
$\underset{\sim}{\hat{b}}_L^{(\alpha)}$	Transformation direction vector in local coordinates

$\hat{\underset{\sim}{b}}_0^{(\lambda)}$	Transformation direction vector in intermediate configuration
$\hat{\underset{\sim}{b}}^{(\lambda)}$	Transformation direction vector in current configuration
$\hat{\underset{\sim}{b}}_t^{(\alpha)}$	Transformation direction vector at previous time step
$\hat{\underset{\sim}{b}}_{t+\Delta t}^{(\alpha)}$	Transformation direction vector at current time step
C	Load corresponding to L_{10} life
$\underset{\sim}{C}$	Elastic stiffness tensor in global coordinates
$\underset{\sim}{C}^0$	Elastic stiffness tensor in local coordinates
C_{11}^0	Elastic stiffness constant
C_{12}^0	Elastic stiffness constant
C_{44}^0	Elastic stiffness constant
c	Ductility exponent
$\underset{\sim}{D}$	Rate of total deformation
$\underset{\sim}{D}^e$	Rate of elastic deformation
$\underset{\sim}{D}^p$	Rate of plastic deformation
$\underset{\sim}{D}^{tr}$	Rate of transform deformation
E_{base}	Young's modulus of base metal
E_{incl}	Young's modulus of inclusion
$\underset{\sim}{E}$	Total strain tensor
$\dot{\underset{\sim}{E}}$	Total strain tensor rate of change
$\Delta\underset{\sim}{E}$	Change in total strain tensor

$\underset{\sim}{E}^{el}$	Elastic strain tensor
$\underset{\sim}{E}^{e}_{t}$	Elastic strain tensor at previous time step
$\underset{\sim}{E}^{e}_{t+\Delta t}$	Elastic strain tensor at current time step
$\underset{\sim}{E}^{ie}$	Total inelastic strain tensor
$\underset{\sim}{E}^{p}$	Martensitic crystal plastic strain tensor
$\underset{\sim}{E}^{p}_{t}$	Martensitic crystal plastic strain tensor at previous time step
$\underset{\sim}{E}^{p}_{t+\Delta t}$	Martensitic crystal plastic strain tensor at current time step
$\underset{\sim}{E}^{tr}$	Transform strain tensor
$\underset{\sim}{E}^{tr}_{t}$	Transform strain tensor at previous time step
$\underset{\sim}{E}^{tr}_{t+\Delta t}$	Transform strain tensor at current time step
$Err_{1}^{(\lambda)}$	Error function one
$Err_{2}^{(\lambda)}$	Error function two
$\underset{\sim}{F}$	Total deformation gradient
$\underset{\sim}{F}_{t}$	Total deformation gradient at previous time step
$\underset{\sim}{F}_{t+\Delta t}$	Total deformation gradient at current time step
$\underset{\sim}{F}^{e}$	Elastic deformation gradient
$\underset{\sim}{F}^{e}_{t}$	Elastic deformation gradient at previous time step
$\underset{\sim}{F}^{e}_{t+\Delta t}$	Elastic deformation gradient at current time step
$\underset{\sim}{F}^{p}$	Martensitic crystal plastic deformation gradient

$\underset{\sim}{F}_t^p$	Martensitic crystal plastic deformation gradient at previous time step
$\underset{\sim}{F}_{t+\Delta t}^p$	Martensitic crystal plastic deformation gradient at current time step
$\dot{\underset{\sim}{F}}^p$	Martensitic crystal plastic deformation gradient rate of change
$\underset{\sim}{F}^{tr}$	Transformation deformation gradient
$\underset{\sim}{F}_t^{tr}$	Transformation deformation gradient at previous time step
$\underset{\sim}{F}_{t+\Delta t}^{tr}$	Transformation deformation gradient at current time step
$\dot{\underset{\sim}{F}}^{tr}$	Transformation deformation gradient rate of change
$f_{cr}^{(\lambda)}$	Critical driving stress
$\left(f_{cr}^{(\lambda)}\right)_0$	Initial critical driving stress
$\dot{f}_{cr}^{(\lambda)}$	Critical driving stress rate of change
$\left(f_{cr}^{(\lambda)}\right)_t$	Critical driving stress rate of change at previous time step
$\left(f_{cr}^{(\lambda)}\right)_{t+\Delta t}$	Critical driving stress rate of change at current time step
$f_{tr}^{(\lambda)}$	Driving stress
$\left(f_{tr}^{(\lambda)}\right)_t$	Driving stress at previous time step
$\left(f_{tr}^{(\lambda)}\right)_{t+\Delta t}$	Driving stress at current time step
G	Shear modulus
$g^{(\alpha)}$	Drag stress
$g_0^{(\alpha)}$	Initial drag stress
$g_t^{(\alpha)}$	Drag stress at previous time step

$g^{(\alpha)}_{t+\Delta t}$	Drag stress at current time step
$\dot{g}^{(\alpha)}$	Drag stress rate of change
gcn	Grain control number
H_{dir}	Direct isotropic hardening parameter
H_{dyn}	Dynamic recovery coefficient
i	Direction index 1…3
j	Direction index 1…3
k	Fitting parameter
L	Fatigue life
$\underset{\sim}{L}^{P}_{0}$	Plastic velocity gradient tensor
L_{10}	Life span associated with 90% reliability
m	Strain rate sensitivity exponent
$\underset{\sim}{m}^{(\alpha)}_{L}$	Slip plane normal direction vector in local coordinates
$\underset{\sim}{m}^{(\alpha)}_{0}$	Slip plane normal direction vector in intermediate configuration
$\underset{\sim}{m}^{(\alpha)}$	Slip plane normal direction vector in current configuration
$\underset{\sim}{m}^{(\alpha)}_{t}$	Slip plane normal direction vector at previous time step
$\underset{\sim}{m}^{(\alpha)}_{t+\Delta t}$	Slip plane normal direction vector at current time step
$\underset{\sim}{N}$	Geometric face normal vector
N_f	Number of cycles to initiate a given crack length
N_{slip}	Number of slip systems
N_{trans}	Number of transformation systems

n	Bearing type factor
n, $n+1$	Iteration number
$\underset{\sim}{n}_{L}^{(\alpha)}$	Habit plane normal vector in local coordinates
$\underset{\sim}{n}_{0}^{(\lambda)}$	Habit plane normal vector in intermediate configuration
$\underset{\sim}{n}^{(\lambda)}$	Habit plane normal vector in current configuration
$\underset{\sim}{n}_{t}^{(\alpha)}$	Habit plane normal vector at previous time step
$\underset{\sim}{n}_{t+\Delta t}^{(\alpha)}$	Habit plane normal vector at current time step
P	Applied load
P_{FS}	Fatemi-Socie parameter
P_{ratch}	Ratcheting parameter
p_0	Peak contact pressure
$p(x)$	Pressure in contact region
Q	Direct hardening parameter of transformation
$\underset{\sim}{R}$	Rotation matrix
$RA_{initial}$	Initial volume fraction of retained austenite
$\underset{\sim}{S}_{t}^{PK}$	Second Piola-Kirchoff stress at previous time step
$\underset{\sim}{S}_{t+\Delta t}^{PK}$	Second Piola-Kirchoff stress at current time step
$\underset{\sim}{s}_{L}^{(\alpha)}$	Slip direction vector in local coordinates
$\underset{\sim}{s}_{0}^{(\alpha)}$	Slip direction vector in intermediate configuration
$\underset{\sim}{s}^{(\alpha)}$	Slip direction vector in current configuration
$\underset{\sim}{s}_{t}^{(\alpha)}$	Slip direction vector at previous time step

$\underset{\sim}{s}^{(\alpha)}_{t+\Delta t}$	Slip direction vector at current time step
SSE_1	Scaled error norm one
SSE_2	Scaled error norm two
SSE_{Ref}	Reference scaled error norm
t	Subscript denoting previous time step
$t+\Delta t$	Subscript denoting current time step
$\underset{\sim}{t}$	Traction vector
Δt	Time step duration
V_{trans}	Total volume fraction transformed
$\left(V_{trans}\right)_t$	Total volume fraction transformed at previous time step
$\left(V_{trans}\right)_{t+\Delta t}$	Total volume fraction transformed at current time step
$\dot{V}_{trans}$	Total volume fraction transform rate
x	Rolling direction variable
y	Depth direction variable
z	Roller axis direction variable

Symbols (Greek)

α	Slip systems 1…48
β	Slip systems 1…48
$\dot{\gamma}^{(\alpha)}$	Shearing rate
$\dot{\gamma}^{(\alpha)}_{try}$	Shearing rate initial guess

$\left(\dot{\gamma}_{try}^{(\alpha)}\right)_n$	Shearing rate guess for the previous iteration
$\left(\dot{\gamma}_{try}^{(\alpha)}\right)_{n+1}$	Shearing rate guess for the current iteration
$\dot{\gamma}_{max}$	Maximum $\left\|\dot{\gamma}_{try}^{(\alpha)}\right\|$ for the current iteration
$\Delta\gamma^{(\alpha)}$	Change in shearing strain
$\dot{\gamma}_0$	Shearing rate coefficient
γ_T	Shape strain magnitude
γ_f'	Ductility coefficient
$\frac{\Delta\gamma_{max}^p}{2}$	Maximum plastic shear strain amplitude for the cycle
$\left(\Delta\gamma_{max}^p\right)_{ratch}$	Maximum ratcheting shear strain
$\delta_{\alpha\beta}$	Kronecker delta
ε_{ij}^p	Plastic strain components
$\left(\Delta\varepsilon_{ij}^p\right)_{cyc}$	Reversed cyclic plastic strain range
$\Delta\varepsilon_{cyc,eff}^p$	Effective cyclic plastic strain range (ECPSR)
$\left(\Delta\varepsilon_{ij}^p\right)_{max}$	Maximum change in plastic strain components over a cycle
$\left(\Delta\varepsilon_{ij}^p\right)_{ratch}$	Ratcheting plastic strain increment components
$\Delta\varepsilon_{ratch,eff}^p$	Effective ratcheting plastic strain increment (ERPSI)
η	Transformation systems 1…24
θ_{euler}	Second Euler angle
λ	Transformation systems 1…24

ν	Poisson ratio
ν_{base}	Poisson ratio of base metal
ν_{incl}	Poisson ratio of inclusion
ν_{tr}	Transform viscosity parameter
$\xi^{(\lambda)}$	Volume fraction transformed
$\xi_t^{(\lambda)}$	Volume fraction transformed at previous time step
$\xi_{t+\Delta t}^{(\lambda)}$	Volume fraction transformed at current time step
$\dot{\xi}^{(\lambda)}$	Volume fraction transformation rate
$\dot{\xi}_{try}^{(\lambda)}$	Volume fraction transformation rate initial guess
$\left(\dot{\xi}_{try}^{(\lambda)}\right)_n$	Volume fraction transformation rate guess for the previous iteration
$\left(\dot{\xi}_{try}^{(\lambda)}\right)_{n+1}$	Volume fraction transformation rate guess for the current iteration
$\dot{\xi}_{big}$	Maximum $\dot{\xi}_{try}^{(\lambda)}$ for the current iteration
$\dot{\xi}_{max}$	Maximum transformation rate
$\Delta\xi^{(\lambda)}$	Change in volume fraction transformed
$\underset{\sim}{\sigma}$	Cauchy stress tensor
$\dot{\underset{\sim}{\sigma}}$	Cauchy stress rate tensor
$\Delta\underset{\sim}{\sigma}$	Change in Cauchy stress tensor
$\underset{\sim}{\sigma}_t$	Cauchy stress tensor at previous time step
$\underset{\sim}{\sigma}_{t+\Delta t}$	Cauchy stress tensor at current time step
$\underset{\sim}{\sigma}_G$	Stress in global coordinates

σ_n^{max}	Maximum normal stress
$\underset{\sim}{\sigma}_{VE}$	Stress in the volume element rotated coordinates
σ_y	Yield stress
σ_{xx}	X-direction normal stress
σ_{xy}	X-y direction shear stress
σ_{yy}	Y-direction normal stress
σ_{zz}	Z-direction normal stress
$\tau^{(\alpha)}$	Resolved shear stress
$\tau_t^{(\alpha)}$	Resolved shear stress at previous time step
$\tau_{t+\Delta t}^{(\alpha)}$	Resolved shear stress at current time step
τ_f'	Fatigue strength coefficient
φ_{euler}	First Euler angle
$\chi^{(\alpha)}$	Back stress
$\chi_0^{(\alpha)}$	Initial back stress
$\chi_t^{(\alpha)}$	Back stress at previous time step
$\chi_{t+\Delta t}^{(\alpha)}$	Back stress at current time step
$\dot{\chi}^{(\alpha)}$	Back stress rate of change
ψ_{euler}	Third Euler angle
Ω	Taylor series angular term

SUMMARY

The use of bearings can be found in virtually all aspects of mechanical systems today. Reliability of these critical components is an important issue. Fatigue performance of bearings is a function of many factors, including service conditions, loading, material properties, environmental factors, and manufacturing processes. Crack nucleation, first spall generation and spall growth in rolling contact fatigue (RCF) are known to be highly sensitive to the heterogeneity of the microstructure. Yet the current state-of-the-art in the design of high performance bearing materials and microstructures is highly empirical requiring substantial lengthy experimental testing to validate the reliability and performance of these new materials and processes. The approach presented here is designed to determine the relative rolling contact fatigue performance as a function of microstructural attributes. Both an efficient geometric finite element model and an advanced two-phase material model were developed to address this complex problem.

A fully three-dimensional finite element modeling allows for end effects to be captured that were not previously possible with two-dimensional plane-strain models, providing for a more realistic assessment of inclusion morphology and arbitrary orientations. The scaling of the finite element models has been optimized to capture the cyclic microplasticity around a modeled inclusion accurately and efficiently. To achieve this, two scales of geometric models were developed to incorporate different sized microstructural phenomena, with both models using traction boundary conditions derived from Hertzian contact stresses.

A microstructure-sensitive material model adds additional capability. A hybrid model that includes both martensite and austenite phases with additional internal state variable to track the volume fraction of retained austenite due to stress-assisted transformation were developed. This represents an advance over previous models where transform plasticity and crystal plasticity were not simultaneously accounted for in a homogenized element containing both phases.

Important links between microstructural features and fatigue indicator parameters (and thus relative fatigue performance) were determined. Demonstration cases show the relationship between inclusion orientation and relative fatigue performance, allowing for the identification of critical angles which maximize fatigue and reduce performance. An additional case study showed that increasing initial volume fraction of retained austenite reduces relative fatigue life. The tools developed allow for investigations of the influence of many microstructural aspects on relative fatigue performance with a numerical model that were not previously possible.

CHAPTER 1: INTRODUCTION

Bearings are an integral component in many mechanical systems. Almost any device with moving parts relies on bearings for friction reduction and smoothness of operation. Due to the crucial nature of such parts, reliability is of paramount importance. Bearing manufacturers must produce a long-lasting bearing at the lowest possible production cost. Fatigue performance of bearings is a function of many factors, including service conditions, loading, material properties, environmental factors, and manufacturing processes.

Figure 1. Typical roller bearing assembly.

During material production, the formation of inclusions is common in bearing steels. Their distribution can vary greatly from supplier to supplier, and orientations are affected by the flow of material during processing. Bearing manufacturers must choose between costlier suppliers with the cleanest steels, and cheaper sources with more inclusions. Empirical relationships between the cleanliness of bearing steels and fatigue life have been created previously with experimental data. However, experimental work on bearing fatigue can be costly and take long amounts of time to complete, and thus it desirable to have a numerical model for predicting plastic damage due to inclusions of varying location, size, and orientation. With a numerical model, many different cases can be tested efficiently.

Previous work in numerical modeling of inclusions has been conducted in two dimensions, but based on indications from historical experience with inclusion-related bearing fatigue life data it is believed that out-of-plane orientations of the long axis of elongated inclusions are associated with minimum bearing life. Inclusions of this type cannot be modeled in a two-dimensional context due to asymmetry, and a three-dimensional modeling technique is required to study arbitrary inclusion orientations relative to the contact surface.

Most bearings are designed against their intended load to remain well within the elastic range, assuming a homogeneous, pure material. Stress concentrations caused by inclusions raise the maximum stress, but often it is not high enough to predict plastic behavior with the J_2 plasticity formulation. However, at the microscopic level, the

material is heterogeneous, containing inclusions, either hard (e.g., Al_2O_3, TiN) or soft (e.g., MnS) non-metallic inclusions, primary carbides, multiple phases (martensite and small amounts of retained austenite, bainite patches), as well as crystallographic features associated with each phase [26,36]. Therefore, it is of interest to understand the plastic behavior occurring due to presence of inclusions, which is controlled by cyclic microplasticity. In order to model the complex hierarchical microstructure of lath martensite which is commonly observed in heat-treated bearing steels, a crystal plasticity material model must be employed local to the inclusion. In addition, it is of interest in steels with significant content of retained austenite to account for the volumetric transformation strain caused by austenite-martensite transformations under loading. Thus a two-phase model is employed to account for both transformation and damage plasticity phenomena. Calibrated with uniaxial cyclic loading experiments conducted on specimens, the model is a useful tool in computing candidate driving forces phenomena such as spall and fatigue crack formation/growth, which depend on microstructural features. Fatigue indicator parameters motivated by critical plane multi-axial fatigue approaches can then be used to study the relative influence of different microstructure attributes on fatigue life. This project focuses on the analysis of a bearing steel containing explicit microstructure attributes at some depth below the contact surface. Recent work performed by Prasannavenkatesan and co-workers [42,61] on gear steels has demonstrated the potential of such focus on microstructure in investigation of fatigue performance, and also serves as inspiration for this work in bearing steel.

This work was performed under the Center for Computational Materials Design (CCMD). The Center's goal is to create a virtual studio of materials design tools. This project fits into that overall goal by developing structure-property simulation tools to enable the design of fatigue and fracture-resistant surfaces and coating systems capturing influence of crystallographic grain size, morphology, and orientation (i.e., microtexture), second phase particles and colonies in industrial-relevant polycrystalline alloys. The project involves both material and finite element models, which feed into the structure-property-performance-analysis portion of the virtual studio, as well as performance metrics such as fatigue indicator parameters, as depicted in Figure 2. The models receive inputs from experimental data performed by both Timken and Georgia Institute of Technology. In the future, alternatives and supplements to experimental inputs based on lower length scale modeling may be used to further capture the underlying physical mechanisms that affect performance.

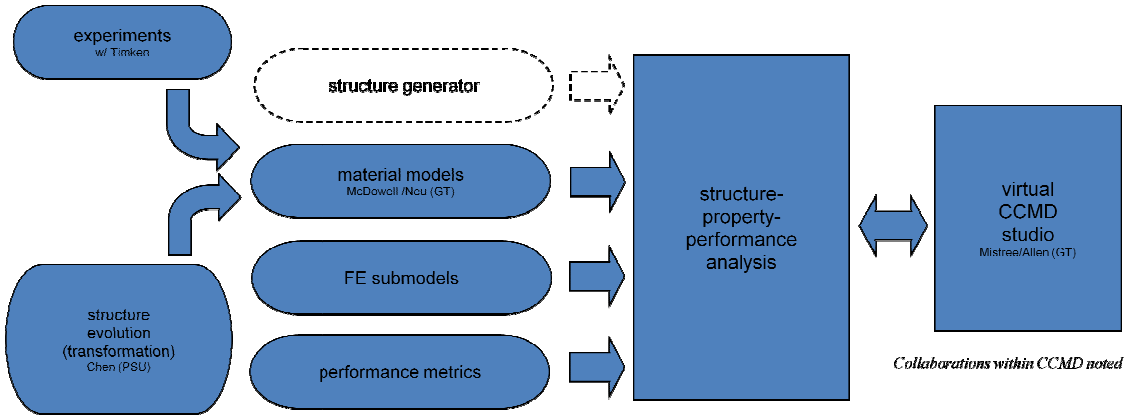

Figure 2. Virtual CCMD Studio.

The model was validated for the rolling contact fatigue case, but it can be used for many other applications such as gear problems, which incorporate both normal contact

and frictional sliding. The geometric model developed can also support other material models including microstructural transformations, crack, and carbon content variations with depth. Another area of application within the CCMD is the Air Force Research Lab's interest in the heat treatment of carburized stainless bearing steels such as Pyrowear 675 [58]. Checking microstructural attributes' effects on fatigue performance via a numerical model would greatly enhance the ability to make heat treatment decisions on new alloy systems. The modularity of the tools developed makes them an invaluable part of the CCMD.

CHAPTER 2: BACKGROUND

In order to create an effective tool for rolling contact fatigue simulations, understanding in several key areas are necessary. Microstructural characteristics, current fatigue models, and material constitutive formulations are all key components in building an improved finite element simulation tool.

2.1 Direction Conventions and Nomenclature

Before proceeding further, an understanding of the coordinate system conventions and naming will be explained. The rolling direction, or direction in which the bearing travels along the race, is the x-axis. The long axis of the roller is defined as the z-direction, and the contact normal direction, vertically oriented, is the y axis, as depicted in Figure 3.

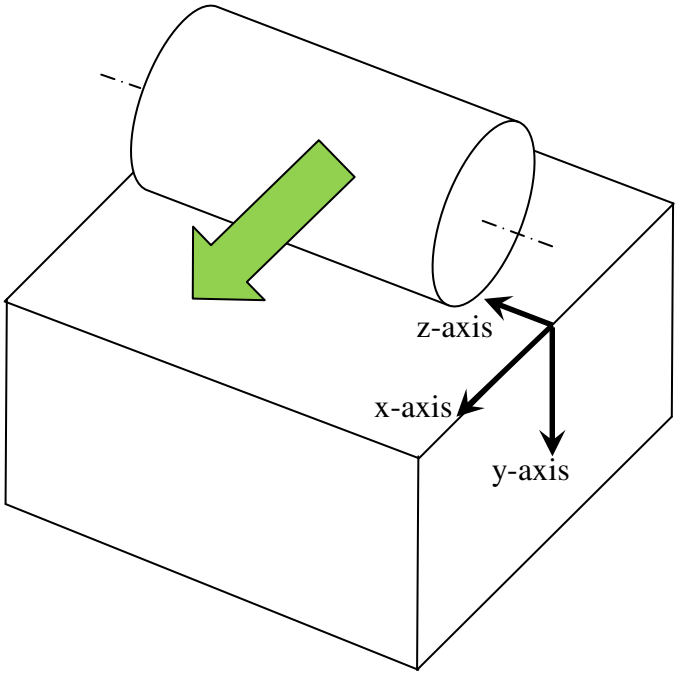

Figure 3. Coordinate system naming conventions.

When referring to inclusions, the long axis is often used to identify its orientation. Inclusions with long axes along the z-axis, or direction of the roller axis, are referred to as parallel, while those aligned with the rolling, or x-direction, are referred to as horizontal. Vertically oriented inclusions, aligned with the y-axis are simply called vertical, as depicted in Figure 4.

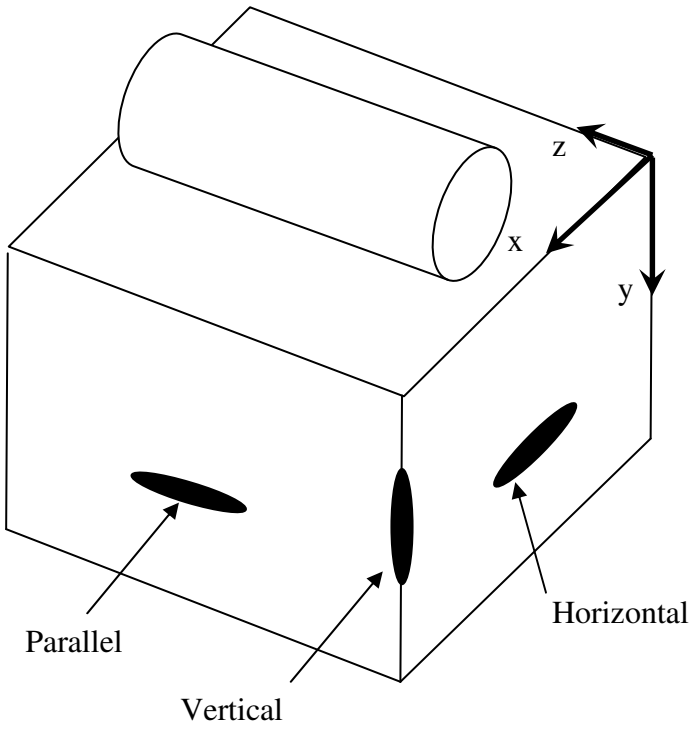

Figure 4. Inclusion orientation nomenclature.

During parametric studies, the orientation of the inclusion can also be referred to by the plane in which plane its long axis may reside, if it is in one of two common planes used in orientation effects studies. Orientations at angles within the x-y plane are referred to as “in-plane”, and orientations within the y-z plane are referred to as “out-of-plane”.

2.2 Microstructural Characteristics in Rolling Contact Fatigue

There are key microstructural attributes associated with rolling contact fatigue. One such feature is that the crack formation location is subspace, and another that is common in martensitic steels is the presence of crack initiation in the direction of so-called “butterfly wings”, as seen in Figure 5 [2].

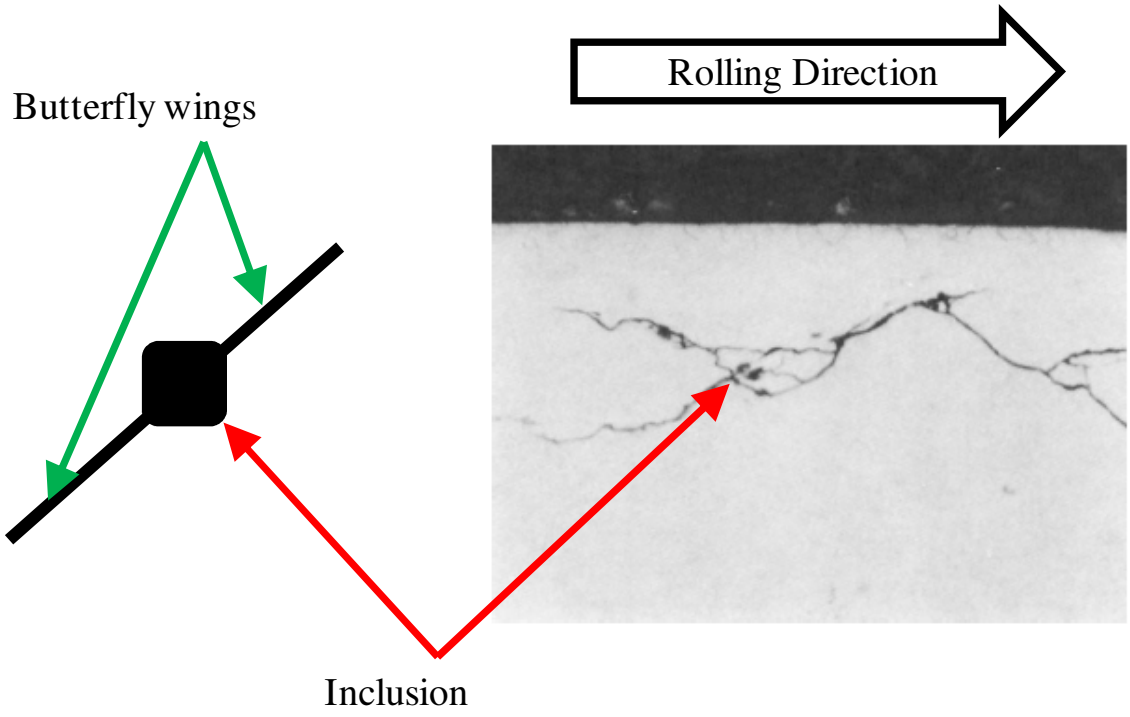

Figure 5. Butterfly wings [2].

An inclusion is most often the source of these butterfly wings, which are pockets of altered martensite microstructure, and are often found at angles as shown relative to the contact surface. This behavior is usually not found in materials with significant amounts of austenite phase yet to be transformed, as it absorbs the energy and becomes converted into martensite first [2]. The accumulation of damage near a non-metallic inclusion is caused by the differences in mechanical properties between the inclusion and

the base metal [6]. So-called white-etching areas are typically found in diagonal patterns, either in one direction or both, depending on whether the cyclic loading is reversed or not [53]. Their location along the regions of maximum shear strain (also diagonal to the inclusion) can be seen in Figure 6. Retained austenite in these regions becomes transformed as high plastic strains accumulate, forming the aforementioned pockets of altered martensitic structure.

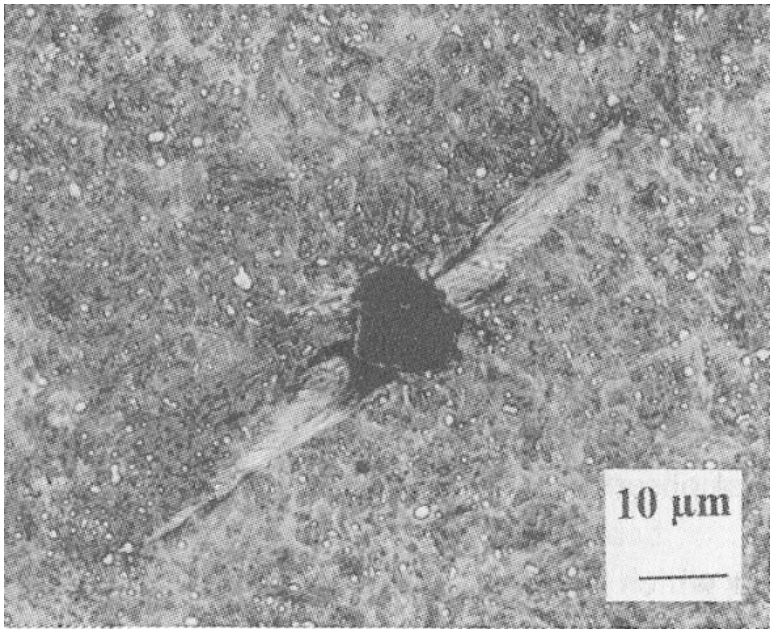

Figure 6. White etching near inclusion [53].

Inclusions can appear singly, as shown in Figure 6, or grouped together in long chains known as stringers, as shown in Figure 7. When in close proximity, these are often treated as a single, rectangular inclusion. The orientation of such stringers can have a significant effect on fatigue performance.

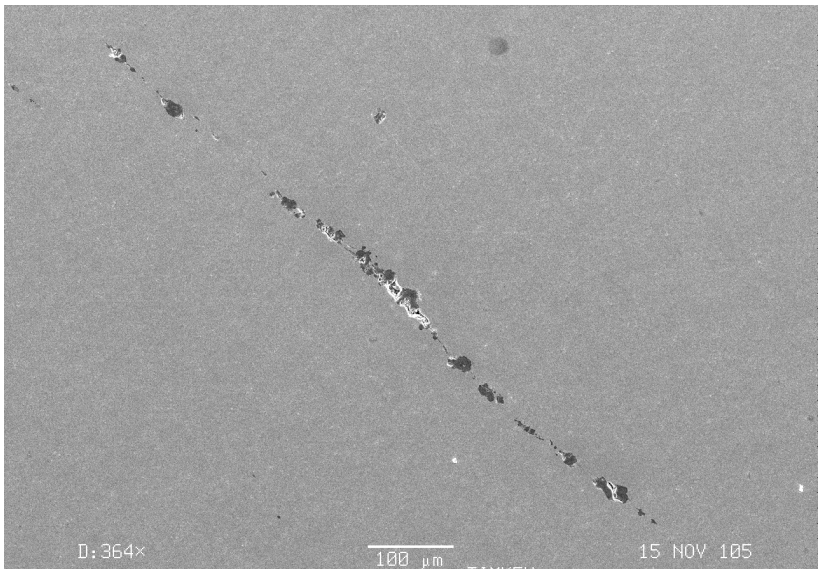

Figure 7. Stringers of inclusions.

The microtexture of the material, which can form during the service of a bearing, is dependent on loading, temperature, and number of cycles, has been shown to control spall morphology in bearings under RCF [56]. Shown in Figure 8 are spall formations, for various loading and temperature combinations. These spalls are initiated by subsurface cracks, whose orientation depends on the crystallographic orientation of the material. Note that inclusions are not always the source of such spalls; the texture of the base metal is also a determining factor in their formation, as well as temperature, number of cycles, and loading values. An elevation in temperature at the same loading can have significant effect on texture and spalling, as shown Figure 8 (a) and (c). The specimen that experienced a maximum contact pressure of 3.3 GPa at 45 ˚C for 15 x 10^8 revolutions shows no texture development or crack growth leading to spalling, whereas an elevation in temperature to 90 ˚C for 1 x 10^8 revolutions reveals {111}<211> dominated texture and a shallow, irregular-bottomed spalls. A higher maximum contact

pressure of 4.8 GPa at 55 ˚C for 2 x 10^8 revolutions, shown in Figure 8 (b), yields a deeper spall formation of regular-bottom shape with {100}<110> texture dominant.

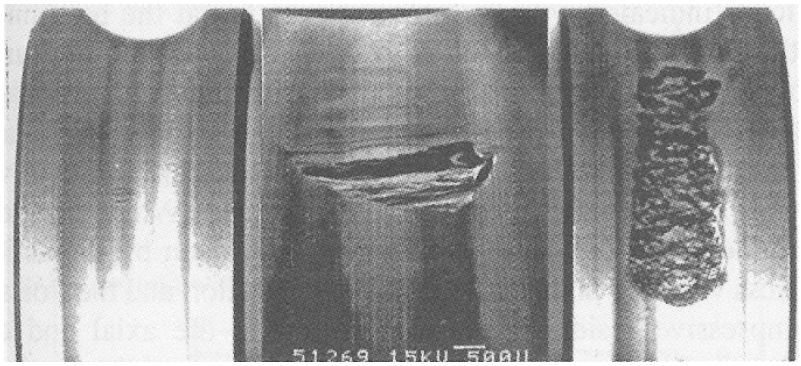

(a) (b) (c)

Figure 8. Microtexture and spalling for the cases of (a) 3.3 GPa at 45 ˚C for 15 x 10^8 revolutions, (b) 4.8 GPa at 55 ˚C for 2 x 10^8 revolutions, and (c) 3.3 GPa at 90 ˚C for 1 x 10^8 revolutions [56].

With heat treatments playing a large role in the configuration of near-surface microstructure in treated components, there is a distinct advantage to those concerned with surface treatments by having a tool available to predict effect of various microstructural characteristics (which can be controlled by processing) on fatigue performance. Heat treatment and quenching parameters were also studied for 52100 series bearing steels by Bhattacharyya et al. [8], with an experimental data approach. A key goal of this project was to allow for numerical predictive modeling of the effects of microstructural variations (such as those caused by heat treatments, for example) on a given material. The use of 41XXX steel was chosen for the demonstration case, but the methods developed herein can be applied to any variety of materials the end user would like to investigate.

2.3 Rolling Contact Fatigue Models

2.3.1 Empirical Models

Early rolling contact fatigue models have been empirically based. A classic life expectancy model used by bearing manufactures is a Weibull analysis. For a given applied force *P*, the approximate fatigue life *L* in millions of cycles can be estimated by

$$L = \left(\frac{C}{P}\right)^n \tag{1}$$

where C is the load corresponding to an L_{10} life (life span associated with 90% reliability) of one million cycles for a given geometry and loading configuration, and n is a factor that depends on the bearing type [28], either 3 for a ball bearing or 10/3 for a roller bearing. Building on this form, an empirical relationship which takes into account cleanliness of bearing steel in determining the L_{10} life is given by Equation (2) [27].

$$L_{10} = a_1 \cdot a_2 \cdot a_3 \left(\frac{C}{P}\right)^n \tag{2}$$

where a_1, a_2, and a_3 are life-adjustment factors for probability of failure, bearing steel cleanliness, and lubrication, respectively. These statistical models were created with experimental data. Since bearings are designed with long service durations in mind, physical life testing of a new bearing process or a new bearing design can take months of run time on roller bearing fatigue testing machines. The high cost of developing these tests can hinder the process, and limits the number of variants that can feasibly be tested [11]. Thus it is desirable to have a numerical model for predicting fatigue life as a function of changes in structure due to processing including the attributes of inclusions or other important features of the microstructure.

2.3.2 Finite Element Models

Previous attempts at modeling rolling contact loading with finite elements have been largely two-dimensional. A rolling contact simulation with an inclusion at varying depth and Hertzian load distribution on semi-infinite domain was performed by Raje et al. [43]. Among the results presented are stress concentrations in the bearing steel and their variation with the modulus of the inclusion and its orientation. It was shown that increasing inclusion modulus yields a higher stress concentration. Additionally, they demonstrated that inclusions oriented perpendicular to the contact surface caused higher stress concentrations than those oriented parallel to the surface [43]. Another two-dimensional analysis of inclusion effects on short crack nucleation and propagation was performed by Melander [36], in which a finite element model containing a circular inclusion was analyzed with different contact conditions (bonded, de-bonded, etc.). The work provided relationships between inclusion-metal interface conditions and the nucleation and growth of fatigue cracks [36]. They concluded that both cracks in inclusions and partial disbonding of the inclusion-matrix interface can increase the propensity for fatigue crack growth [36]. Both of these areas must be well understood to compare rolling contact fatigue performance against inclusion and microstructural characteristics. However, in order to examine the orientations of elongated inclusions that are most commonly associated with reduced bearing life, a three-dimensional model like the one developed herein is needed. Another key reason for moving to a fully three-dimensional model is the ability to capture end effects; while a plane-strain assumption for a roller bearing race is valid (the roller is long compared to the contact width), the

inclusions are not semi-infinite in length, and thus end effects in the out-of-plane direction cannot be captured without a fully three-dimensional model.

2.4 Contact Mechanics

Analytical formulation of contact between non-conforming bodies is the basis for the traction boundary conditions that this model uses. While this study concentrates on roller bearing applications, the methodology laid out can be used for ball bearing applications and gears as well. The Hertzian formulation of contact between cylinders, which can be equated to a cylinder-on-half-space equivalent, is used to calculate the stress state of a pure material at a specific depth and location [21]. Bearings typically are designed to remain in the elastic range of the material's macroscopic behavior. The formulation for elastic Hertzian contact pressure in the contact region for the body types stated is given as

$$p(x) = p_0 \cdot \sqrt{1 - \left(\frac{x}{a}\right)^2} \tag{3}$$

where p_0 is the peak pressure and a is the contact half-width. To find the stress state at a given location within the half-space body, singular integral equations must be evaluated using the pressure distribution given in Equation (3) and are given by the following:

$$\sigma_{xx} = \frac{-1}{\pi}\int_{-a}^{a} \frac{2 \cdot y \cdot (x-s)^2 \cdot p(s)}{\left[(x-s)^2 + y^2\right]} ds \tag{4}$$

$$\sigma_{yy} = \frac{-1}{\pi}\int_{-a}^{a} \frac{2 \cdot y^3 \cdot p(s)}{\left[(x-s)^2 + y^2\right]} ds \tag{5}$$

$$\sigma_{xy} = \frac{-1}{\pi}\int_{-a}^{a} \frac{2\cdot y^2\cdot(x-s)\cdot p(s)}{\left[(x-s)^2+y^2\right]}ds \tag{6}$$

$$\sigma_{zz} = \nu\cdot\left(\sigma_{xx}+\sigma_{yy}\right) \tag{7}$$

When these singular integral equations are integrated, for a given depth location the stresses vary with x-location as shown by the solid lines in Figure 9.

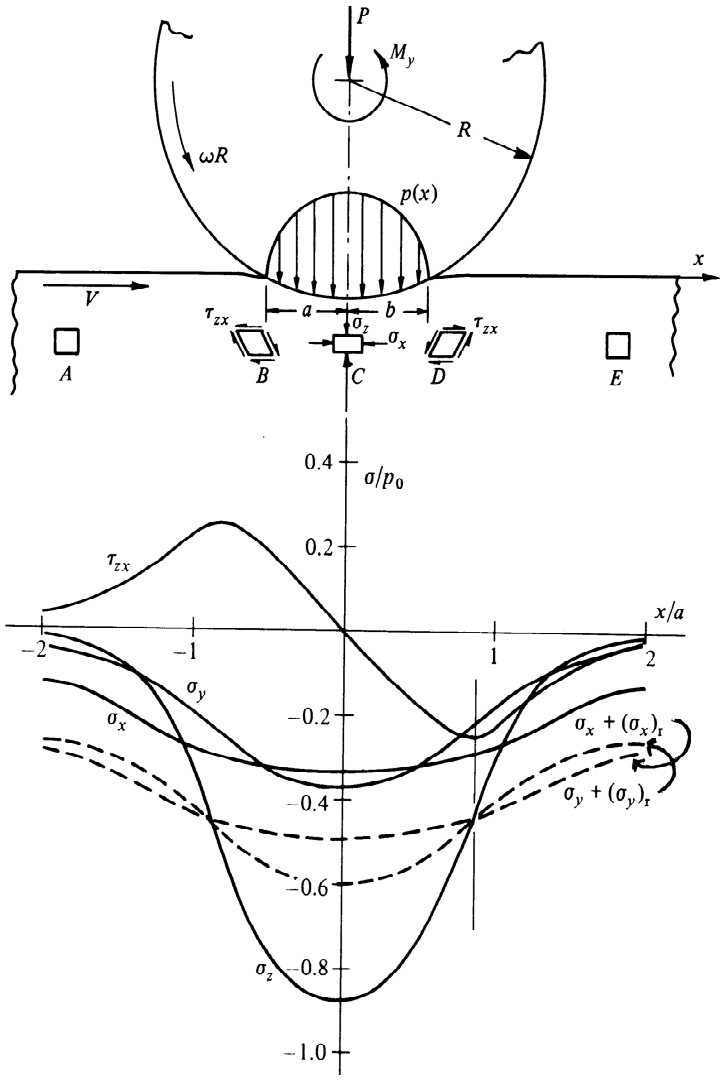

Figure 9. Hertzian stress components as a function of x-location within the subsurface space at a given depth of y=0.5a [21].

Also shown in dotted lines are the alterations in the stress field caused by a residual stress state brought on by inelastic Hertzian contact. Note the blunting of the maximum stress amplitude due to the residual stresses reached during shakedown passes. Of interest in these inelastic loading cases is the cyclic state of the subsurface stress, particularly the σ_{xy} orthogonal (or, "in-plane") shear stress. Shown in Figure 10 is the amplitude variation of the orthogonal shear stress and the orthogonal shear stress-strain behavior during inelastic Hertzian cyclic loading [21].

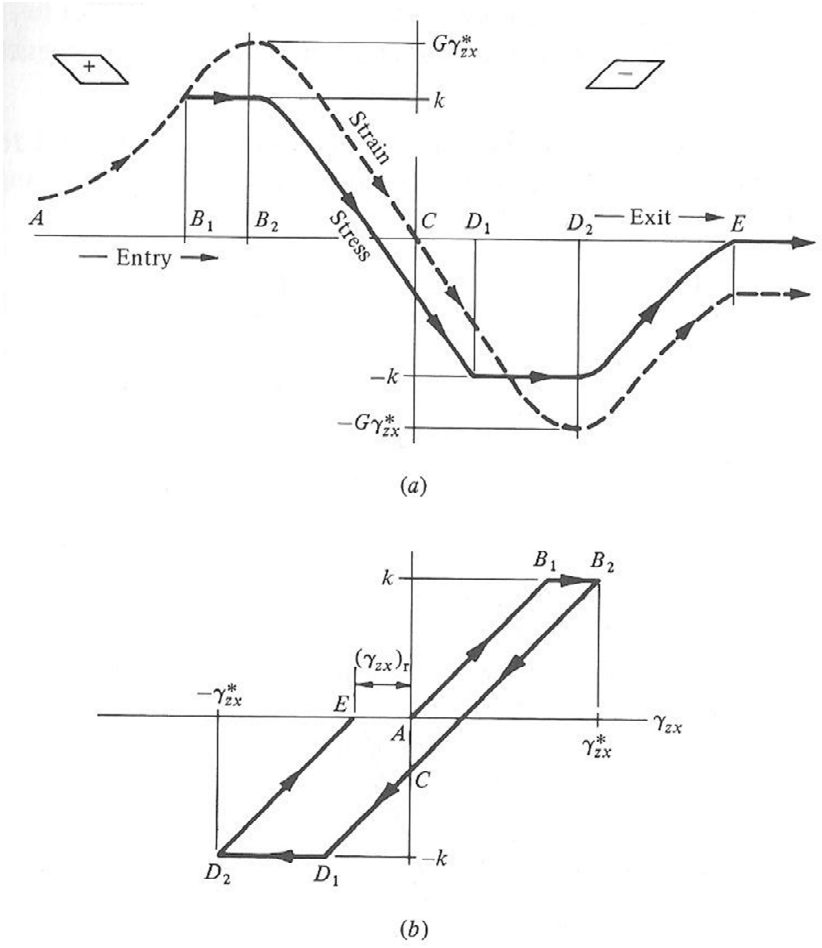

Figure 10. (a) Plastic shear stress amplitude over a roller pass, and (b) orthogonal shear stress-strain cycle over the roller pass [21].

The cyclic behavior of the orthogonal shearing makes it an important component to investigate in any inelastic loading situation.

2.5 Crystal Plasticity Formulation

Crack formation in rolling contact fatigue is controlled by cyclic microplasticity. To capture microstructural effects on fatigue performance in the model, a crystal plasticity material formulation is used. A rate-dependent model formulated by Asaro [5] and McGinty [33] was chosen. The crystal plasticity algorithm begins with the multiplicative decomposition of deformation gradient (Figure 11).

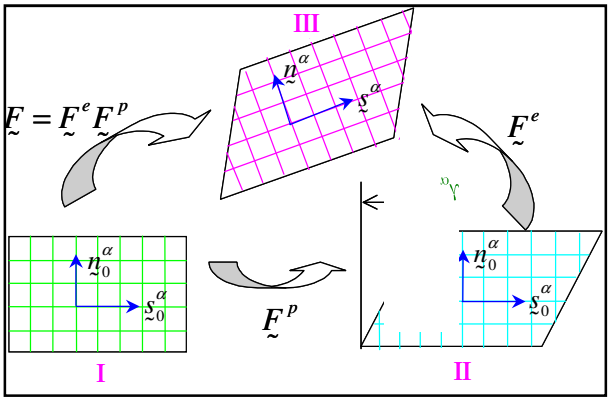

Figure 11. Crystal Plasticity Multiplicative Decomposition.

The total deformation gradient is given by

$$\underset{\sim}{F} = \underset{\sim}{F}^e \cdot \underset{\sim}{F}^p \tag{8}$$

where $\underset{\sim}{F}^e$ is the elastic deformation gradient representing the elastic stretch and rotation of lattice, and $\underset{\sim}{F}^p$ is the plastic deformation gradient describing the collective effects of dislocation motion along the active slip planes relative to a fixed lattice in the reference

configuration. Unit vectors $\underset{\sim}{s}_0^{(\alpha)}$ and $\underset{\sim}{m}_0^{(\alpha)}$ denote the slip direction vector and the slip plane normal direction vector, respectively, for the α^{th} slip system in the intermediate configuration. The values for these vectors for BCC martensite crystal plasticity are given in Appendix A. The resolved shear stress on each slip system is related to the Cauchy stress tensor according to

$$\tau^{(\alpha)} = \underset{\sim}{\sigma} : \left(\underset{\sim}{s}^{(\alpha)} \otimes \underset{\sim}{m}^{(\alpha)} \right) \tag{9}$$

where the slip direction and plane normal are rotated into the current configuration by Equations (10) and (11).

$$\underset{\sim}{s}^{(\alpha)} = \underset{\sim}{F}^{e} \cdot \underset{\sim}{s}_0^{(\alpha)} \tag{10}$$

$$\underset{\sim}{m}^{(\alpha)} = \left(\underset{\sim}{F}^{e} \right)^{-T} \cdot \underset{\sim}{m}_0^{(\alpha)} \tag{11}$$

Under the application of resolved shear stress, the shearing rates on the each slip system, $\dot{\gamma}^{(\alpha)}$, are related to the plastic velocity gradient in the intermediate configuration according to

$$\underset{\sim}{L}_0^{P} = \dot{\underset{\sim}{F}}^{p} \cdot \left(\underset{\sim}{F}^{p} \right)^{-1} = \sum_{\alpha=1}^{N_{slip}} \dot{\gamma}^{(\alpha)} \cdot \left(\underset{\sim}{s}_0^{(\alpha)} \otimes \underset{\sim}{m}_0^{(\alpha)} \right) \tag{12}$$

with $\dot{\gamma}^{(\alpha)}$ ascribed to follow the rate-dependent flow rule,

$$\dot{\gamma}^{(\alpha)} = \dot{\gamma}_0 \cdot \left| \frac{\tau^{(\alpha)} - \chi^{(\alpha)}}{g^{(\alpha)}} \right|^{m} \cdot \operatorname{sign}\left(\tau^{(\alpha)} - \chi^{(\alpha)} \right) \tag{13}$$

where $\dot{\gamma}_0$ is the shearing rate coefficient. Here, the slip systems are always active, and rate dependence is governed by m, the strain rate sensitivity exponent. High values of m can effectively make the model quasi-rate independent as desired, while still retaining the

ability to incorporate rate dependence with a lower value. The drag stress, $g^{(\alpha)}$, and the back stress, $\chi^{(\alpha)}$, on the α^{th} slip system evolve according to

$$\dot{g}^{(\alpha)} = \sum_{\beta=1}^{N_{slip}} H_{dir} \cdot \left|\dot{\gamma}^{(\beta)}\right| - g^{(\alpha)} \cdot \sum_{\beta=1}^{N_{slip}} H_{dyn} \cdot \left|\dot{\gamma}^{(\beta)}\right| \tag{14}$$

$$\dot{\chi}^{(\alpha)} = A_{dir} \cdot \dot{\gamma}^{(\alpha)} - \chi^{(\alpha)} \cdot A_{dyn} \cdot \left|\dot{\gamma}^{(\alpha)}\right| \tag{15}$$

where H_{dir} is the direct isotropic hardening coefficient, H_{dyn} is the dynamic recovery coefficient for drag stress, A_{dir} is the kinematic hardening coefficient, and A_{dyn} is the dynamic recovery coefficient for the back stress [34].

2.6 Transformation Plasticity

To explore bearing performance in multi-phase alloys, the effects of retained austenite must be considered. The austenite can promote ductility and can also induce residual stress fields due to volume expansion during the phase change. Thus, the two-phase model proposed herein must contain a formulation accounting for evolution of the volume fraction of grains, as well as the volumetric strains produced by such activity.

Austenite to martensite transformation deformation parameters can be formulated in a manner described by Gall and Sehitoglu [16], with transformation directions and habit plane normals relative to orientation of a single crystal as depicted in Figure 12.

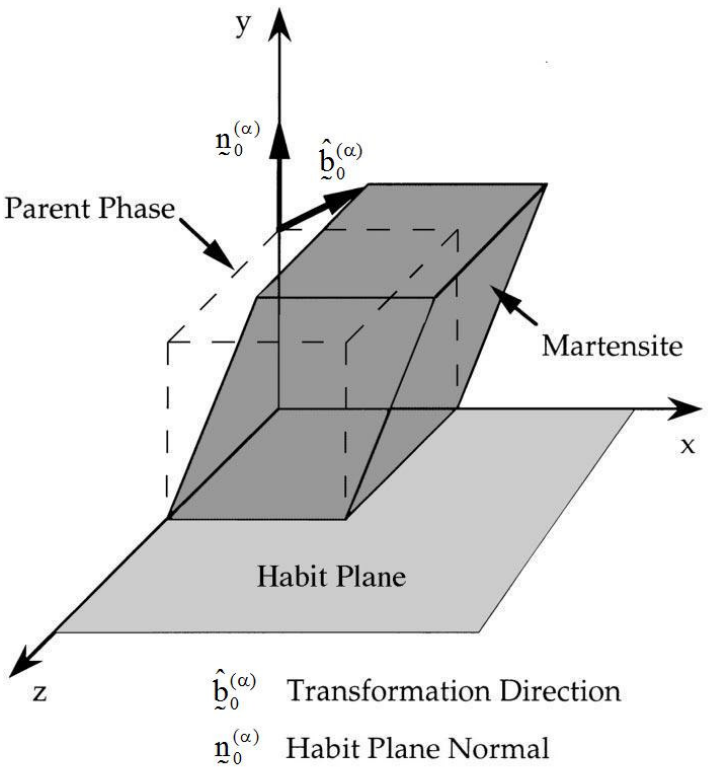

Figure 12. Transformation direction and habit plane normal [16].

In keeping with the planned microstructural formulation of the two-phase model developed in this project, the stress-assisted transformation model proposed by Suiker and Turtletaub [50] was identified as the best choice for implementing transformation. Their formulation was chosen over other formulations for steels such as that proposed by Karaman and co-workers [24] because a key feature of the model is its multiplicative decomposition, similar in formulation to that of the crystal plasticity model that will be utilized. The total deformation gradient is given by

$$\underset{\sim}{F} = \underset{\sim}{F}^{e} \cdot \underset{\sim}{F}^{tr} \tag{16}$$

where $\underset{\sim}{F}^{e}$ is the elastic deformation gradient, and $\underset{\sim}{F}^{tr}$ is the transformation deformation gradient which accounts for the volumetric expansion and shape strain of the austenite-

martensite transition, relative to the reference configuration. Unit vectors $\hat{\underset{\sim}{b}}_0^{(\lambda)}$ and $\underset{\sim}{n}_0^{(\lambda)}$ correspond to the transformation direction, also sometimes referred to as the shape strain direction, and the habit plane normal, respectively, for the λ^{th} transformation system in the intermediate configuration. The values for these vectors for an FCC austenite transformation are given in Appendix B. Transformation is said to occur when a critical driving stress on a given transformation system is reached. The driving stress $f_{tr}^{(\lambda)}$ on a transformation system λ is related to the transformation and habit vectors, and the Cauchy stress by

$$f_{tr}^{(\lambda)} = \underset{\sim}{\sigma} : \left(\gamma_T \cdot \hat{\underset{\sim}{b}}^{(\lambda)} \otimes \underset{\sim}{n}^{(\lambda)} \right) \tag{17}$$

where the transformation direction and habit plane normal are rotated into the current configuration by

$$\hat{\underset{\sim}{b}}^{(\lambda)} = \underset{\sim}{F}^e \cdot \hat{\underset{\sim}{b}}_0^{(\lambda)} \tag{18}$$

$$\underset{\sim}{n}^{(\lambda)} = \left(\underset{\sim}{F}^e \right)^{-T} \cdot \underset{\sim}{n}_0^{(\lambda)} \tag{19}$$

and γ_T is the shape strain magnitude, a parameter which is uniform for all transformation systems. When the driving stress in Equation (17) exceeds the critical driving stress $f_{cr}^{(\lambda)}$ for the transformation system, the rate of volume fraction transformation $\dot{\xi}^{(\lambda)}$ on that system is given by

$$\dot{\xi}^{(\lambda)} = \dot{\xi}_{max} \cdot \tanh\left(\frac{1}{\nu_{tr}} \cdot \frac{\left\langle f_{tr}^{(\lambda)} - f_{cr}^{(\lambda)} \right\rangle}{f_{cr}^{(\lambda)}} \right) \tag{20}$$

where $\dot{\xi}_{max}$ is the maximum rate of transformation, as the hyperbolic tangent reaches a maximum value of one. The transform viscosity parameter ν_{tr} can be adjusted to control

the desired amount of rate dependence in the transformation. Note that unlike the rate-dependent crystal plasticity model laid out in the previous section, transformation is only active when the Macaulay brackets are satisfied; that is, only when $f_{tr}^{(\lambda)}$ exceeds $f_{cr}^{(\lambda)}$. The transformation is also uni-directional on each system (while $\dot{\gamma}^{(\alpha)}$ in Equation (13) can be positive or negative, $\dot{\xi}^{(\lambda)}$ is only positive or zero). There are 24 transformation systems for the austenite, and 12 of them are reverse vectors of the others. This is employed to ensure that although transform can occur in either direction, the austenite can only transform into martensite, and not the reverse.

The rates of transformation $\dot{\xi}^{(\lambda)}$ must be non-negative because they have the physical meaning of the rate of volume fraction transform on that given system. When summed together, they give the rate of change of the volume fraction transformed from austenite to martensite, which is then multiplied by the time step, Δt, to obtain the total volume fraction transformed:

$$\dot{V}_{trans} = \sum_{\lambda=1}^{N_{trans}} \dot{\xi}^{(\lambda)} \tag{21}$$

$$V_{trans} = \dot{V}_{trans} \cdot \Delta t \tag{22}$$

where $\dot{V}_{trans}$ is the total volume fraction rate of transform of retained austenite, and V_{trans} is the total volume fraction transformed. Limits placed on the system transform amounts $\xi^{(\lambda)}$ are based on the initial volume fraction of retained austenite in the material, designated as $RA_{initial}$. Transformation in sum, as well as on any given system, cannot exceed the initial amount of austenite present, as governed by Equations (23) and (24).

$$0 \le V_{trans} \le RA_{initial} \tag{23}$$

$$0 \le \xi^{(\lambda)} \le RA_{initial} \tag{24}$$

When activated, the transform rates $\dot{\xi}^{(\lambda)}$ on the transformation systems drive the rate of change of the transform deformation gradient according to

$$\dot{\underset{\sim}{F}}^{tr} = \sum_{\lambda=1}^{N_{trans}} \dot{\xi}^{(\lambda)} \cdot \left(\gamma_T \cdot \hat{\underset{\sim}{b}}_0^{(\lambda)} \otimes \underset{\sim}{n}_0^{(\lambda)} \right) \tag{25}$$

Additionally, the transform rates control the evolution of the critical driving force $f_{cr}^{(\lambda)}$ via

$$\dot{f}_{cr}^{(\lambda)} = \sum_{\eta=1}^{N_{trans}} Q \cdot \left| \dot{\xi}^{(\eta)} \right| \tag{26}$$

where Q is the direct hardening parameter of transformation. This accounts for the increased resistance to transform as more of the retained austenite becomes surrounded by transformed martensite. The increase in resistance to transform on any system is assumed to be the same.

2.7 Fatigue Indicator Parameters

In order to understand the influence inclusion orientation, effects, and shapes on the driving force for subsurface fatigue crack nucleation distinguish, we must evaluate the cyclic plastic behavior of the material. Two effective strain-based measures of this behavior are the ratcheting plastic strain increment, and the reversed cyclic plastic strain range [3]. The ratcheting plastic strain increment accumulated over one pass of the roller is given as:

$$\left(\Delta\varepsilon_{ij}^{p}\right)_{ratch} = \left(\varepsilon_{ij}^{p}\right)\Big|_{\text{End of Cycle}} - \left(\varepsilon_{ij}^{p}\right)\Big|_{\text{Beginning Of Cycle}} \tag{27}$$

For convenience, the effective ratcheting plastic strain increment, hereon referred to as ERPSI, is defined as

$$\Delta\varepsilon_{ratch,eff}^{p} = \sqrt{\frac{2}{3}\left(\Delta\varepsilon_{ij}^{p}\right)_{ratch}\left(\Delta\varepsilon_{ij}^{p}\right)_{ratch}} \tag{28}$$

The reversed cyclic plastic strain range over a given cycle is defined as

$$\left(\Delta\varepsilon_{ij}^{p}\right)_{cyc} = \left(\Delta\varepsilon_{ij}^{p}\right)_{max}\Big|_{\text{Over the Cycle}} - \left(\Delta\varepsilon_{ij}^{p}\right)\Big|_{ratch} \tag{29}$$

Again, it is convenient to look at the value in a Von-Mises type effective formulation, the effective cyclic plastic strain range (ECPSR):

$$\Delta\varepsilon_{cyc,eff}^{p} = \sqrt{\frac{2}{3}\left(\Delta\varepsilon_{ij}^{p}\right)_{cyc}\left(\Delta\varepsilon_{ij}^{p}\right)_{cyc}} \tag{30}$$

The ECPSR and ERPSI are simple scalar fatigue indicator parameters (FIPs). Critical plane based FIPs can also be used [32].

A critical-plane approach is motivated by observation of planes in which fatigue cracks form. The classical critical-plane approach is the Fatemi-Socie parameter [14].

$$P_{FS} = \frac{\Delta\gamma_{max}^{p}}{2}\cdot\left(1+k\cdot\frac{\sigma_{n}^{max}}{\sigma_{y}}\right) = \frac{\left(\tau_{f}'\right)^{2}}{G}\cdot\left(2\cdot N_{f}\right)^{b} + \gamma_{f}'\cdot\left(2\cdot N_{f}\right)^{c} \tag{31}$$

where $\Delta\gamma_{max}^{p}/2$ is the maximum plastic shear strain amplitude for the cycle, k is a parameter found by fitting uniaxial test data against torsion test data, σ_{n}^{max} is the maximum normal stress acting on the $\Delta\gamma_{max}^{p}$ plane, and σ_{y} is the yield stress. The Fatemi-Socie parameter is an effective measure of the driving force for fatigue crack

nucleation in scenarios where cracks grow in planes of high shear [4], which is often the scenario in rolling contact fatigue.

Since ratcheting defined by Equations (27) and (28) plays a key role in damage accumulation surrounding inclusions, a modified Fatemi-Socie formulation proposed by Zhang and coworkers [60] is:

$$P_{ratch} = \left(\Delta\gamma^{p}_{max}\right)_{ratch} \cdot \left(1 + k \cdot \frac{\sigma_n^{max}}{\sigma_y}\right) \tag{32}$$

with $\left(\Delta\gamma^{p}_{max}\right)_{ratch}$ being the maximum ratcheting shear strain from the ratcheting strain field given by Equation (27), and all of the other parameters are the same as defined in Equation (31).

CHAPTER 3: METHODOLOGY

3.1 Goals

The specific goal of this project is to develop structure-property-performance relations for rolling contact fatigue. Whereas previous approaches to modeling rolling contact have relied on empirical data and macroscopic finite element models, this new approach seeks to capture explicitly the influence of microstructure on performance. In addition, the previous numerical modeling has been primarily two-dimensional, thus neglecting key end effects which are addressed in the new three-dimensional technique. Approaching this task requires two key items to be developed: a geometric representative model, and polycrystalline material models sensitive to the attributes aforementioned. Key attributes for the geometric model are an accurate loading representation, and efficiency in running these models to simulate multiple passes of a bearing. This will facilitate gauging relative fatigue performance of different realizations of microstructure including inclusion orientation, amounts and distributions of retained austenite, and microstructural characteristics such as grain distribution and sizing. The material model must incorporate polycrystalline plasticity of martensite, as well as account for austenite-martensite transformation and the associated inelastic transform strains. Once developed, the long-term goal is to create a system in which other structural features, such as voids (cracks), transformed microstructure, and the influence of near-surface microtexture can be included.

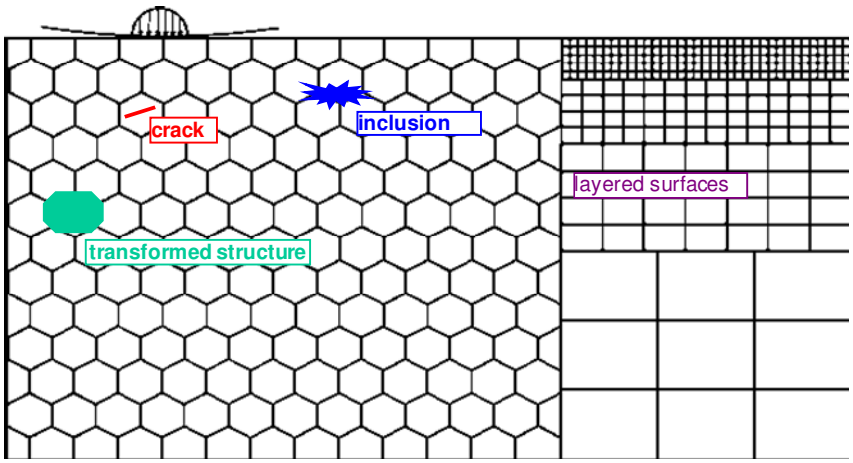

Figure 13. Additional applications of developed model.

This work focuses on free rolling. Tractive rolling, sliding and fretting cases are extensions of the current work by changing the boundary conditions on the geometric model. Hence, problems involving gears and other normal/tangential contact problems can also be investigated using this methodology by changing the boundary conditions on the geometric model.

3.2 Geometric Finite Element Models

When designing the geometric models, it was necessary to accurately represent the loading of roller bearings passing along a bearing race. This involves re-creating the Hertzian loading condition of a portion of a half-space, as described by Equations (3) through (33). It is also important to be able to efficiently conduct multiple simulated passes in the most efficient manner possible. Bearing races are subject to very large numbers of cycles, with multiple bearings passing over a given location in the race through a single rotation of the accompanying part.

Three scaling levels were considered in this project, using ABAQUS software [1]. The first was a large-scale model, which models a chunk of the race large enough to

explicitly model the bearing load passing along its top (positive y-face) surface. The second was a small-scale volume element model, designed to be small relative to contact width, and depicting the immediate volume surrounding a single inclusion. And third, a sub-model, with scaling in-between the first and second models described. The relative scaling of each are depicted in a schematic showing typical dimensions in Figure 14.

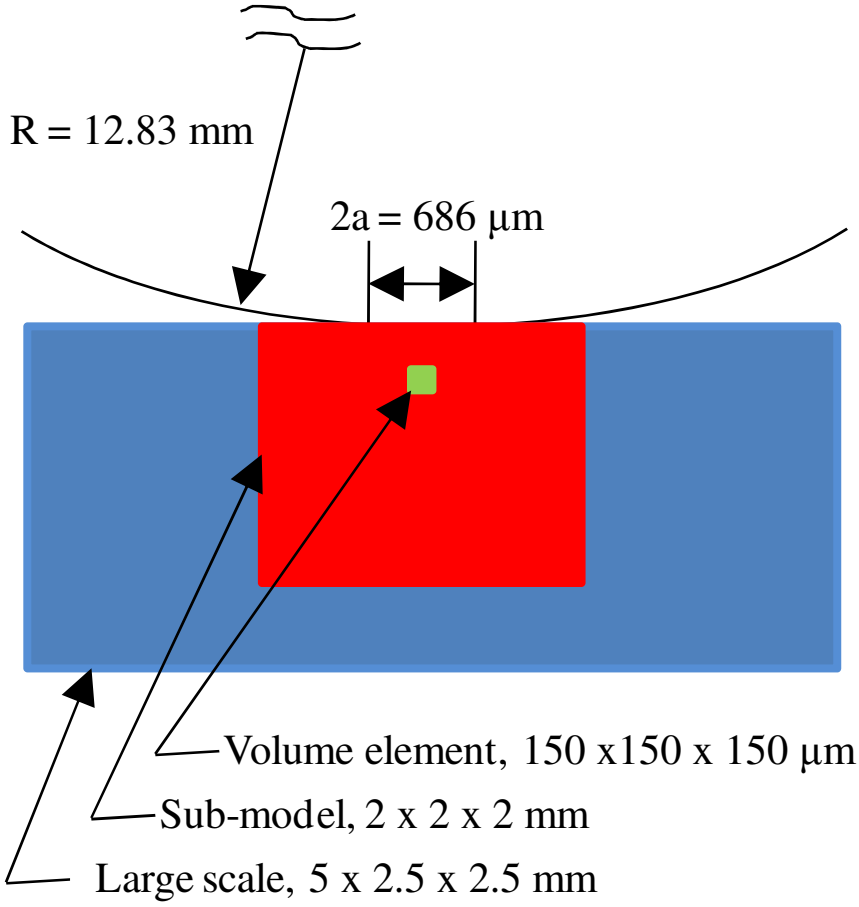

Figure 14. Schematic depicting the relative sizes of the three model scales.

Each model has advantages and disadvantages to consider, discussed herein, and are appropriate for different modeling situations.

3.2.1 Large-scale Model

The purpose of the model is to generate an accurate far-field stress distribution relative to the inclusion size. It was developed as an initial attempt to model a sizable portion of the bearing race. The overall shape was a three-dimensional brick with elastic far-field zone, plastic zone near the inclusion, and elastic inclusion zone at depth, as depicted in Figure 15.

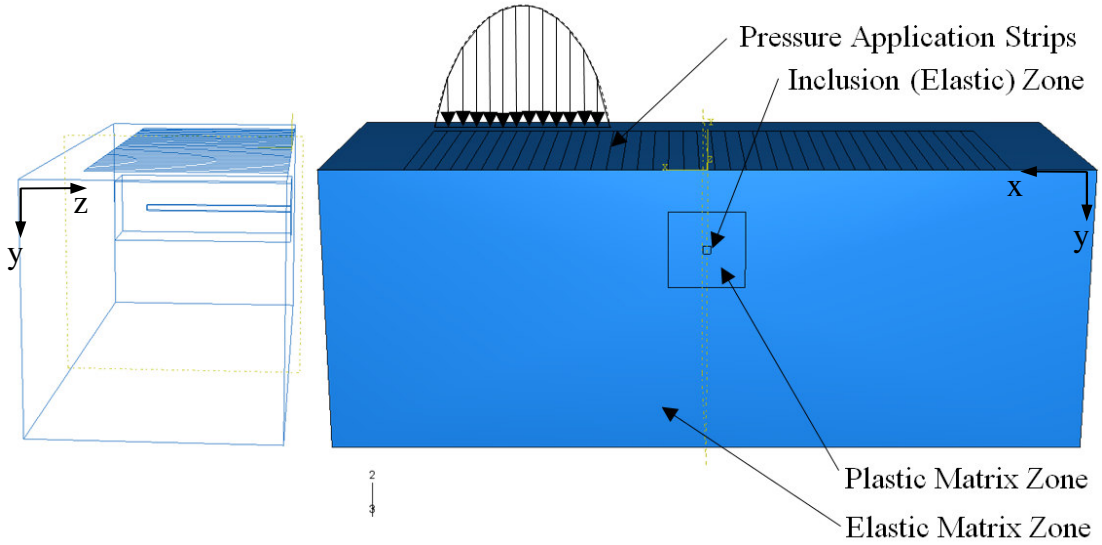

Figure 15. Large-scale model setup.

The boundary conditions are a fixed vertical (y) displacement of zero on the bottom surface (opposite the load application surface), and 3-D simply supported scheme at two corners of the bottom surface (x and z one corner, z another). An elastic zone surrounds all sides of the plastic zone containing the inclusion, as seen by the hidden side view on the left. The large-scale model shown was set up for a parallel orientation inclusion, and thus can take advantage of symmetry on the z-normal face. The Hertzian contact

pressure provided by Equation (3) was applied discretely with trapezoidal application across 13 pressure application strips, as shown in Figure 16.

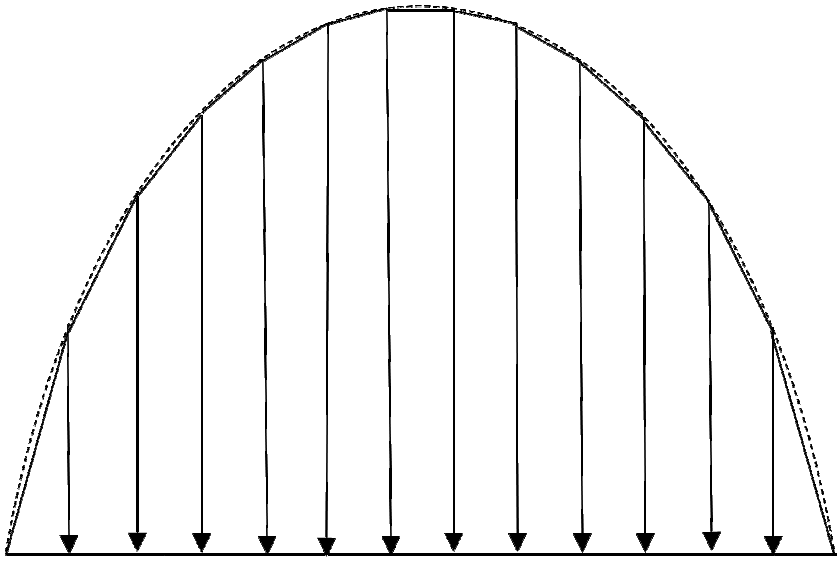

Figure 16. Contact pressure application scheme.

The application of this load can thus be "rolled" in increments as small as 1/13 of the contact width, to simulate a roller pass. The increments were set large when the load was far from the inclusion, and space closer together when directly over the inclusion region. This scheme of rolling for a single pass of a bearing is depicted in Figure 17.

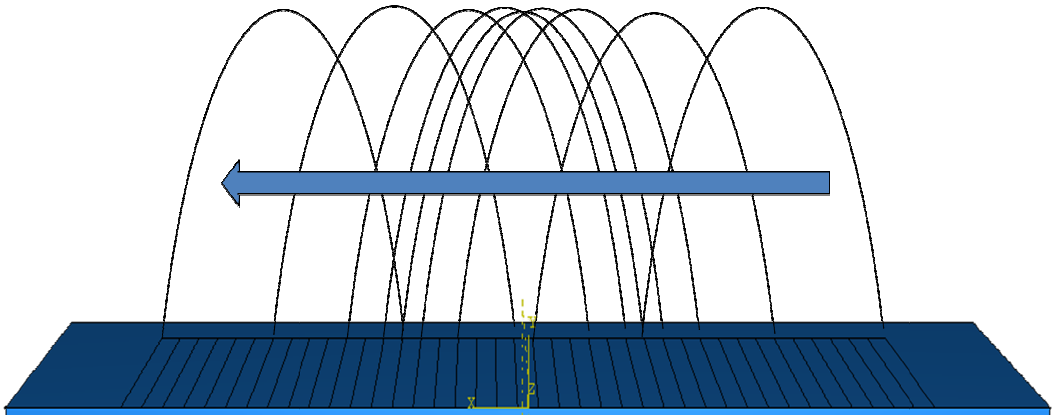

Figure 17. Pressure strip simulated pass.

This loading and geometry scheme provides an excellent stress distribution relative to the analytical solution. The pressure application results in a smooth vertical normal stress component (σ_{yy}), even in the higher pressure gradient areas on the far left and right of the contact width, as shown at center loading in Figure 18.

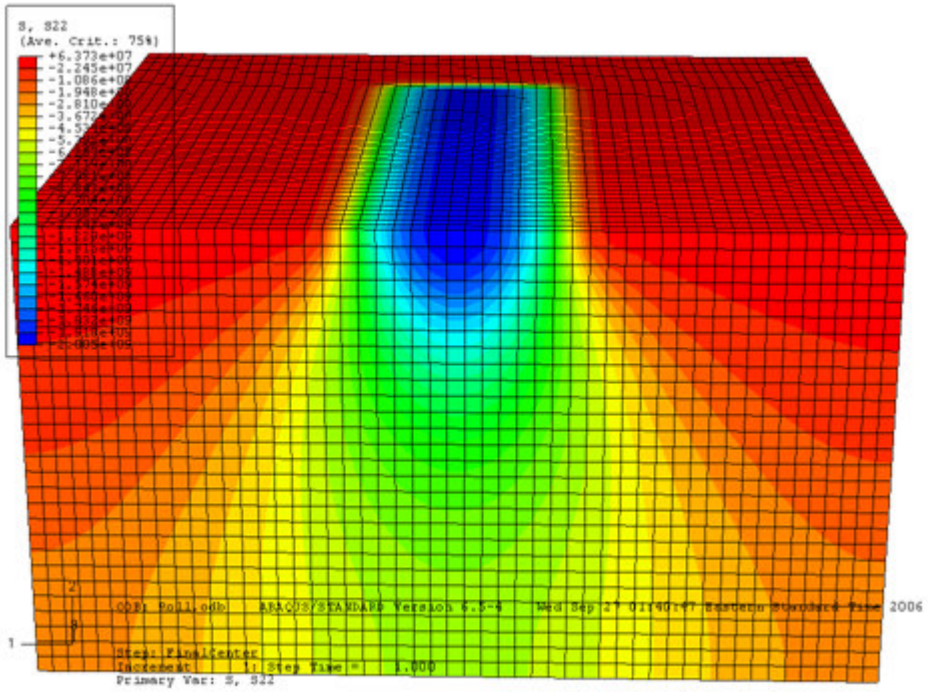

Figure 18. Large-scale model y-normal stress distribution.

Examining the Tresca stress distribution at the same loading point, it can be seen that the characteristic stress field predicted by a Hertzian analytical loading is generated in the finite element model. Some end effects can be seen at the lower corners of the model, but they are sufficiently far from the "hot zone" so as not to interfere with the important distribution at depth of max Tresca stress.

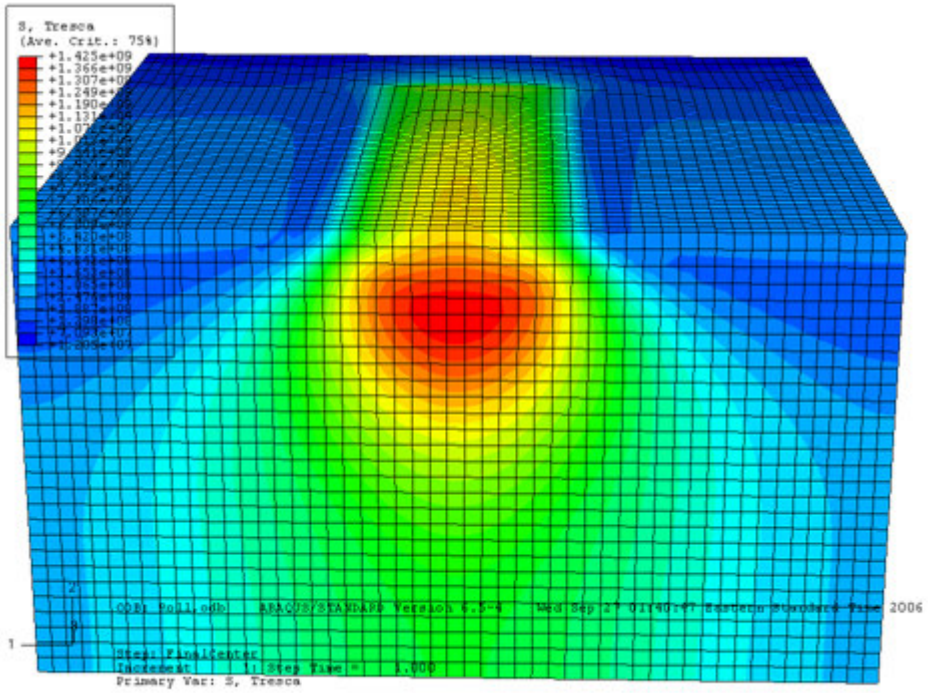

Figure 19. Large-scale model Tresca stress distribution.

The large-scale model's advantages are a simple loading scheme and boundary conditions, and accurate representation of the stress field at depths other than close to the model bottom support. However, the model also presents several disadvantages. Note that in the previous figures, the mesh is fine enough to create a smooth stress state, but it is not small enough to accurately depict inclusion entities. The already high element count would have to be increased eight-fold for every halving in size of the brick elements used. Due to mapped meshing requirements in the ABAQUS software, brick elements must essentially be uniform in size over a 3-D model to mesh properly. The issue was addressed with tetrahedral elements to gauge if this could provide a solution. It was determined that although the tetrahedral elements allow for selective mesh

refinement enough to allow inclusions to be modeled, the resulting stress distribution became much less smooth, as depicted in Figure 20.

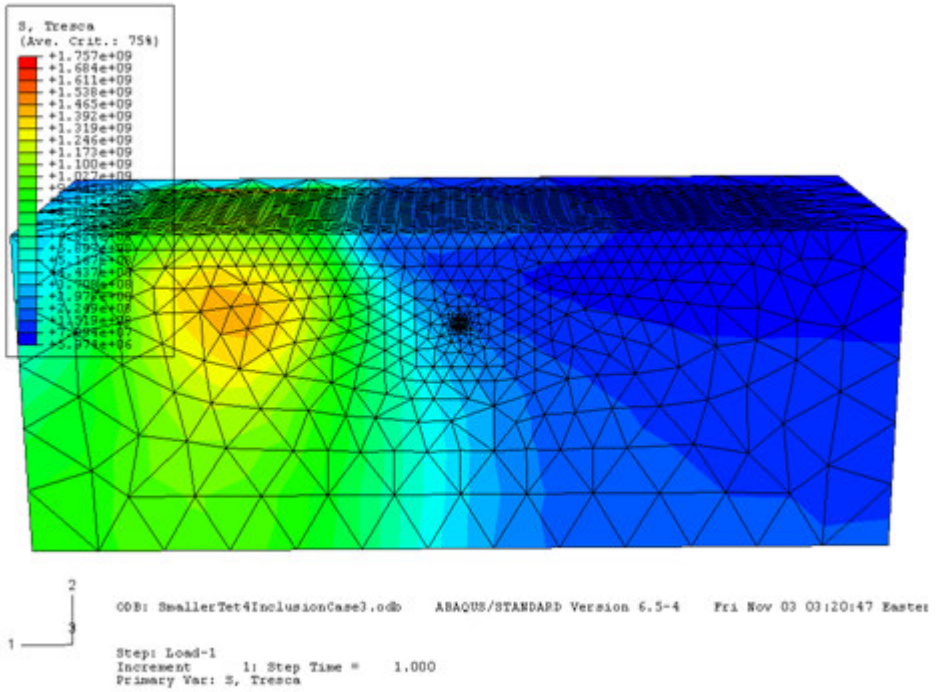

Figure 20. Tetrahedral meshing Tresca stress distribution.

For the tetrahedral mesh shown above, with elastic and elasto-plastic J_2 elements, a typical single bearing pass took approximately 12 hours to complete on a Windows-based PC with a 2 GHz processor. For rolling contact fatigue analysis, at least three passes must be conducted in order to achieve shakedown and spot any cyclic plastic behavior, resulting in an average run time of 36 hours. Insertion of crystal plasticity material models would amplify the run time significantly over the J_2 formulation. Therefore, following several test scenarios with the large-scale model setup, it was found to be too computationally expensive for the mesh density required near the inclusions. When considering the need for multiple cyclic passes, this scale of model was not feasible.

3.2.2 Small-scale Volume Element Model

The small-scale volume element approach was conceived to study the plastic strain accumulation around smaller inclusions in better detail. The stress state given by Equations (4) to (7) is applied as boundary conditions. They are integrated in the user-defined traction routine via a trapezoidal method. In order to apply the stress state, the stress tensor is multiplied by the normal vector of the geometric face, giving the traction vector (Equation (33)).

$$\underset{\sim}{t} = \underset{\sim}{\sigma} \cdot \underset{\sim}{N} \tag{33}$$

From this equation, the traction boundary conditions for the models are generated. These loadings are applied to a subsurface volume element base material containing an inclusion, as depicted in Figure 21. The size of the cubic volume element is chosen to be small relative to the contact size to provide a reasonable assumption of uniform (minimal gradient) stress distribution at the edges of the model.

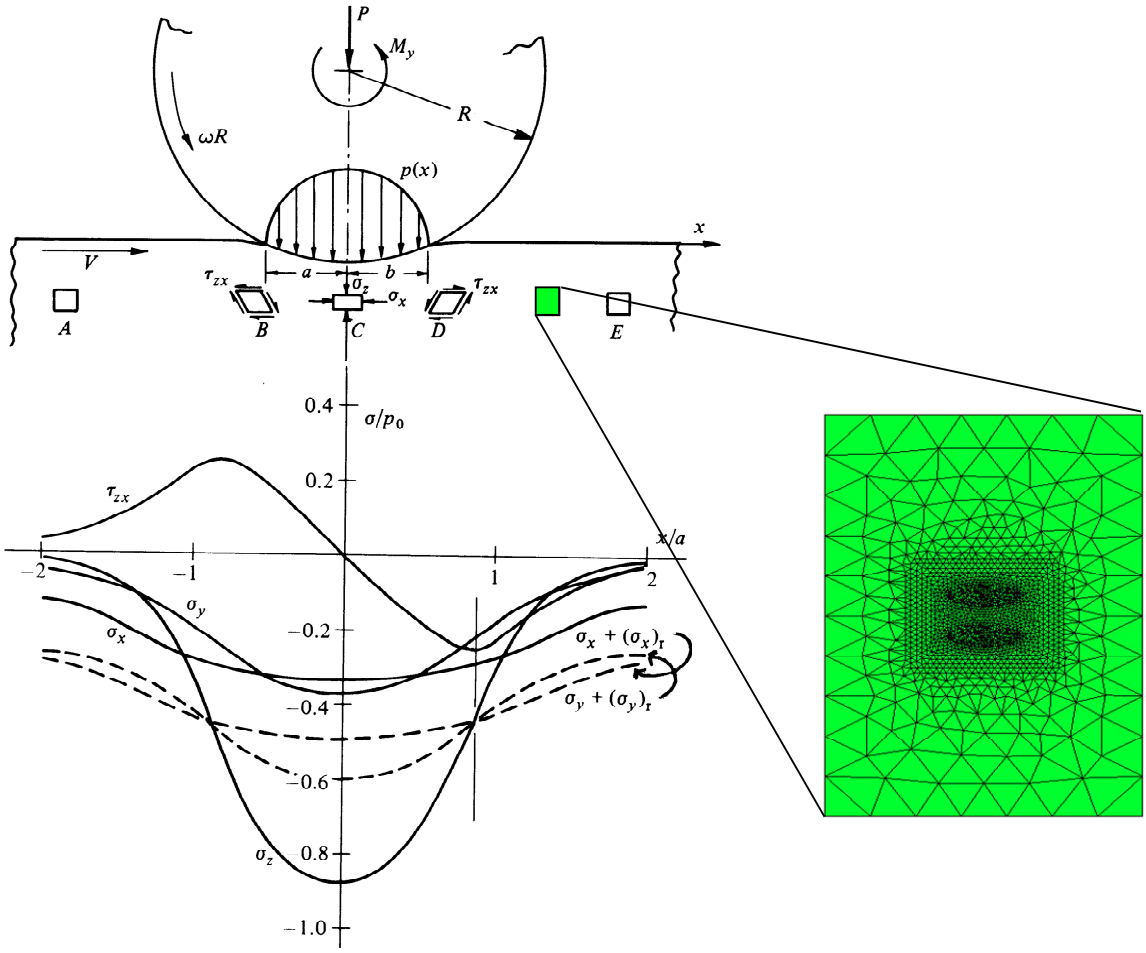

Figure 21. Small-scale volume element scheme [21].

This allows for a very fine mesh surrounding the inclusion, to study the cyclic plastic strain accumulation local to a single inclusion and the corresponding likelihood of fatigue crack nucleation. Given the scaling considerations, inclusions of size 10 x 10 x 50 μm and 10 x 10 x 10 μm were modeled, with a volume element of side length 150 μm. At this size, the variation in stress components that are being approximated by uniform tractions is approximately 7% of the nominal value over the side length of the volume element.

Loads are applied as uniform tractions on each surface of the model, and a 3-D simple support is applied at three corners of the model to eliminate rigid body modes. A cutaway of the volume element model is shown, meshed with tetrahedral elements, depicting the loading applications in Figure 22. The use of tetrahedral elements allows free meshing and an increased density immediately surrounding the inclusion. Mesh size seedings are given for the model in Table 1.

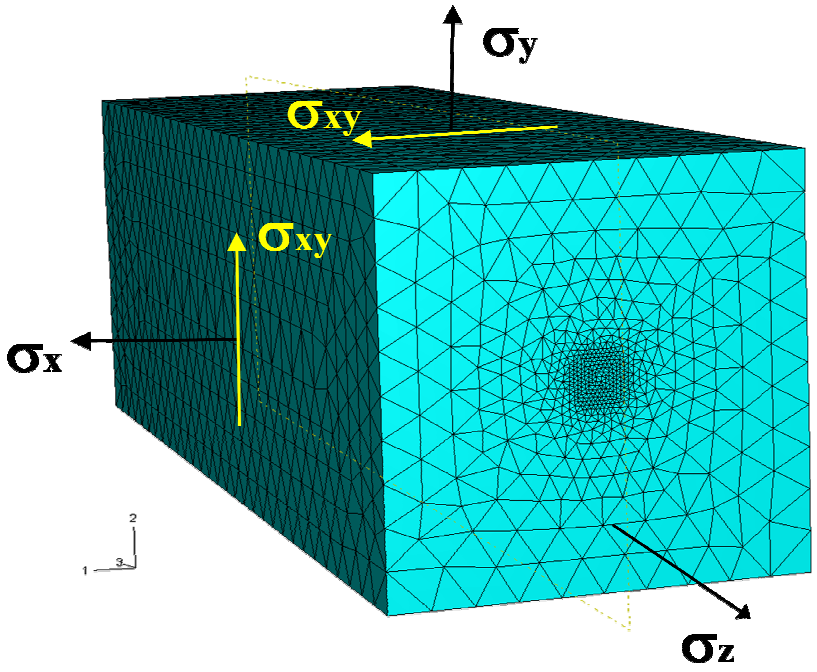

Figure 22. Volume element load applications.

Table 1. Volume element mesh sizing for tetrahedral elements.

Mesh Region	Nominal Mesh Element Size
Inclusion	1.25 μm
Matrix Inner Boundary	1.25 μm
Matrix Outer Edges	15 μm

The model simulates a pass by simply varying the magnitude of these traction boundary conditions in a series of segments. The spacing of these loading points, shown in Figure 23, is chosen such that linear interpolation between them will reasonably recreate the analytical stress variations as given by Equations (4) to (7). This is implemented using the ramped amplitude option in ABAQUS. For this model, nine discrete load points were chosen, as shown in Figure 23. They provide a good representation of the stress component curves. In addition, the x-location spacing of the load points was chosen such that a load step fell on the maximum positive and negative values of the maximum orthogonal shear stress (see the green curve below). The y-location, or depth, of the volume element is chosen and remains a constant for the stress application calculations within the simulation. Determination of the number of load steps to use involved manually increasing the number of load steps per pass until the results were within tolerance of each other. The magnitude of the applied loading is such that without the inclusion as a stress riser, the model would remain in the elastic regime. Thus, the curves shown in Figure 23 are those of the elastic Hertzian distribution depicted in Figure 9.

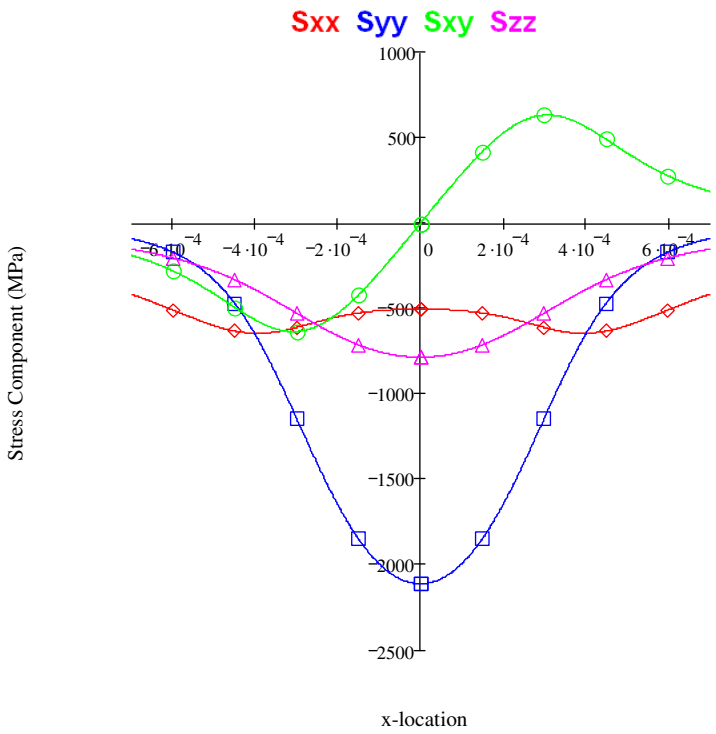

Figure 23. Loading application points for a simulated bearing pass.

To apply these loads efficiently in ABAQUS, a user traction subroutine (UTRACLOAD) was created to calculate the traction vector for each face of the volume element, by computing the singular integral Equations (4) through (7) and then multiplying by the unit normal vector of the face (Equation (33)). An input vector changes the x-coordinate in the calculations for each load step, while the y-depth is held constant. To add versatility to the model, a rotation option was added to the UTRACLOAD. By entering a direction cosine matrix, the stress state can be rotated from the global (load applied) coordinate directions to any chosen volume element orientation,

$$\underset{\sim}{\sigma}_{VE} = \underset{\sim}{R} \cdot \underset{\sim}{\sigma}_{G} \cdot \underset{\sim}{R}^{T} \tag{34}$$

where $\underset{\sim}{\sigma}_G$ is the stress in global coordinates, $\underset{\sim}{\sigma}_{VE}$ is the stress in the volume element's rotated orientation, and $\underset{\sim}{R}$ is the rotation matrix, whose columns are the direction cosines of the volume element's coordinate axes relative to the global coordinates.

By rotating the stress field, any inclusion orientation can be easily modeled without the need to re-mesh. This also allows for the use of brick elements through mapped meshing, when the model is sub-divided into rectangular prism regions (all edges right angles).

The volume element model with brick elements is divided using the partition tool within ABAQUS/CAE. This allows meshing of the model with different material properties on a single part, assuming bonded interfaces. Therefore, the inclusion, crystal plasticity region, and outer transition regions are all sharing common border nodes, as opposed to using contact formulations which can cause artificial stress risers. The resulting partitions give 125 regions. The central single region is the inclusion, as shown in Figure 24.

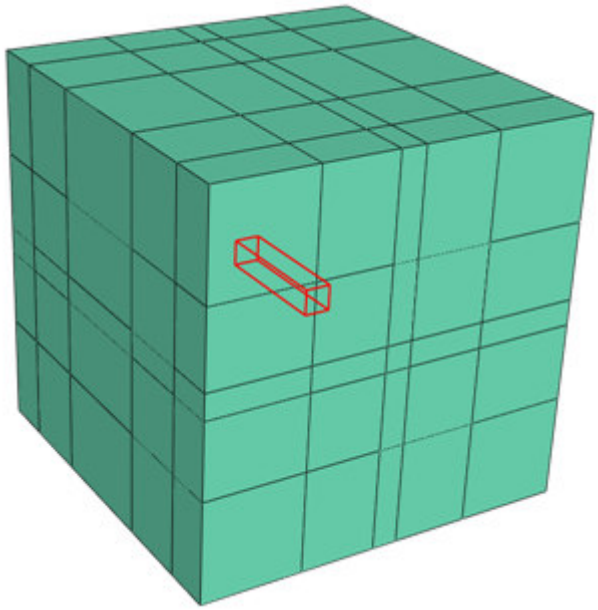

Figure 24. Inclusion region in volume element model.

All 26 regions immediately surrounding the inclusion are for the plastic (J_2 or crystal) section, highlighted in Figure 25. The outside 98 regions are an elastic cushion zone providing a transition of the boundary condition stresses to the plasticity region.

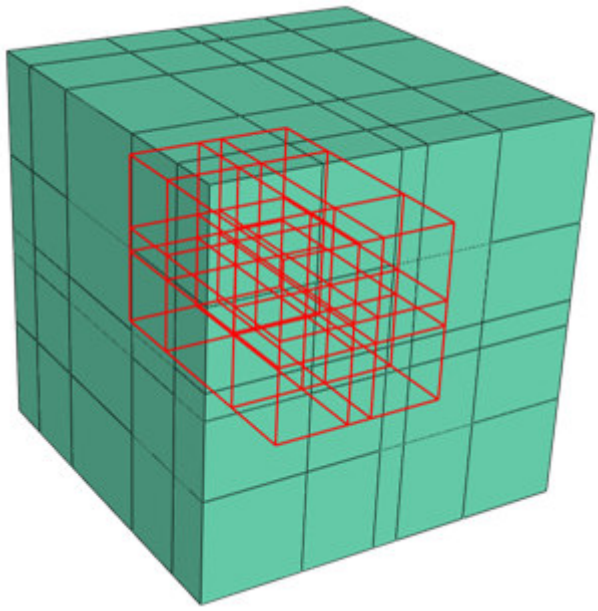

Figure 25. Plasticity region in volume element model.

3.2.3 Sub-model

Seeking to take the best attributes from both the small-scale and large-scale approaches, the sub-model was designed to allow larger inclusions and stringers of inclusions to be studied without the computational expense of the large-scale model. The sub-model approach uses a size roughly an order of magnitude larger than the volume element model, with 2 x 2 x 2 mm size base metal matrix, which is large enough relative to the contact half-width to require a non-uniform traction distribution. This is applied via a modification of the user-defined traction routine UTRACLOAD developed for the small-scale model, where depth (y-location) and x-location are no longer considered constant over a face of the model. In this case, Equations (4) to (7) are calculated using the coordinates of each element's face as tractions are applied to them. These tractions

give a stress distribution similar to what would be expected in a semi-infinite half-space. As can be seen in Figure 26, a plot of von Mises stress when the UTRACLOAD is applied, the scheme works well to deliver a smooth, analytical-matching stress distribution. The arrows are representative of the traction vectors applied by Equation (33), scaled for magnitude and direction. Note that on the top surface, the contact pressure is applied.

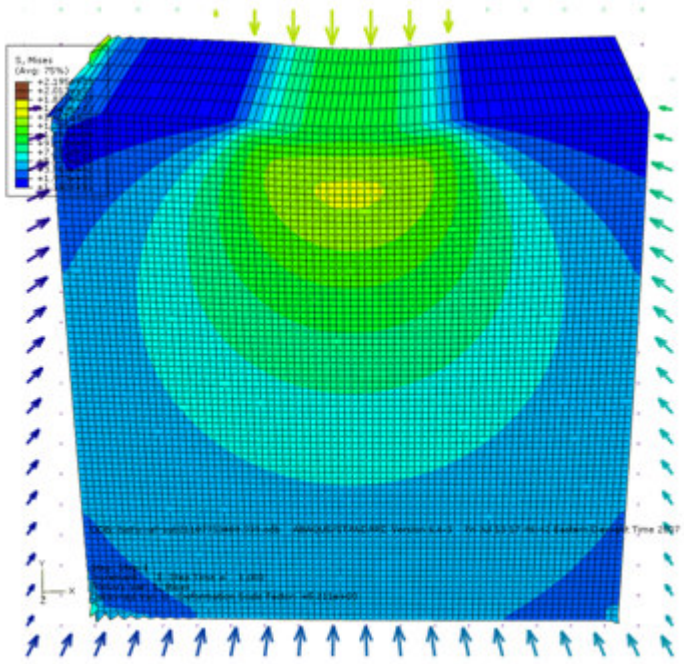

Figure 26. Sub-model setup with non-uniform tractions applied.

Major advantages of this model are its ability to handle larger inclusions as well as stringers of inclusions, and to create a smooth non-uniform stress field over the model. In addition, since the model represents a region of the bearing race up to the surface, it would be an ideal model for future implementation of tractive rolling, sliding and fretting simulations. The chief limitation for the model is a decidedly longer computation time

when compared with the volume element model. Typically there is a ten times increase in computing time over the small-scale model for an equivalent number of load steps.

3.2.4 Geometric Model Testing with J_2 Plasticity

Before implementation of the newly developed material model, the geometric models were tested using conventional macro-plasticity. To facilitate this, multiple-pass simulations were conducted using a J_2 macro-plasticity model. The 4145 steel response (fully martensite structure) was chosen as the base metal to test the geometric models, as it contains mostly a single-phase and has easily modeled material behavior. The inclusions are composed of aluminum oxide (Al_2O_3), which is stiffer than the base metal. Basic material properties, inclusion attributes, and loading parameters for the model are given in Table 2. The peak contact pressure is a modification from the value given for the loading case, specified by Timken as a typical bearing load test magnitude [11]. The load used here is 1.75 times the normal test load amount, and was overloaded such that the J_2 plasticity model produces inelastic behavior with the inclusion present as a stress riser, but not without an inclusion. The contact half-width, a, and the inclusion depth (the depth of maximum orthogonal shear) are functions of the peak applied loading. Three inclusion shapes were used: a rectangular prism, a cubic, and a cylinder. The nomenclature for their dimensions is given in Figure 27.

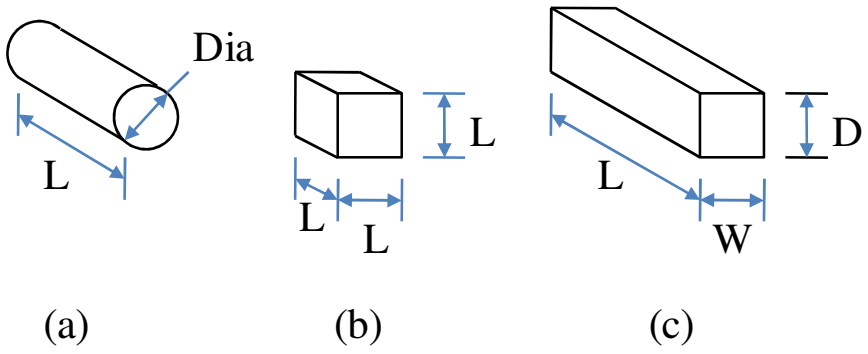

Figure 27. Inclusion dimension nomenclature for (a) cylindrical, (b) square, and (c) rectangular inclusion shapes.

Table 2. Geometric model testing parameters.

Material Properties	**Value and Units**
E_{base}	200 GPa
ν_{base}	0.3
σ_y	1500 MPa
E_{incl}	300 GPa
ν_{incl}	0.2
Inclusion Dimensions	**Value and Units**
L x W x D, rectangular inclusion	50 x 10 x 10 µm
L x Dia, cylindrical inclusion	50 x 10 µm
L, cubic inclusion	10 µm
Inclusion depth	267 µm
Loading Parameters	**Value and Units**
p_0	2.68 GPa
a	344 µm

The J_2 plasticity model with linear isotropic hardening available in ABAQUS was used. Pairs of stress and plastic strain, given in Table 3, represent the experimental 4145

steel with a fully martensitic microstructure. Linear interpolation was used between these points.

Table 3. Stress-plastic strain points for J_2 plsaticity with linear isotropic hardening

Stress (MPa)	**Plastic strain**
1500	0
1700	0.00448462
1900	0.01059270
2000	0.01501900
2100	0.02249680
2150	0.02858480
2200	0.04367300

Simulations were conducted for three inclusion shapes, with elongated inclusions oriented in various directions relative to the rolling direction. The three-dimensional nature of the model provides important end effects that cannot be captured by earlier two-dimensional models, as shown in Figure 28, which gives the effective plastic strain surrounding a rectangular inclusion in the parallel orientation. The inclusion outline can be seen in the center, and the model is cut through the origin normal to the x-direction and z-direction. Note the risers in accumulation of plastic strain near the end of the inclusion.

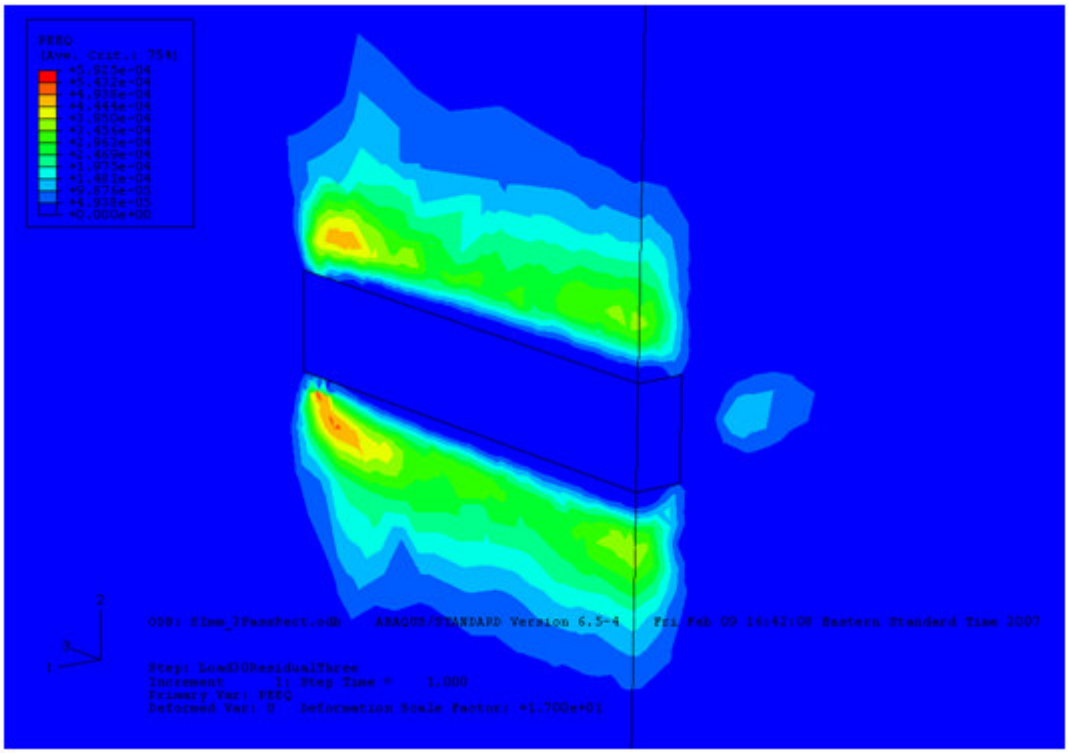

Figure 28. End effects of 3-D model on effective plastic strain.

Ratcheting behavior induced by high shear areas, as depicted in Figure 5 and Figure 6, can often lead to crack nucleation during cyclic loading. This was observed during the numerical testing of the geometric RCF models, where ratcheting plastic strains accumulated in the same locations. The ERPSI defined by Equation (28) was examined after each pass. The plastic strain accumulations for a rectangular parallel inclusion after the first, second, and third passes are shown in Figure 29. It can be seen that on the initial pass, the areas above and below the inclusion accumulate the most plastic strain, due to the high normal strains in those areas. However, they reach a shakedown in subsequent passes. The area of greatest plastic shear strains after the initial shakedown is near the corners of the inclusion. This corresponds well with the white etched areas of Figure 6, which depict areas that experienced high plastic strains.

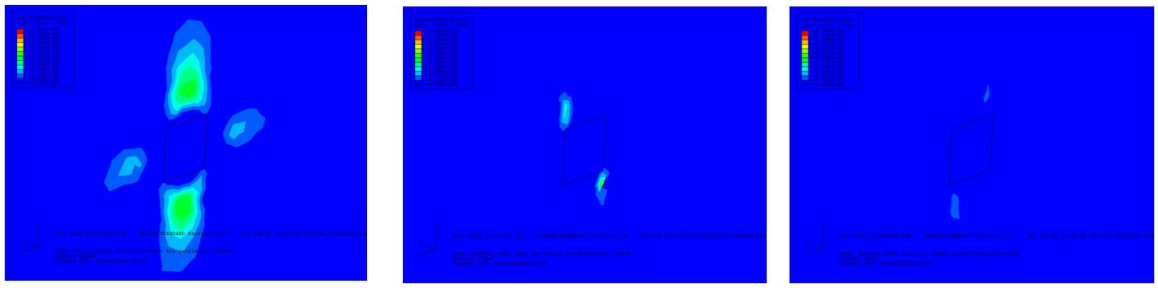

Figure 29. ERPSI in the x-y plane for 1st, 2nd, 3rd passes for a rectangular, parallel orientation inclusion.

It can be seen that the ERPSI accumulations due to high shear occur very near to the corners of the rectangular inclusion. To ensure that this behavior was not due to artificial numerical effects of the corners, a cylindrical inclusion was compared to the rectangular. Figure 30 and Figure 31 provide a comparison of the effective plastic strain after three passes surrounding rectangular and cylindrical inclusions, respectively In addition, Figure 32 and Figure 33 are plots of the in-plane (x-y) plastic shear strain.

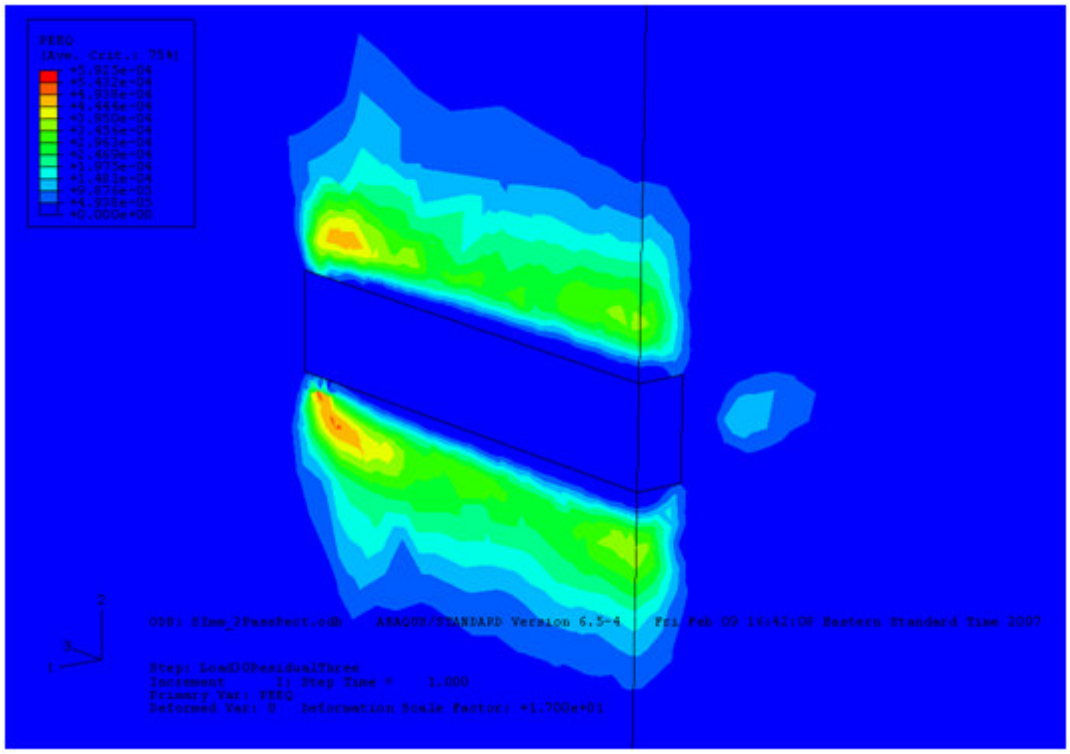

Figure 30. Effective plastic strain for rectangular parallel inclusion, cut on x and z-planes.

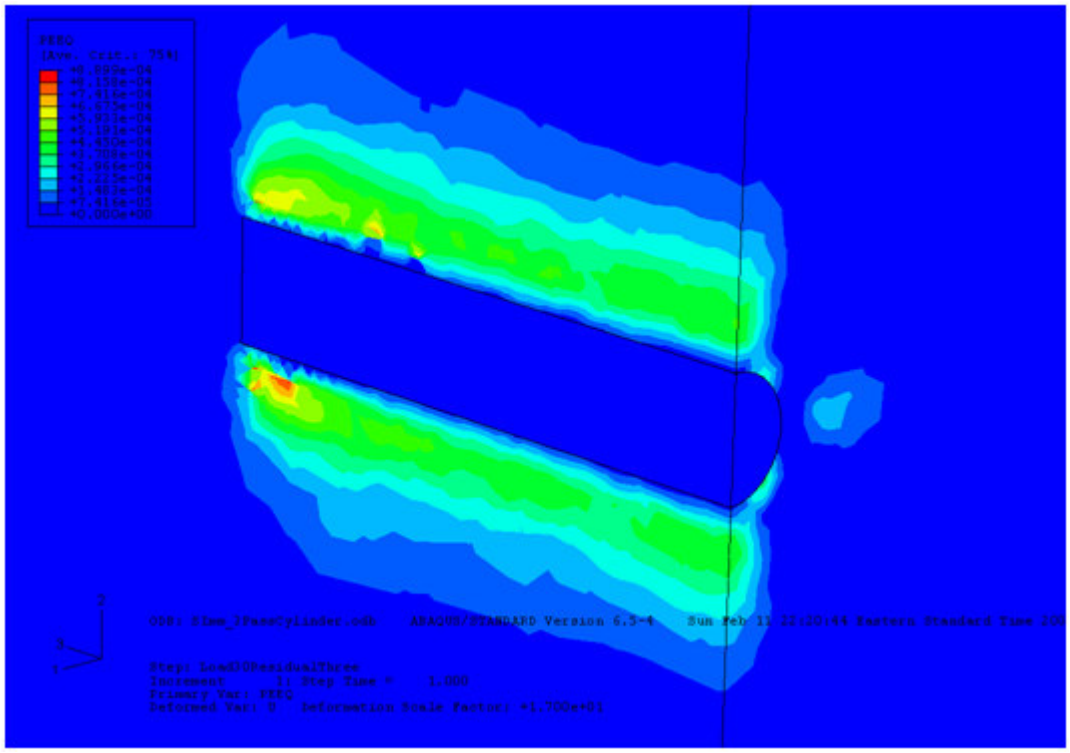

Figure 31. Effective plastic strain for cylindrical parallel inclusion, cut on x and z-planes.

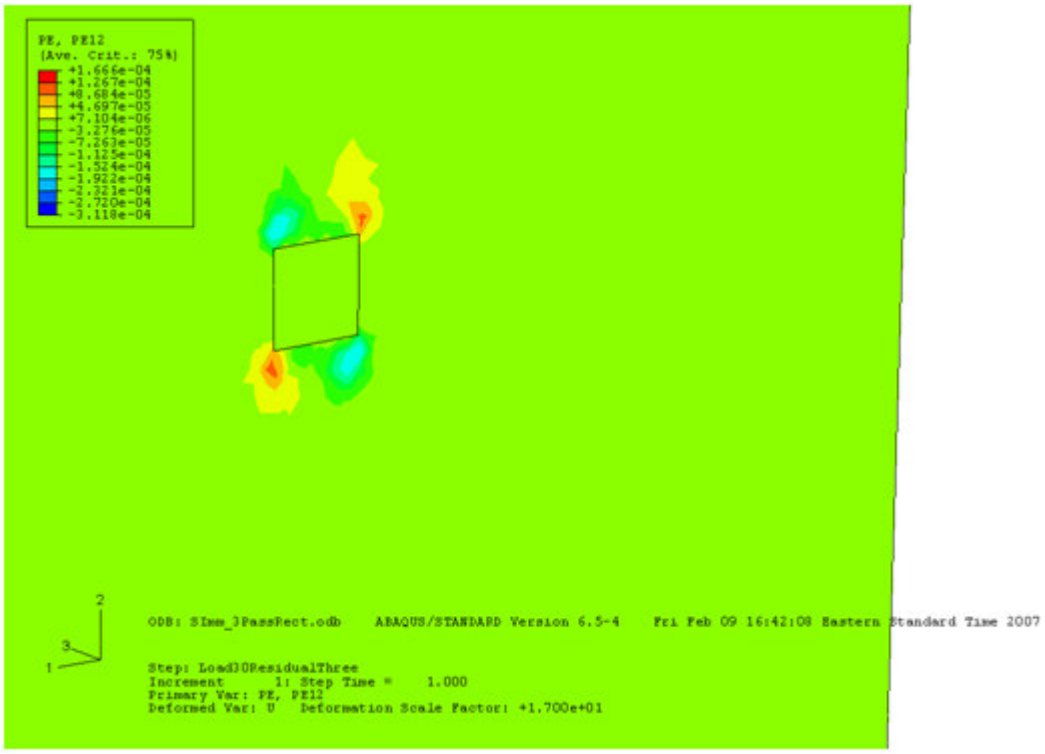

Figure 32. In-plane plastic shear strain for rectangular parallel inclusion, after 3rd pass.

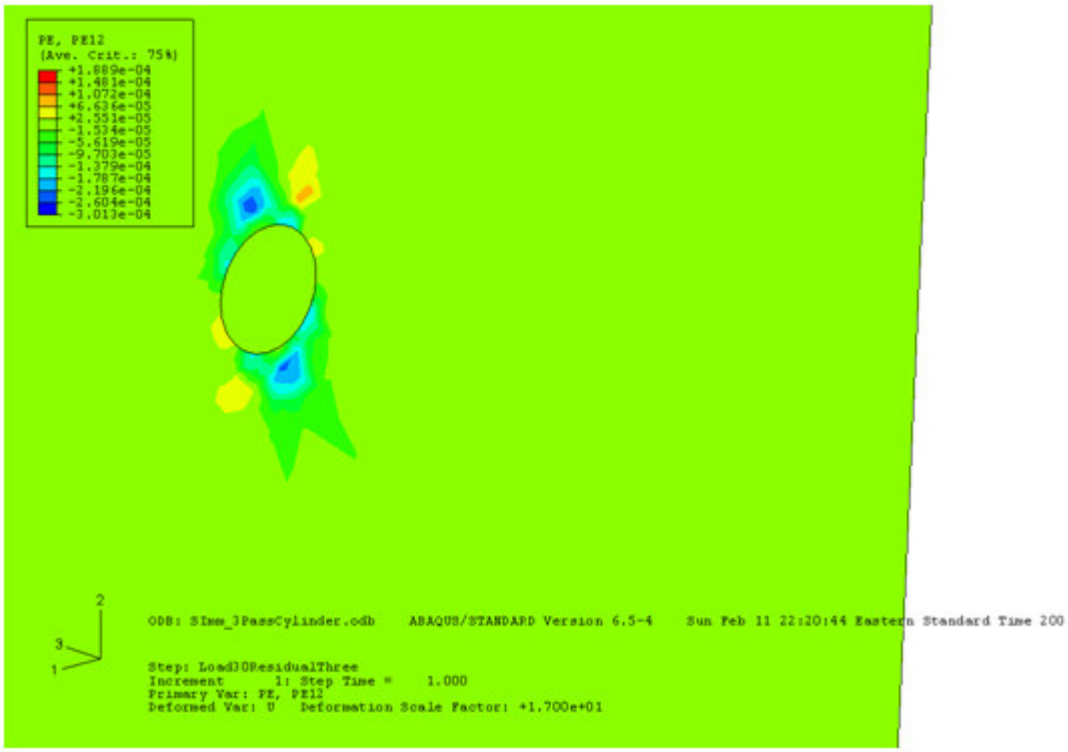

Figure 33. In-plane plastic shear strain for cylindrical parallel inclusion, after 3rd pass.

Note that in both cases, the magnitude and locations of these strains are quite similar. Thus, the rectangular inclusion gives a consistent response to a cylindrical modeled shape, and is preferable because of the ability to use brick elements and mapped meshing. The maximum shear locations fall on planes passing through the z-axis, and approximately 35 degrees from the y-axis. Examining a cut view of the model from Figure 32 on this plane reveals again the importance of end effects and the need for use of a 3-D model over previous 2-D attempts at inclusion studies, as shown in Figure 34. The increase in magnitude near the end of the inclusion demonstrates the significance of the end effect in the z-direction, which is excluded in 2-D studies.

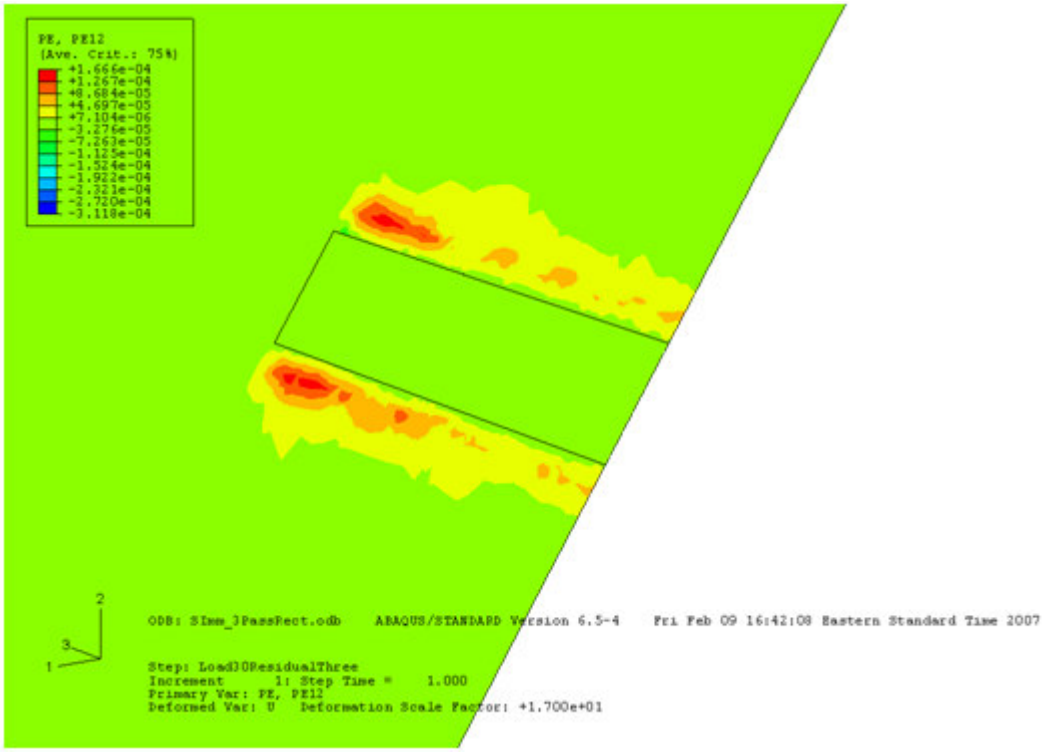

Figure 34. X-Y plastic shear strain on 35 degree angled cut, after 3rd pass.

The maximum value of the ERPSI for rectangular, cubic, and cylindrical inclusion shapes is shown in Figure 35 for the three principal direction orientations of rectangular and cylindrical inclusions, and for the cubic inclusion shape.

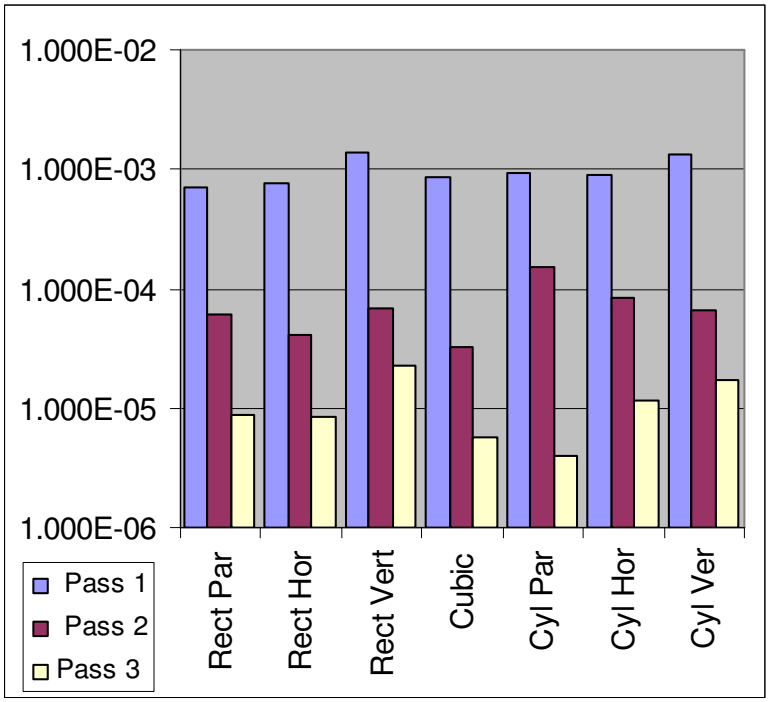

Figure 35. ERPSI by shape and orientation.

Note that the magnitude of plastic strain accumulation falls an order of magnitude in subsequent passes, and this trend is consistent across all shapes and orientations. After shakedown conditions settle, the third pass shows an indication of the vertical orientation accumulating the most plastic strain in both the rectangular and cylindrical shapes. Shown in Figure 36 is the third-pass ERPSI accumulation for a cylindrical inclusion case with its long axis oriented vertically. The accumulation builds in offset corner locations near the top and bottom ends of the inclusion.

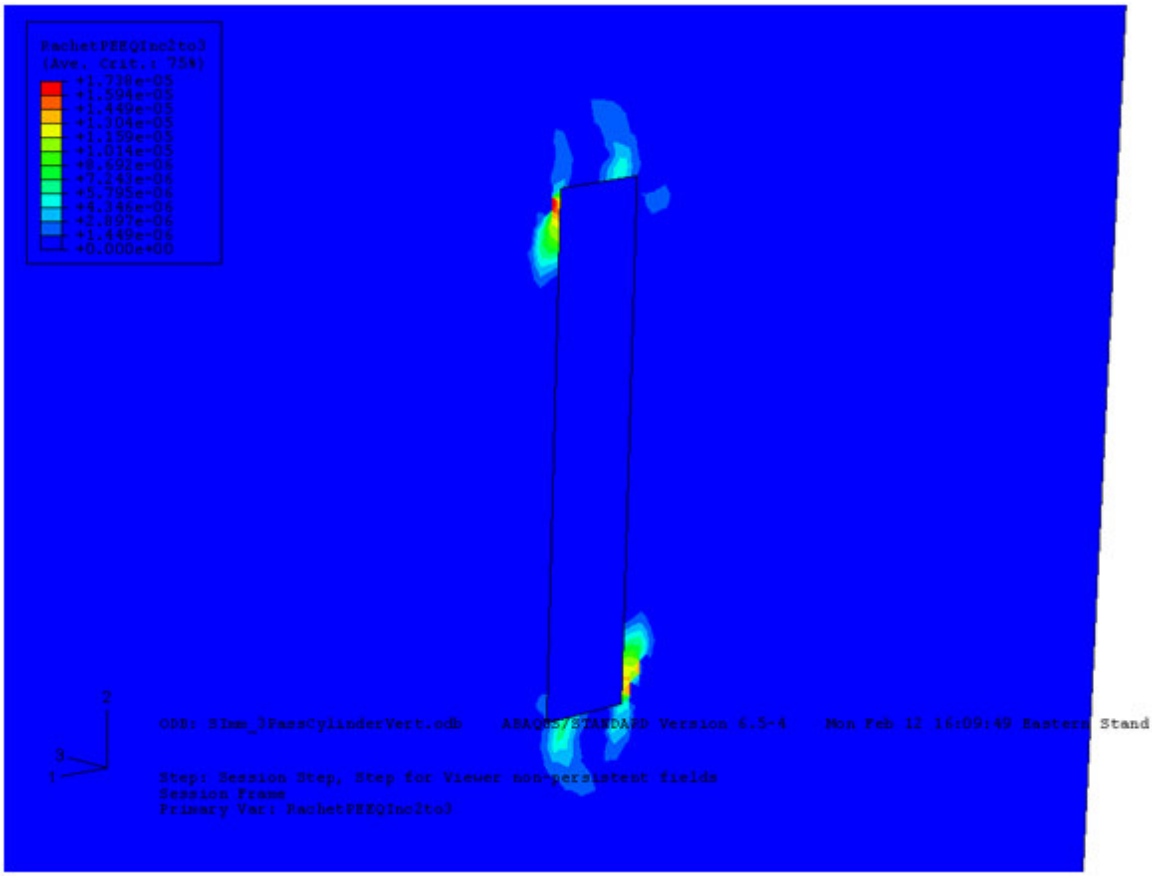

Figure 36. Third-pass ERPSI accumulation for a vertically oriented cylindrical inclusion.

The volume element model provides good plastic strain distribution detail near the inclusion, while being relatively cheap computationally. In addition, the inclusion can be oriented at various angles relative to the contact above it for parametric orientation studies to be conducted without re-meshing the model. Its main limitation is that the inclusion must be small relative to the contact half-width in order to assume uniform tractions on the faces of the volume element. The geometric model developed provides a consistent, expected response with the J_2 material model inserted, and will subsequently be used with the newly developed two-phase crystal plasticity model also developed in this project.

3.3 Advanced Material Modeling

3.3.1 Series 41XXX Steels

The 41XXX series of bearing steels was chosen as a representative material to build the modeling tools around. The structure type of these metals is lath martensite. Within a prior austenite grain, martensitic lathes are formed, and in some varieties, pockets of retained austenite remain between the lathes, as depicted by the schematic in Figure 37.

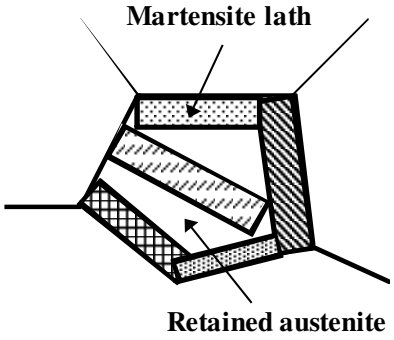

Figure 37. Lath martensite grain structure.

The response behavior of these steels can vary greatly by the initial volume fraction of retained austenite, heat treatment, and distribution of primary carbides. Shown in Figure 38 are plots of the response of various 41XXX varieties in tensile testing at room temperature, and a quasi-static strain rate of 1.0×10^{-4} s^{-1}. It can be seen that there is a great variation in response with change in initial volume fraction of retained austenite (RA).

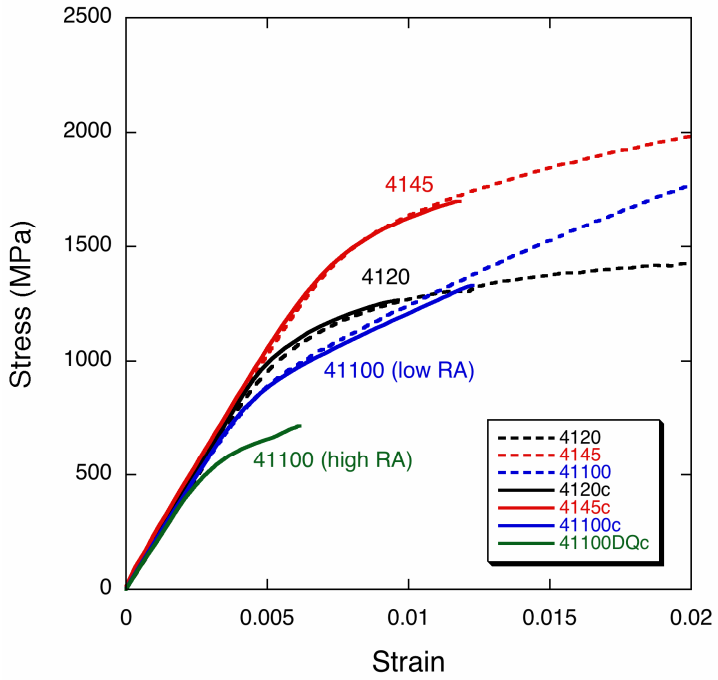

Figure 38. Stress-strain responses of various 41XXX steel varieties.

The two varieties chosen for this study were 4145 and 41100, with the latter being further divided into three different heat treatments. Magnified views (100x) of the actual microstructures for the 4145 and 41100 variants reveal the differences in appearance for various amounts of retained austenite. The 4145 material was selected because it is nearly fully martensitic, as indicated by the densely packed martensitic laths in Figure 39. Thus it can be reasonably treated as a single-phase dominant material. It is used to calibrate the martensitic plasticity portion of the material model developed herein.

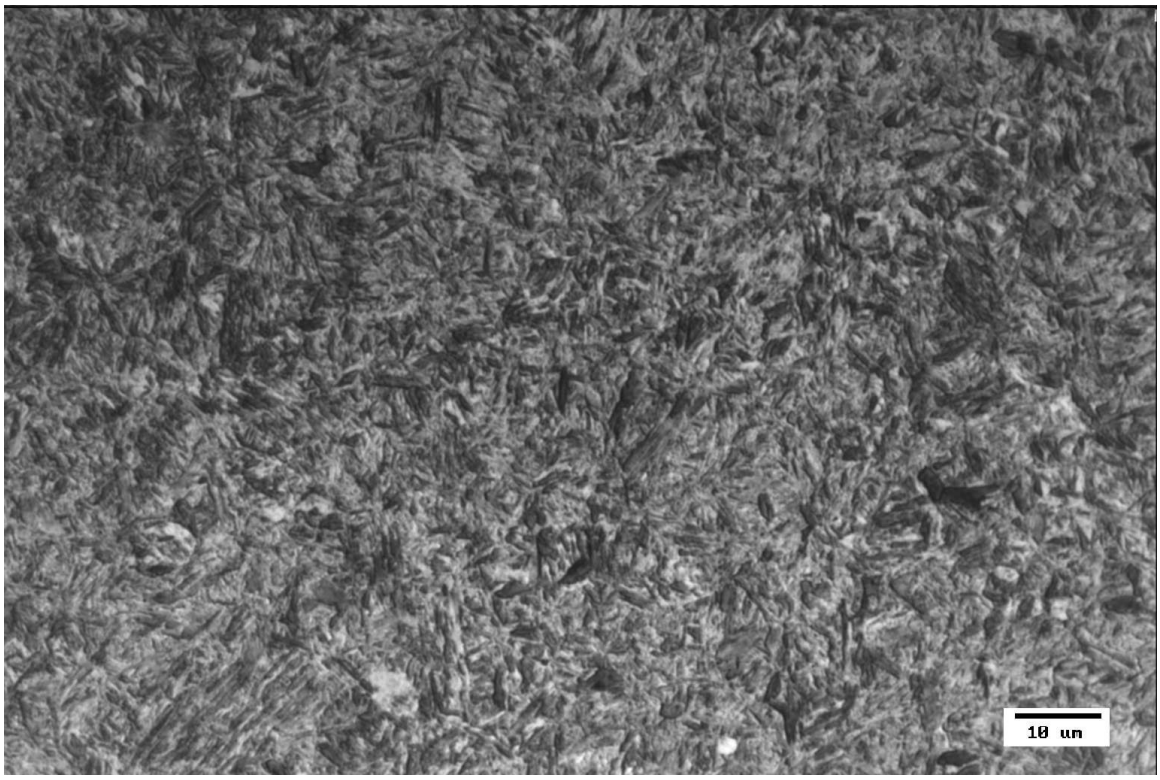

Figure 39. Micrograph of 4145 series steel.

The heat treatment of 41100 steels was varied to control the initial volume fraction of retained austenite. Three variants chosen were 13% RA, 22% RA, and 35% RA. Details on the heat treatment procedures for the three variants are given in Table 4, including austenitizing and tempering values of temperature and duration.

Table 4. Heat treatment schedule for 41100 steels to achieve 13%, 22%, and 35% initial retained austenite.

Process	**13% Retained Austenite**	**22% Retained Austenite**	**35% Retained Austenite**
Initial austenitizing at a temperature of…	1750 ˚F	1750 ˚F	1750 ˚F
Quenching and re-austenitizing at a temperature of…	1425 ˚F	1540 ˚F	N/A
Quenching followed by tempering at a temperature of…	360 ˚F	360 ˚F	360 ˚F
Temper for a duration of…	1 hr	1 hr	1 hr

A schematic of the heat treatment processes for the different volume fractions is depicted in Figure 40. From top to bottom are the 35%, 22%, and 13% RA processes. Note that the distribution of primary carbides increases with decreasing volume fraction of RA.

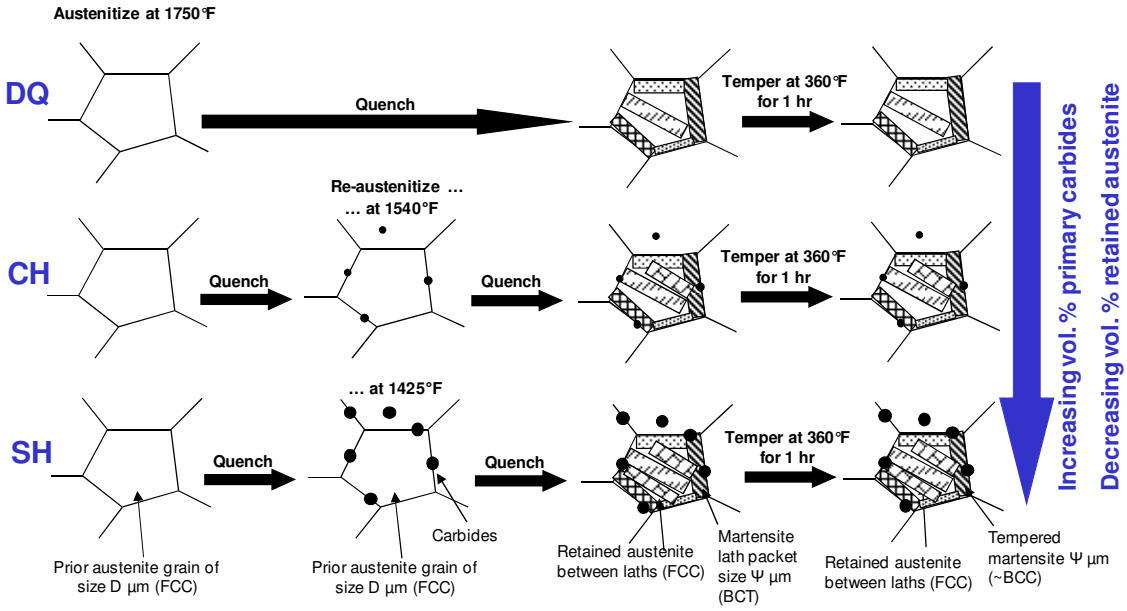

Figure 40. 41100 heat treatments.

The presence of retained austenite in 41100 becomes more apparent with increasing volume fraction of that phase. Note that the 13% RA specimen (Figure 41) closely resembles the 4145 due to the high percentage of martensite. As the volume fraction increases to 22% (Figure 42), visible portions of retained austenite (lighter shade areas) are detectable, and when increased to 35% RA (Figure 43), significant austenite is visible.

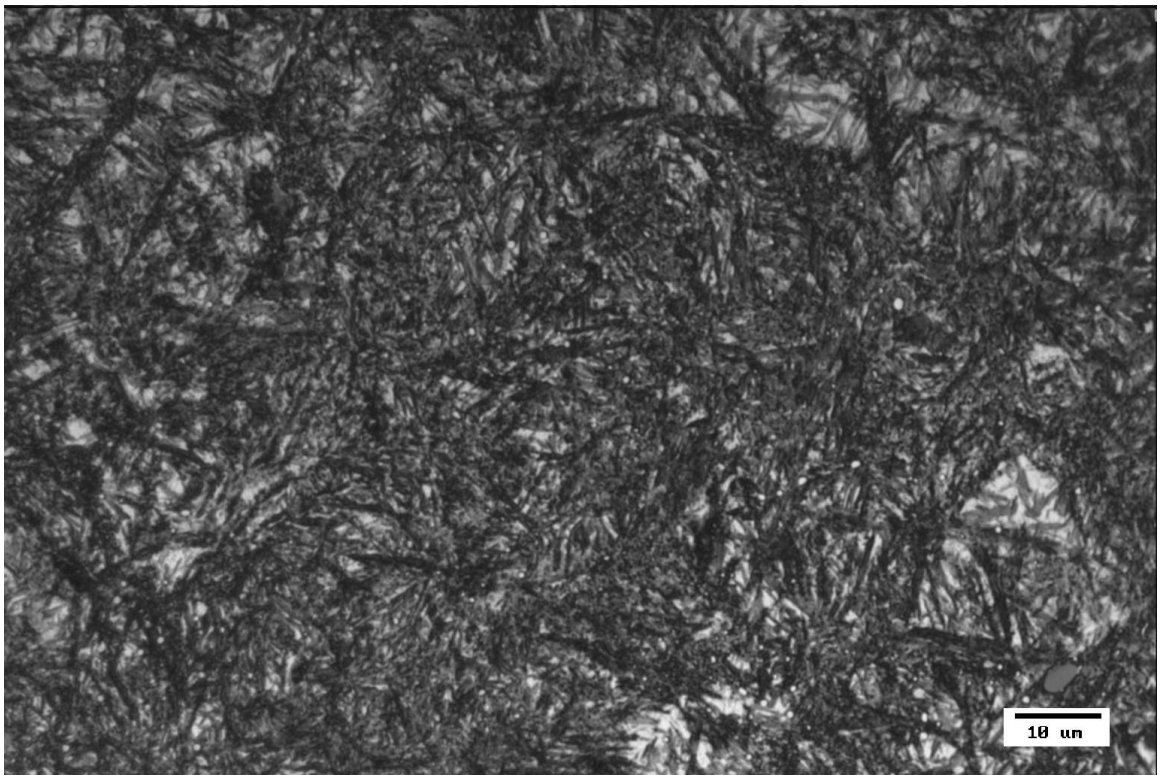

Figure 41. Micrograph of 41100 series steel with 13% initial retained austenite.

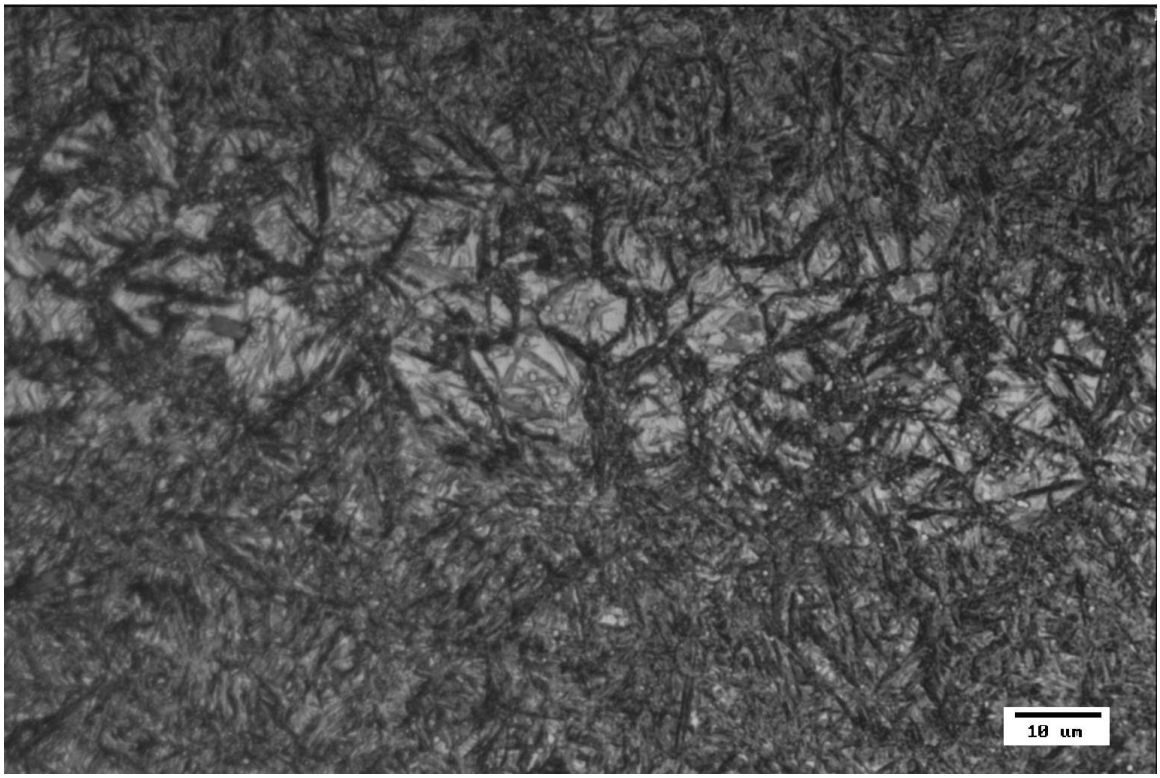

Figure 42. Micrograph of 41100 series steel with 22% initial retained austenite.

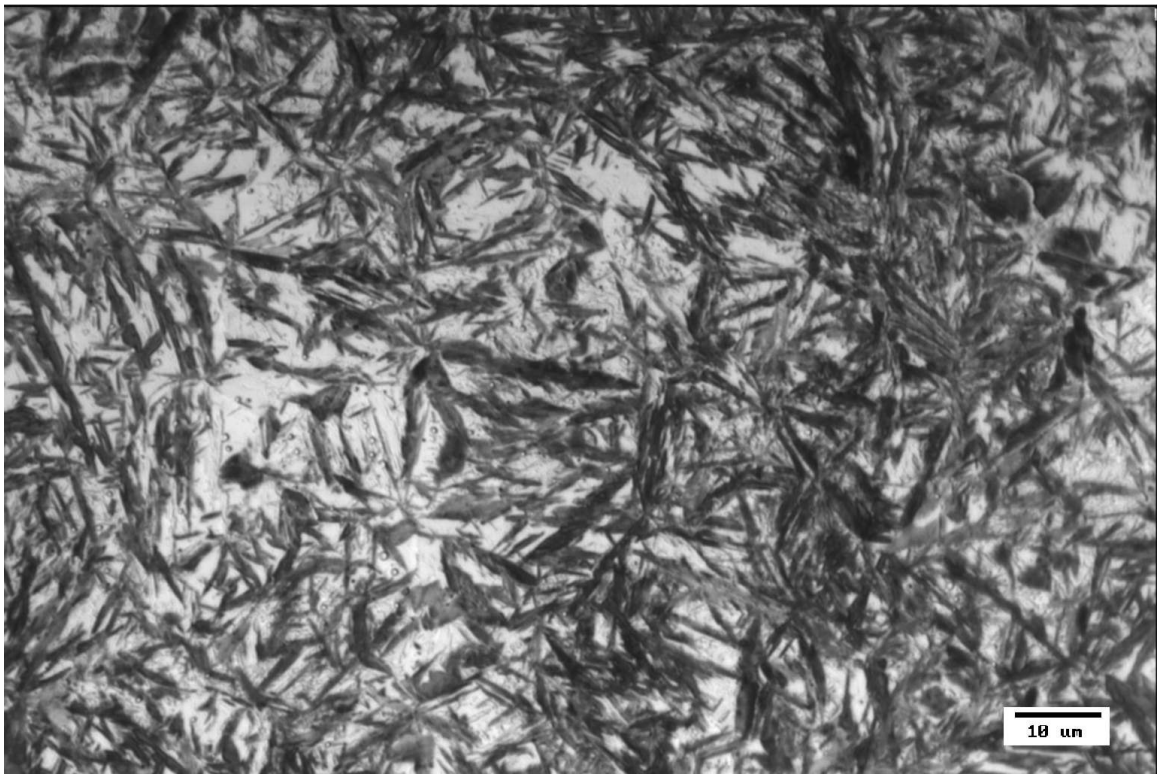

Figure 43. Micrograph of 41100 series steel with 35% initial retained austenite.

3.3.2 Multi-phase material representation

The microstructure of 41000 steel contains martensite laths with pockets of retained austenite within each (prior austenitic) grain, as depicted in Figure 37. A material model that advances the current state of the art must incorporate polycrystalline plasticity of martensite, as well as account for austenite-martensite transformation and the associated inelastic transform strains. Two methods of producing the desired combination of behaviors are explicit modeling and hybrid modeling.

Previous work has been done with two-phase materials in which plasticity occurs uniquely in each phase [59], but has not incorporated a transform component. In such a formulation with a transformation component, individual elements would be designated

as austenite or martensite, and a transform would occur when a critical driving stress was reached, changing that element from one phase to the other. It is difficult to represent the lath martensite structure with explicit modeling because it requires extremely fine meshes, which are not feasible for practical problem involving a large number of grains or packets. Utilizing a practical size mesh presents a large challenge with this type of scheme. Elements must be scaled considerably smaller than the grain size, since the lath martensite structure contains both phases in a single grain. Therefore, such a method would not be feasible for this study.

Alternatively, a hybrid approach is introduced here to account for evolution of volume fraction as well as crystal plasticity. In this technique, both crystal plasticity for the martensite and volumetric transform strain of austenite to martensite are calculated in a single element, with a variable tracking the evolution of transformed martensite. The kinematics is modeled using a triple multiplicative decomposition of the deformation gradient. Each homogenized element is capable of representing either a lath grain or an averaged response of a number of grains. Such a scheme allows scaling of elements from grain-size upwards as much as desired. Smaller mesh scales close to grain-size allow for examination of the localized plasticity caused by microstructural characteristics. Larger meshing scales will not produce visible localized responses, but take into account the response of many individual grains, and the element provides an averaged response. This allows the user to customize their scale to the desired amount of localized behavior on one end, to the desired speed and efficiency of larger scales on the other end.

3.3.3 Two-Phase Micro-Plasticity Material Model

The new two-phase hybrid model is built around a triple multiplicative decomposition of the deformation gradient $\underset{\sim}{F}$, given as

$$\underset{\sim}{F} = \underset{\sim}{F}^{e} \cdot \underset{\sim}{F}^{p} \cdot \underset{\sim}{F}^{tr} \tag{35}$$

where $\underset{\sim}{F}^{tr}$ accounts for the volumetric strain produced by the austenite-martensite phase transformation, and $\underset{\sim}{F}^{p}$ accounts for polycrystalline plasticity in the martensite. Plasticity and transformation occur along slip and transformation systems associated with the lattice structures of the martensite and austenite. The evolution of the crystal plasticity follows the formulation work of Asaro [5] in Equations (9) through (15). The model uses the 48 BCC slip systems to approximate the behavior of the BCT tempered martensite found in the 41XXX steels, which are found in Appendix A. The transformation is controlled by a formulation based on Suiker and Turtletaub [50], given in Equations (17) through (26). These equations are calculated on the 24 FCC transform systems for austenite-to-martensite transformation, listed in Appendix B.

Upon examination of these formulations individually, it can be seen that the critical stress for transformation and micro-plasticity are based on the Cauchy stress $\underset{\sim}{\sigma}$. Therefore, a priority must be assigned for the two inelastic behaviors calculated. Since the austenite is a softer phase of material and the transform thresholds are generally lower than plastic deformation of martensite, this model assumes that transformation is given priority in the hierarchy of the algorithm. The hierarchy is also denoted by the position of the transform deformation gradient $\underset{\sim}{F}^{tr}$ on the far right-hand side of Equation (35).

This necessitates a two-step procedure for modeling the combined behavior in a displacement-based finite element code such as ABAQUS [1], used herein. The total deformation gradient at the beginning and end of each time step are input, and the tangent modulus must be determined in a manner consistent with Equation (35). The transformation strain increment, if present within a given time step, is determined first via an iterative Newton-Raphson method. During this iteration, the plastic deformation gradient does not vary. Subsequently, the stress is re-calculated and the plastic deformation is iterated to balance the external load. Hence, this procedure can be viewed as two-step iterative approach reducing the slope of the response for a fixed strain increment, as illustrated in Figure 44.

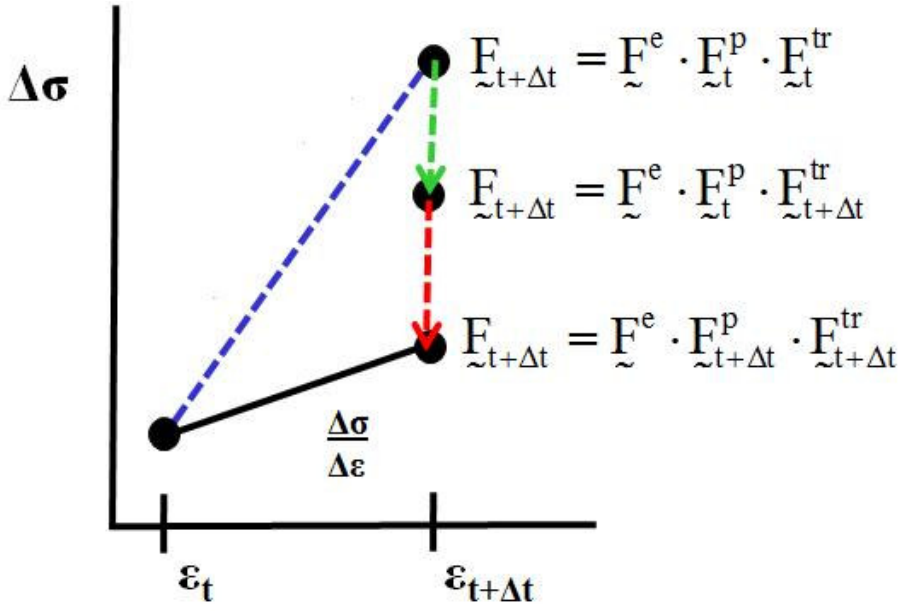

Figure 44. Hierarchy of iterations containing transform and plasticity.

3.3.4 Algorithmic Treatment

The two-phase formulation is implemented via an implicit integration algorithm. This was chosen because an explicit algorithm at the low rate-dependence cases

investigated would require extremely small steps and thus not be practical. The model evaluates the shearing rates $\dot{\gamma}^{(\alpha)}$ and transform rates $\dot{\xi}^{(\lambda)}$ at the end of the given time step, which requires an iterative process, since the terms in Equations (13) and (20) are dependent on $\dot{\gamma}^{(\alpha)}$ and $\dot{\xi}^{(\lambda)}$. The implicit martensitic crystal plasticity portion of the algorithm follows the method laid out by McGinty [33], using a Newton-Raphson iterative technique and scaled error norm to judge iteration convergence. The formulation is coded in an ABAQUS user material subroutine called UMAT. A flow chart depicting the sequence of calculations is given in Figure 45.

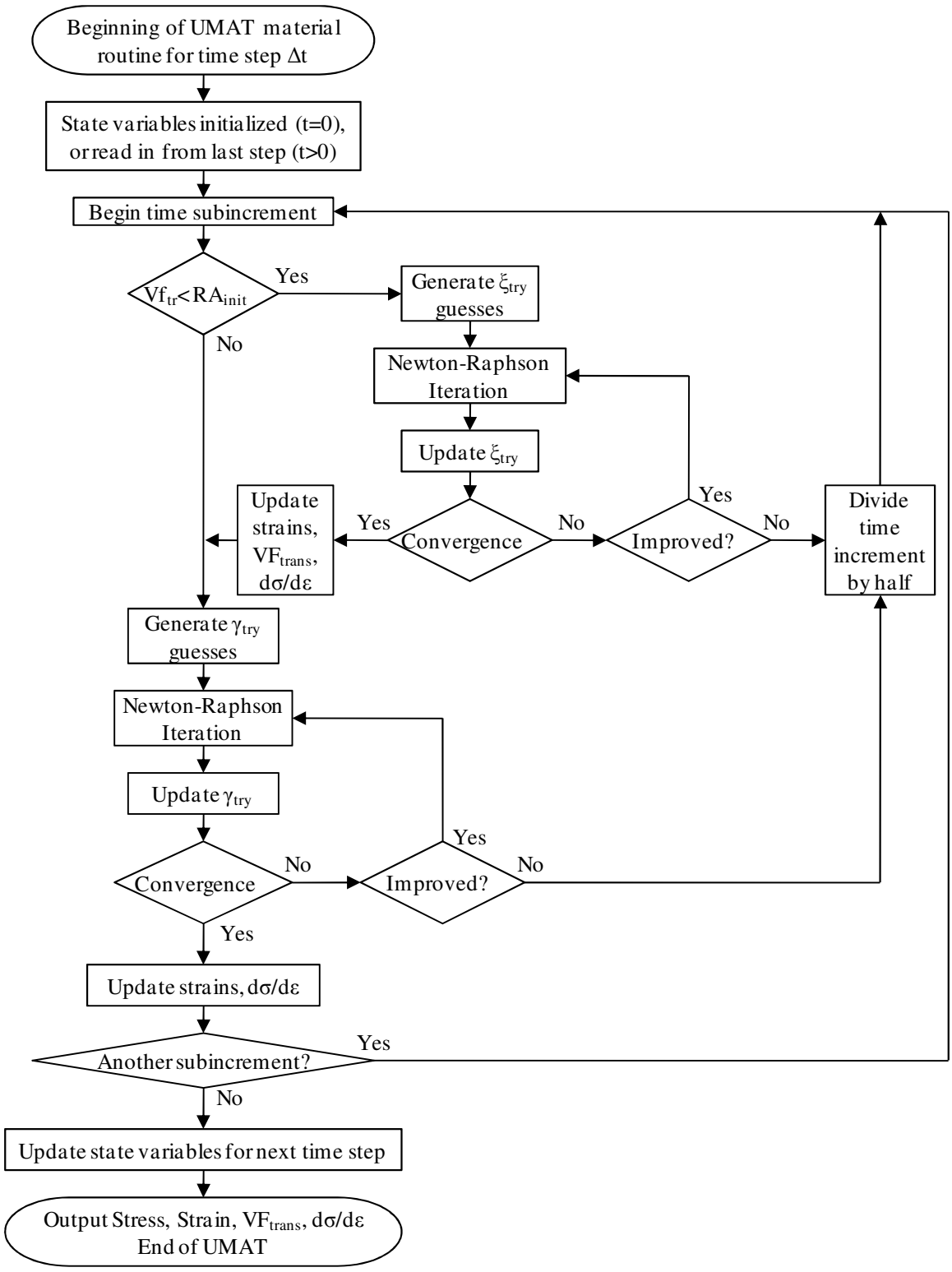

Figure 45. Flow diagram for user material routine UMAT.

3.3.4.1 Algorithm Inputs and Preliminary Calculations

For a given time step Δt, the deformation gradients at the beginning and end of the time step, $\underset{\sim}{F}_t$ and $\underset{\sim}{F}_{t+\Delta t}$, are input into the UMAT. Herein, all subscripts t denote values at the previous step, and $t+\Delta t$ indicate the current time step. The user-defined inputs for the code are listed in Table 5.

Table 5. List of input parameters for UMAT.

Elastic Properties	**Martensitic Crystal Plasticity Properties**	**Austenitic Transform Plasticity Properties**	**Microstructure and Orientation Properties**
C_{11}^0	$\dot{\gamma}_0$	$\dot{\xi}_{max}$	gcn
C_{12}^0	m	ν_{tr}	φ_{euler}
C_{44}^0	$g_0^{(\alpha)}$	$\left(f_{cr}^{(\lambda)}\right)_0$	θ_{euler}
	H_{dir} and H_{dyn}	Q	ψ_{euler}
	$\chi_0^{(\alpha)}$	$RA_{initial}$	
	A_{dir} and A_{dyn}	γ_T	

The three elastic constants C_{11}^0, C_{12}^0, and C_{44}^0 form the elasticity tensor. Three constants are used in order to allow for transverse isotropy to be applied, as an available feature of the code. However, in the demonstration cases used in this study, a fully isotropic elastic tensor is used. Initial values for the back, drag, and critical driving stresses are given by $\chi_0^{(\alpha)}$, $g_0^{(\alpha)}$, and $\left(f_{cr}^{(\lambda)}\right)_0$, and are initially the same for all slip and transform systems, respectively. The "gcn" (grain control number) input is an integer option which controls the microstructural scaling of an individual element, according to Table 6. Depending on the gcn option selected, orientation of the element's lattice structure is either input by the

user or randomly assigned by the code. To accomplish this, the code contains 6000 grain orientations pre-defined, which have been created outside the code and checked for a varied distribution. The code randomly selects an orientation or orientations for each element, and only repeats them if more than 6000 orientations are required. The Euler angles φ_{euler}, θ_{euler}, and ψ_{euler}, depicted in Figure 46, give the rotation sequence for the local crystalline lattice structure coordinate directions (shown in red) in terms of the global coordinate directions (shown in blue).

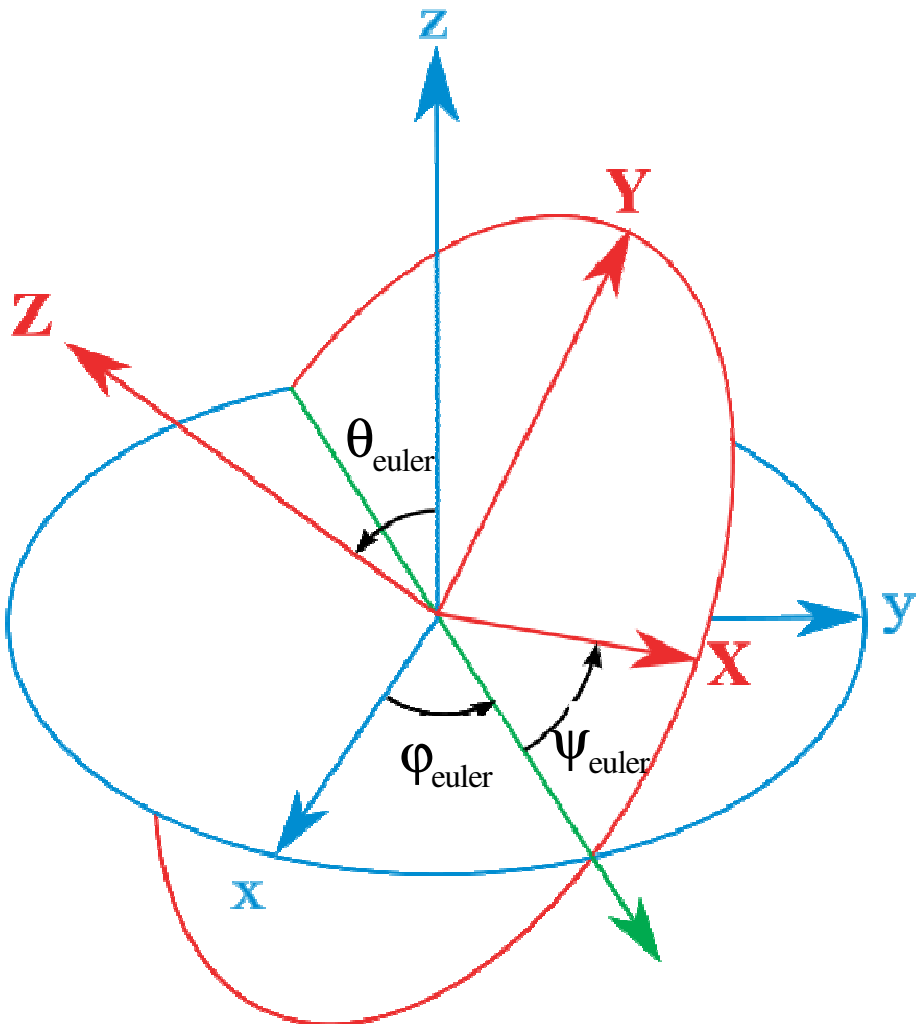

Figure 46. Euler angle definitions between local lattice coordinates and global coordinates.

They are specified by the user in the input file for an gcn choice of 0; otherwise these inputs are ignored. All other inputs in Table 5 are as previously defined.

Table 6. Option gcn choices.

gcn	option
0	Single grain orientation per element, orientation from input Euler angles
1	Single grain orientation per element, randomly generated Euler angles
> 1	gcn grain orientations per element, response averaged over grains, randomly generated Euler angles

For a gcn input of greater than 1, all calculations described are performed gcn times, once for each grain orientation. The multiple grain data in an element is tracked separately for the next time step, and only averaged for outputting of strain and transformation data.

After reading the inputs, either from Table 5, or from computed values from the previous time step, the code begins calculations by converting parameters in local orientations to global directions, as all calculations are performed in global coordinates. The rotation tensor $\underset{\sim}{R}$ contains the direction cosines between local and global coordinate systems, as defined by the input or randomly generated Euler angles. The elasticity tensor, slip directions, slip plane normals, transformation directions, and the habit plane normals are all rotated according to

$$C_{ijkl} = R_{ip} \cdot R_{jq} \cdot C^{0}_{prqs} \cdot R_{kr} \cdot R_{ls} \tag{36}$$

$$\underset{\sim}{s}^{(\alpha)}_{0} = \underset{\sim}{R} \cdot \underset{\sim}{s}^{(\alpha)}_{L} \tag{37}$$

$$\underset{\sim}{m}_0^{(\alpha)} = \underset{\sim}{R} \cdot \underset{\sim}{m}_L^{(\alpha)} \tag{38}$$

$$\hat{\underset{\sim}{b}}_0^{(\alpha)} = \underset{\sim}{R} \cdot \hat{\underset{\sim}{b}}_L^{(\alpha)} \tag{39}$$

$$\underset{\sim}{n}_0^{(\alpha)} = \underset{\sim}{R} \cdot \underset{\sim}{n}_L^{(\alpha)} \tag{40}$$

where all L subscripts denote local directions on the unit vectors, and $\underset{\sim}{C}^0$ is the elasticity tensor in local coordinates.

The algorithm then begins by checking the current value of V_{trans}, as defined in Equation (22). If V_{trans} is less than the initial retained austenite amount, $RA_{initial}$, the code performs transform iterations to check if any transform occurs over the current time increment. If the value of V_{trans} has already reached $RA_{initial}$, the microstructure is fully martensitic and the transform section is skipped over, the previous time step's transform deformation gradient, $\underset{\sim}{F}_t^{tr}$, is set as the current step's $\underset{\sim}{F}_{t+\Delta t}^{tr}$, and the algorithm moves on to martensitic plasticity.

3.3.4.2 Transformation Iterations

Upon entering the transformation section, an initial guess value for the transformation rates must be calculated to give a starting point for the Newton-Raphson iterations. This is accomplished by using values from the previous time step, beginning with the elastic deformation gradient,

$$\underset{\sim}{F}_t^e = \underset{\sim}{F}_t \cdot \left(\underset{\sim}{F}_t^{tr}\right)^{-1} \cdot \left(\underset{\sim}{F}_t^p\right)^{-1} \tag{41}$$

which is then used to calculate the transformation directions and habit plane normals in the current configuration according to the following:

$$\hat{\underset{\sim}{b}}_t^{(\alpha)} = \underset{\sim}{F}_t^e \cdot \hat{\underset{\sim}{b}}_0^{(\alpha)} \tag{42}$$

$$\underset{\sim}{n}_t^{(\alpha)} = \left(\underset{\sim}{F}_t^e\right)^{-T} \cdot \underset{\sim}{n}_0^{(\alpha)} \tag{43}$$

The elastic strain is also calculated,

$$\underset{\sim}{E}_t^e = \frac{1}{2}\left(\left(\underset{\sim}{F}_t^e\right)^T \cdot \underset{\sim}{F}_t^e - \underset{\sim}{I}\right) \tag{44}$$

and used to determine the second Piola-Kirchoff stress and Cauchy stress at time t,

$$\underset{\sim}{S}_t^{PK} = \underset{\sim}{C} : \underset{\sim}{E}_t^e \tag{45}$$

$$\underset{\sim}{\sigma}_t = \frac{1}{\left|\underset{\sim}{F}_t^e\right|}\left(\underset{\sim}{F}_t^e \cdot \underset{\sim}{S}_t^{PK} \cdot \left(\underset{\sim}{F}_t^e\right)^T\right) \tag{46}$$

Using the Cauchy stress from the previous time step, guess values for the transformation driving stresses are calculated by

$$\left(f_{tr}^{(\lambda)}\right)_t = \underset{\sim}{\sigma}_t : \left(\gamma_T \cdot \underset{\sim}{\hat{b}}_t^{(\lambda)} \otimes \underset{\sim}{n}_t^{(\lambda)}\right) \tag{47}$$

The driving stresses are then plugged into the transformation rate equations to determine initial guess values, denoted $\dot{\xi}_{try}^{(\lambda)}$, on each transform system according to

$$\dot{\xi}_{try}^{(\lambda)} = \dot{\xi}_{max} \cdot \tanh\left(\frac{1}{\nu_{tr}} \cdot \frac{\left\langle\left(f_{tr}^{(\lambda)}\right)_t - \left(f_{cr}^{(\lambda)}\right)_t\right\rangle}{\left(f_{cr}^{(\lambda)}\right)_t}\right) \tag{48}$$

With a guess value generated, the Newton-Raphson loop is now entered. The loop iterates until values of $\dot{\xi}_{try}^{(\lambda)}$ produce error norms within a tolerance specified in the code (set to 1.0 x 10^{-5}). The loop begins with the calculation of these norms, with updated values of all other variables based on the $\dot{\xi}_{try}^{(\lambda)}$ values. First, the transform deformation gradient is updated by the following:

$$\underset{\sim}{F}_{t+\Delta t}^{tr} = \underset{\sim}{F}_t^{tr} + \sum_{\lambda=1}^{N_{trans}} \dot{\xi}_{try}^{(\lambda)} \cdot \left(\gamma_T \cdot \underset{\sim}{\hat{b}}_0^{(\lambda)} \otimes \underset{\sim}{n}_0^{(\lambda)}\right) \cdot \Delta t \tag{49}$$

This new value is used to update the driving stresses to the current time step. The martensitic plastic deformation gradient is left at the previous time step. This is due to the hierarchy proposed that the stress-assisted transformation is given priority. Following calculation of any existing transform under the current load, the plasticity will then be calculated with the final $\underset{\sim}{F}^{tr}_{t+\Delta t}$ for the time step fixed. Utilizing the $\underset{\sim}{F}^{tr}_{t+\Delta t}$ calculated from Equation (49), the transform direction and habit plane normal vectors, elastic strain, Piola-Kirchoff and Cauchy stresses, and the driving stress for transformation are calculated as follows:

$$\underset{\sim}{F}^{e}_{t+\Delta t} = \underset{\sim}{F}_{t+\Delta t} \cdot \left(\underset{\sim}{F}^{tr}_{t+\Delta t}\right)^{-1} \cdot \left(\underset{\sim}{F}^{p}_{t}\right)^{-1} \tag{50}$$

$$\hat{\underset{\sim}{b}}^{(\alpha)}_{t+\Delta t} = \underset{\sim}{F}^{e}_{t+\Delta t} \cdot \hat{\underset{\sim}{b}}^{(\alpha)}_{0} \tag{51}$$

$$\underset{\sim}{n}^{(\alpha)}_{t+\Delta t} = \left(\underset{\sim}{F}^{e}_{t+\Delta t}\right)^{-T} \cdot \underset{\sim}{n}^{(\alpha)}_{0} \tag{52}$$

$$\underset{\sim}{E}^{e}_{t+\Delta t} = \frac{1}{2}\left(\left(\underset{\sim}{F}^{e}_{t+\Delta t}\right)^{T} \cdot \underset{\sim}{F}^{e}_{t+\Delta t} - \underset{\sim}{I}\right) \tag{53}$$

$$\underset{\sim}{S}^{PK}_{t+\Delta t} = \underset{\sim}{C} : \underset{\sim}{E}^{e}_{t+\Delta t} \tag{54}$$

$$\underset{\sim}{\sigma}_{t+\Delta t} = \frac{1}{\left|\underset{\sim}{F}^{e}_{t+\Delta t}\right|}\left(\underset{\sim}{F}^{e}_{t+\Delta t} \cdot \underset{\sim}{S}^{PK}_{t+\Delta t} \cdot \left(\underset{\sim}{F}^{e}_{t+\Delta t}\right)^{T}\right) \tag{55}$$

$$\left(f_{tr}{}^{(\lambda)}\right)_{t+\Delta t} = \underset{\sim}{\sigma}_{t+\Delta t} : \left(\gamma_{T} \cdot \hat{\underset{\sim}{b}}^{(\lambda)}_{t+\Delta t} \otimes \underset{\sim}{n}^{(\lambda)}_{t+\Delta t}\right) \tag{56}$$

This results in values of $f_{tr}{}^{(\lambda)}$ based on the assumed values for $\dot{\xi}^{(\lambda)}_{try}$. The critical driving stresses are also updated according to

$$\left(f_{cr}{}^{(\lambda)}\right)_{t+\Delta t} = \left(f_{cr}{}^{(\lambda)}\right)_{t} + \sum_{\eta=1}^{N_{trans}} Q \cdot \dot{\xi}_{try}{}^{(\eta)} \cdot \Delta t \tag{57}$$

Now all parameters have been updated to reflect the current time step according to the transform rates $\dot{\xi}_{try}^{(\lambda)}$. A set of error functions are then created by re-arranging Equation (20) to get

$$Err_1^{(\lambda)} = \tanh\left(\frac{1}{\nu_{tr}} \cdot \frac{\left\langle \left(f_{tr}^{(\lambda)}\right)_{t+\Delta t} - \left(f_{cr}^{(\lambda)}\right)_{t+\Delta t} \right\rangle}{\left(f_{cr}^{(\lambda)}\right)_{t+\Delta t}} \right) - \frac{\dot{\xi}_{try}^{(\lambda)}}{\dot{\xi}_{max}} \tag{58}$$

The Newton-Raphson method will use these equations and their derivatives to update $\dot{\xi}_{try}^{(\lambda)}$ in the next loop. A scaled error norm SSE_1 is then calculated based on these residuals. If any of $\dot{\xi}_{try}^{(\lambda)}$ are greater than zero, it is defined as

$$SSE_1 = \frac{1}{N_{trans}} \sqrt{\sum_{\lambda=1}^{N_{trans}} \left(\frac{\dot{\xi}_{try}^{(\lambda)}}{\dot{\xi}_{big}} \cdot Err_1^{(\lambda)} \right)^2} \tag{59}$$

where $\dot{\xi}_{big}$ is given by

$$\dot{\xi}_{big} = \max\left(\dot{\xi}_{try}^{(\lambda)}\right), \lambda = 1...N_{trans} \tag{60}$$

In the event that all $\dot{\xi}_{try}^{(\lambda)}$ are zero, then SSE_1 is set at zero. This error norm based on the current guess $\dot{\xi}_{try}^{(\lambda)}$ is then saved as a reference error for the loop:

$$SSE_{Ref} = SSE_1 \tag{61}$$

Now the loop creates updated guess values of the transformation rates. To accomplish this, the code calculates the partial derivatives of the residuals given by Equation (58) with respect to each transform rate. Note that these derivatives must account for the Macauley brackets and thus have two possible formulations based on the values of $\left(f_{tr}^{(\lambda)}\right)_{t+\Delta t}$ and $\left(f_{cr}^{(\lambda)}\right)_{t+\Delta t}$. If the Macauley brackets yield a positive value, then

$$\frac{\partial \mathrm{Err}_1^{(\lambda)}}{\partial \dot{\xi}^{(\eta)}} = \left(\text{coefficient}\right) \cdot \frac{\dfrac{\partial f_{tr}^{(\lambda)}}{\partial \dot{\xi}^{(\eta)}} - \dfrac{\partial f_{cr}^{(\lambda)}}{\partial \dot{\xi}^{(\eta)}} \cdot \left(1 + \dfrac{\left\langle \left(f_{tr}^{(\lambda)}\right)_{t+\Delta t} - \left(f_{cr}^{(\lambda)}\right)_{t+\Delta t} \right\rangle}{\left(f_{cr}^{(\lambda)}\right)_{t+\Delta t}} \right)}{\nu_{tr} \cdot \left(f_{cr}^{(\lambda)}\right)_{t+\Delta t}} - \frac{1}{\dot{\xi}_{max}} \qquad (62)$$

$$\text{if} \quad \left(f_{tr}^{(\lambda)}\right)_{t+\Delta t} > \left(f_{cr}^{(\lambda)}\right)_{t+\Delta t}$$

where the coefficient is

$$\text{coefficient} = 1 - \tanh^2 \left(\frac{\left\langle \left(f_{tr}^{(\lambda)}\right)_{t+\Delta t} - \left(f_{cr}^{(\lambda)}\right)_{t+\Delta t} \right\rangle}{\nu_{tr} \cdot \left(f_{cr}^{(\lambda)}\right)_{t+\Delta t}} \right) \qquad (63)$$

If the Macaulay brackets give zero, then

$$\frac{\partial \mathrm{Err}_1^{(\lambda)}}{\partial \dot{\xi}^{(\eta)}} = -\frac{1}{\dot{\xi}_{max}} \quad \text{if} \quad \left(f_{tr}^{(\lambda)}\right)_{t+\Delta t} \le \left(f_{cr}^{(\lambda)}\right)_{t+\Delta t} \qquad (64)$$

Equation (62) contains various derivatives which must be defined. The derivative of the critical driving stress with respect to transform rates can be computed based on Equation (26), and is given by

$$\frac{\partial f_{cr}^{(\lambda)}}{\partial \dot{\xi}^{(\eta)}} = Q \cdot \Delta t \qquad (65)$$

The calculation of the driving stress derivatives is based on Equation (17), but is more difficult because the Cauchy stress, transform directions and habit plane normals in the current configuration are all dependent on $\dot{\xi}^{(\eta)}$. As noted by McGinty [33], by neglecting higher-order terms, the derivative can be simplified. Using these assumptions, the driving stress derivative can be given as

$$\frac{\partial f_{tr}^{(\lambda)}}{\partial \dot{\xi}^{(\eta)}} \cong -\left(\gamma_T \cdot \underset{\sim}{\hat{b}}_0^{(\lambda)} \otimes \underset{\sim}{n}_0^{(\lambda)}\right) : \underset{\sim}{C} : \left(\gamma_T \cdot \underset{\sim}{\hat{b}}_0^{(\eta)} \otimes \underset{\sim}{n}_0^{(\eta)}\right) \qquad (66)$$

The estimates for the transform rates are now updated in the Newton-Raphson loop by solving a series of simultaneous equations over all transform systems, given by

$$\mathrm{Err}_{\mathrm{l}}^{(\lambda)} = -\sum_{\eta=1}^{N_{\mathrm{trans}}} \frac{\partial \mathrm{Err}_{\mathrm{l}}^{(\lambda)}}{\partial \dot{\xi}^{(\eta)}} \cdot \Delta\dot{\xi}^{(\eta)} \tag{67}$$

where $\Delta\dot{\xi}^{(\eta)}$ is the change in the estimated value of the transform rate. The change values are added to the previous guess value (denoted iteration n), to give the new estimated transform rates (denoted n+1):

$$\left(\dot{\xi}_{\mathrm{try}}^{(\lambda)}\right)_{\mathrm{n+1}} = \left(\dot{\xi}_{\mathrm{try}}^{(\lambda)}\right)_{\mathrm{n}} + \Delta\dot{\xi}^{(\lambda)} \tag{68}$$

Using these new values of $\dot{\xi}_{\mathrm{try}}{}^{(\lambda)}$, Equations (49) through (59) are then re-calculated. The new $\mathrm{SSE}_{\mathrm{l}}$ is compared to $\mathrm{SSE}_{\mathrm{Ref}}$, to check for improvement. If there is not improvement, the code reduces the time increment by half, and returns to the top of the algorithm to calculate the new smaller sub-increment, as many divisions as is necessary to converge. If there is improvement, then the code checks to see if the $\mathrm{SSE}_{\mathrm{l}}$ error norm value is within tolerance. If tolerance is not achieved, another Newton-Raphson iteration is performed by returning to Equation (49) with the new value of $\dot{\xi}_{\mathrm{try}}{}^{(\lambda)}$. If convergence has been achieved within tolerance, then the values for $\dot{\xi}_{\mathrm{try}}{}^{(\lambda)}$ are the accepted values for the current time step:

$$\dot{\xi}_{\mathrm{t+\Delta t}}^{(\lambda)} = \left(\dot{\xi}_{\mathrm{try}}^{(\lambda)}\right)_{\mathrm{n+1}} \quad \text{if} \quad \mathrm{SSE}_{\mathrm{l}} \le \text{tolerance} \tag{69}$$

The volume fraction transform amounts on each transform system are then updated based on the time increment, along with the total transform amount, the transformation strains and the rate of transform deformation with respect to stress rate tensor:

$$\Delta\xi^{(\lambda)} = \dot{\xi}_{\mathrm{t+\Delta t}}^{(\lambda)} \cdot \Delta\mathrm{t} \tag{70}$$

$$\xi_{\mathrm{t+\Delta t}}^{(\lambda)} = \xi_{\mathrm{t}}^{(\lambda)} + \Delta\xi^{(\lambda)} \tag{71}$$

$$\left(V_{trans}\right)_{t+\Delta t} = \left(V_{trans}\right)_t + \sum_{\lambda=1}^{N_{trans}} \Delta\xi^{(\lambda)} \tag{72}$$

$$\underset{\sim}{E}^{tr}_{t+\Delta t} = \underset{\sim}{E}^{tr}_t + \sum_{\lambda=1}^{N_{trans}} \Delta\xi^{(\lambda)} \cdot \gamma_T \cdot \left(\hat{\underset{\sim}{b}}^{(\lambda)}_{t+\Delta t} \otimes \underset{\sim}{n}^{(\lambda)}_{t+\Delta t}\right)_{sym} \tag{73}$$

where

$$\left(\hat{\underset{\sim}{b}}^{(\lambda)}_{t+\Delta t} \otimes \underset{\sim}{n}^{(\lambda)}_{t+\Delta t}\right)_{sym} = \frac{1}{2} \cdot \left[\left(\hat{\underset{\sim}{b}}^{(\lambda)}_{t+\Delta t} \otimes \underset{\sim}{n}^{(\lambda)}_{t+\Delta t}\right) + \left(\underset{\sim}{n}^{(\lambda)}_{t+\Delta t} \otimes \hat{\underset{\sim}{b}}^{(\lambda)}_{t+\Delta t}\right)\right] \tag{74}$$

The rate of transform deformation with respect to stress rate tensor, given by

$$\frac{\partial \underset{\sim}{D}^{tr}}{\partial \dot{\underset{\sim}{\sigma}}} = \sum_{\lambda=1}^{N_{trans}} \frac{\partial \underset{\sim}{D}^{tr}}{\partial \dot{\xi}^{(\lambda)}} \cdot \frac{\partial \dot{\xi}^{(\lambda)}}{\partial f_{tr}^{(\lambda)}} \cdot \frac{\partial f_{tr}^{(\lambda)}}{\partial \underset{\sim}{\sigma}} \cdot \frac{\partial \underset{\sim}{\sigma}}{\partial \dot{\underset{\sim}{\sigma}}} \tag{75}$$

where

$$\frac{\partial \underset{\sim}{D}^{tr}}{\partial \dot{\xi}^{(\lambda)}} = \gamma_T \cdot \left(\hat{\underset{\sim}{b}}^{(\lambda)}_{t+\Delta t} \otimes \underset{\sim}{n}^{(\lambda)}_{t+\Delta t}\right)_{sym} \tag{76}$$

$$\frac{\partial f_{tr}^{(\lambda)}}{\partial \underset{\sim}{\sigma}} = \gamma_T \cdot \left(\hat{\underset{\sim}{b}}^{(\lambda)}_{t+\Delta t} \otimes \underset{\sim}{n}^{(\lambda)}_{t+\Delta t}\right)_{sym} \tag{77}$$

will be used later in calculating the tangent modulus. Note that the partial derivative of stress with respect to the stress rate for the discretized time step is Δt.

$$\frac{\partial \underset{\sim}{\sigma}}{\partial \dot{\underset{\sim}{\sigma}}} = \Delta t \tag{78}$$

The value of $\frac{\partial \dot{\xi}^{(\lambda)}}{\partial f_{tr}^{(\lambda)}}$ requires careful treatment due to presence of the Macaulay bracket in Equation (20), and thus has two possible definitions.

$$\frac{\partial \dot{\xi}^{(\lambda)}}{\partial f_{tr}^{(\lambda)}} = \left[\text{coefficient}\right] \cdot \frac{\dot{\xi}_{max}}{\nu_{tr} \cdot \left(f_{cr}^{(\lambda)}\right)_{t+\Delta t}} \quad \text{if} \quad \left(f_{tr}^{(\lambda)}\right)_{t+\Delta t} > \left(f_{cr}^{(\lambda)}\right)_{t+\Delta t}$$

$$\frac{\partial \dot{\xi}^{(\lambda)}}{\partial f_{tr}^{(\lambda)}} = 0 \quad \text{if} \quad \left(f_{tr}^{(\lambda)}\right)_{t+\Delta t} \leq \left(f_{cr}^{(\lambda)}\right)_{t+\Delta t} \tag{79}$$

where the coefficient was defined in Equation (63). The transformation portion of the time step is now complete, and the code moves on to the martensitic crystal plasticity calculations.

3.3.4.3 Crystal Plasticity Iterations

Following the completion of transform section, the code then moves into the crystal plasticity algorithm to determine the plastic strain in the martensite. This section of the code follows the work of McGinty [33], and as with the transform calculations, begins with guess values for the shearing rates for the Newton-Raphson iterations. Like the transform section, the values from the previous time step for $\underset{\sim}{F}_t$ and $\underset{\sim}{F}_t^p$ are used to determine the initial guess. However, the transform deformation gradient for the step has already been calculated and is now considered fixed. Thus, the Newton-Raphson iterations will use the current value, $\underset{\sim}{F}_{t+\Delta t}^{tr}$, fixed throughout the plasticity loop:

$$\underset{\sim}{F}_t^e = \underset{\sim}{F}_t \cdot \left(\underset{\sim}{F}_{t+\Delta t}^{tr}\right)^{-1} \cdot \left(\underset{\sim}{F}_t^p\right)^{-1} \tag{80}$$

The $\underset{\sim}{F}_t^e$ tensor is then used to transform the slip directions and slip plane normals from the intermediate to the current configuration:

$$\underset{\sim}{s}_t^{(\alpha)} = \underset{\sim}{F}_t^e \cdot \underset{\sim}{s}_0^{(\alpha)} \tag{81}$$

$$\underset{\sim}{m}_t^{(\alpha)} = \left(\underset{\sim}{F}_t^e\right)^{-T} \cdot \underset{\sim}{m}_0^{(\alpha)} \tag{82}$$

The elastic strain is then calculated and used to evaluate the second Piola-Kirchoff stress and Cauchy stresses, as defined in Equations (44) through (46). The Cauchy stress is then inserted into the resolved shear stress equation, resulting in the initial guess values for the Newton iterations, as described by

$$\tau_t^{(\alpha)} = \underset{\sim}{\sigma}_t : \left(\underset{\sim}{s}_t^{(\alpha)} \otimes \underset{\sim}{m}_t^{(\alpha)} \right) \tag{83}$$

With the resolved shear stresses estimated, the shearing rates initial guess values on each slip system α, denoted $\dot{\gamma}_{try}^{(\alpha)}$, are calculated according to

$$\dot{\gamma}_{try}^{(\alpha)} = \dot{\gamma}_0 \cdot \left| \frac{\tau_t^{(\alpha)} - \chi_t^{(\alpha)}}{g_t^{(\alpha)}} \right|^m \cdot \text{sign}\left(\tau_t^{(\alpha)} - \chi_t^{(\alpha)} \right) \tag{84}$$

The code now has a starting point for the Newton-Raphson iterative loops. The loop iterates until the estimates for $\dot{\gamma}_{try}^{(\alpha)}$ return error norms below the user-defined tolerance. The loop begins with the calculation of the error norms, with the re-calculated values of all variables based on $\dot{\gamma}_{try}^{(\alpha)}$, similar to the transform section. In order to update the plastic deformation gradient, the plastic velocity gradient must first be calculated according to

$$\underset{\sim}{L}_0^P = \sum_{\alpha=1}^{N_{slip}} \dot{\gamma}_{try}^{(\alpha)} \cdot \left(\underset{\sim}{s}_0^{(\alpha)} \otimes \underset{\sim}{m}_0^{(\alpha)} \right) \tag{85}$$

The plastic velocity gradient is related to the plastic deformation gradient via the formulation in Equation (12). Since we are iterating over a discrete time step, for an implicit integration scheme, the relation can be described by

$$\underset{\sim}{F}_{t+\Delta t}^p = \exp\left(\underset{\sim}{L}_0^P \cdot \Delta t \right) \cdot \underset{\sim}{F}_t^p \tag{86}$$

where the exponential term in Equation (86) is calculated using a Taylor series expansion to second order.

$$\exp\left(\underset{\sim}{L}_0^P \cdot \Delta t\right) = \underset{\sim}{I} + \left(\underset{\sim}{L}_0^P \cdot \Delta t\right) \cdot \frac{\sin(\Omega)}{\Omega} + \left(\underset{\sim}{L}_0^P \cdot \underset{\sim}{L}_0^P \cdot \Delta t^2\right) \cdot \frac{1-\cos(\Omega)}{\Omega^2} \tag{87}$$

where

$$\Omega = \Delta t \cdot \sqrt{\frac{1}{2} \cdot \left(\underset{\sim}{L}_0^P : \underset{\sim}{L}_0^P\right)} \tag{88}$$

The updated value of $\underset{\sim}{F}^p_{t+\Delta t}$ is then used in re-calculating the resolved shear stress for the current time step using the following equations:

$$\underset{\sim}{F}^e_{t+\Delta t} = \underset{\sim}{F}_{t+\Delta t} \cdot \left(\underset{\sim}{F}^{tr}_{t+\Delta t}\right)^{-1} \cdot \left(\underset{\sim}{F}^p_{t+\Delta t}\right)^{-1} \tag{89}$$

$$\underset{\sim}{s}^{(\alpha)}_{t+\Delta t} = \underset{\sim}{F}^e_{t+\Delta t} \cdot \underset{\sim}{s}^{(\alpha)}_0 \tag{90}$$

$$\underset{\sim}{m}^{(\alpha)}_{t+\Delta t} = \left(\underset{\sim}{F}^e_{t+\Delta t}\right)^{-T} \cdot \underset{\sim}{m}^{(\alpha)}_0 \tag{91}$$

$$\underset{\sim}{E}^e_{t+\Delta t} = \frac{1}{2}\left(\left(\underset{\sim}{F}^e_{t+\Delta t}\right)^T \cdot \underset{\sim}{F}^e_{t+\Delta t} - \underset{\sim}{I}\right) \tag{92}$$

$$\underset{\sim}{S}^{PK}_{t+\Delta t} = \underset{\sim}{C} : \underset{\sim}{E}^e_{t+\Delta t} \tag{93}$$

$$\sigma_{t+\Delta t} = \frac{1}{\left|\underset{\sim}{F}^e_{t+\Delta t}\right|}\left(\underset{\sim}{F}^e_{t+\Delta t} \cdot \underset{\sim}{S}^{PK}_{t+\Delta t} \cdot \left(\underset{\sim}{F}^e_{t+\Delta t}\right)^T\right) \tag{94}$$

$$\tau^{(\alpha)}_{t+\Delta t} = \sigma_{t+\Delta t} : \left(\underset{\sim}{s}^{(\alpha)}_{t+\Delta t} \otimes \underset{\sim}{m}^{(\alpha)}_{t+\Delta t}\right) \tag{95}$$

This differs from the transform updates built on Equation (50) in that all components of the deformation gradient are now at the current time step. Since the transform has already been calculated, it is now fixed during the crystal plasticity calculations. The re-calculated $\tau^{(\alpha)}_{t+\Delta t}$ are now based on the current $\dot{\gamma}^{(\alpha)}_{try}$ values. Next, the drag and back stresses must evolve to the current time step, according to the hardening laws in

Equations (14) and (15). Discretized for the time increment, these updates are performed according to the following:

$$g_{t+\Delta t}^{(\alpha)} = \frac{g_t^{(\alpha)} + \sum_{\beta=1}^{N_{slip}} H_{dir} \cdot \left|\dot{\gamma}_{try}^{(\beta)}\right| \cdot \Delta t}{1 + \sum_{\beta=1}^{N_{slip}} H_{dyn} \cdot \left|\dot{\gamma}_{try}^{(\beta)}\right| \cdot \Delta t} \tag{96}$$

$$\chi_{t+\Delta t}^{(\alpha)} = \frac{\chi_t^{(\alpha)} + A_{dir} \cdot \dot{\gamma}_{try}^{(\alpha)} \cdot \Delta t}{1 + A_{dyn} \cdot \left|\dot{\gamma}_{try}^{(\alpha)}\right| \cdot \Delta t} \tag{97}$$

At this point, all of the parameters in Equation (13) have been updated for the current time step, based on the values of the shearing rates $\dot{\gamma}_{try}^{(\alpha)}$. Similar to the transform residual described by Equation (58), an error residual for the plasticity is calculated,

$$Err_2^{(\alpha)} = \tau_{t+\Delta t}^{(\alpha)} - \chi_{t+\Delta t}^{(\alpha)} - g_{t+\Delta t}^{(\alpha)} \cdot \left|\frac{\dot{\gamma}_{try}^{(\alpha)}}{\dot{\gamma}_0}\right|^{\frac{1}{m}} sign(\dot{\gamma}_{try}^{(\alpha)}) \tag{98}$$

The scaled error norm SSE_2 is now computed using the residuals. When any $\dot{\gamma}_{try}^{(\alpha)}$ is non-zero, the norm is given by

$$SSE_2 = \frac{1}{N_{slip}} \sqrt{\sum_{\alpha=1}^{N_{slip}} \left(\frac{\left|\dot{\gamma}_{try}{}^{(\alpha)}\right|}{\dot{\gamma}_{max}} \cdot Err_2^{(\alpha)} \right)^2} \tag{99}$$

with $\dot{\gamma}_{max}$ defined as

$$\dot{\gamma}_{max} = \max\left(\left|\dot{\gamma}_{try}{}^{(\alpha)}\right|\right), \alpha = 1...N_{slip} \tag{100}$$

If $\dot{\gamma}_{max}$ is determined to be zero, SSE_2 equals zero. Like the transform iterations, it is stored as the reference value for comparison to the norm in future iterations:

$$SSE_{Ref} = SSE_2 \tag{101}$$

In order to determine the next set of shearing rates, the Newton-Raphson loop then calculates the partial derivatives of the residual values defined in Equation (98) with respect to the shearing rates, as given by

$$\frac{\partial \mathrm{Err}_2^{(\alpha)}}{\partial \dot{\gamma}^{(\beta)}} = \frac{\partial \tau^{(\alpha)}}{\partial \dot{\gamma}^{(\beta)}} - \frac{\partial \chi^{(\alpha)}}{\partial \dot{\gamma}^{(\beta)}} - \frac{\partial g^{(\alpha)}}{\partial \dot{\gamma}^{(\beta)}} \cdot \left(\frac{\tau_{t+\Delta t}^{(\alpha)} - \chi_{t+\Delta t}^{(\alpha)}}{g_{t+\Delta t}^{(\alpha)}} \right) - \frac{g_{t+\Delta t}^{(\alpha)}}{m \cdot \dot{\gamma}_0} \cdot \left| \frac{\tau_{t+\Delta t}^{(\alpha)} - \chi_{t+\Delta t}^{(\alpha)}}{g_{t+\Delta t}^{(\alpha)}} \right|^{1-m} \tag{102}$$

To calculate Equation (102), several partial derivatives must first be determined. The derivative of the drag stress with respect to shearing rates is defined based on Equation (14), and is given by

$$\frac{\partial g^{(\alpha)}}{\partial \dot{\gamma}^{(\beta)}} = \frac{\left(H_{dir} - g_{t+\Delta t}^{(\alpha)} \cdot H_{dyn} \right) \cdot \Delta t}{\left(1 + \sum_{\beta=1}^{N_{slip}} H_{dyn} \cdot \left| \dot{\gamma}_{try}^{(\beta)} \right| \cdot \Delta t \right)} \cdot \mathrm{sign}(\dot{\gamma}_{try}^{(\beta)}) \tag{103}$$

The back stress partial derivative is formulated from Equation (15),

$$\frac{\partial \chi^{(\alpha)}}{\partial \dot{\gamma}^{(\beta)}} = \frac{\left(A_{dir} - \chi_{t+\Delta t}^{(\alpha)} \cdot A_{dyn} \cdot \mathrm{sign}\left(\dot{\gamma}_{try}^{(\beta)} \right) \right) \cdot \Delta t}{\left(1 + A_{dyn} \cdot \left| \dot{\gamma}_{try}^{(\beta)} \right| \cdot \Delta t \right)} \cdot \delta_{\alpha\beta} \tag{104}$$

where $\delta_{\alpha\beta}$ is the Kronecker delta. The derivative of the resolved shear stress with respect to the shearing rates is based on Equation (9). As in the transform case with the driving stress, care must be taken to ensure that all terms that are functions of $\dot{\gamma}^{(\beta)}$, including the Cauchy stress, the slip direction, and the slip plane normal. By neglecting higher-order terms, the derivative can be defined as

$$\frac{\partial \tau^{(\alpha)}}{\partial \dot{\gamma}^{(\beta)}} \cong -\left(\underset{\sim}{s}_0^{(\alpha)} \otimes \underset{\sim}{m}_0^{(\alpha)} \right) : \underset{\sim}{C} : \left(\underset{\sim}{s}_0^{(\beta)} \otimes \underset{\sim}{m}_0^{(\beta)} \right) \tag{105}$$

The estimated shearing rate values are then iterated via the Newton-Raphson process, simultaneously solving the Newton equations for each slip system.

$$\mathrm{Err}_2^{(\alpha)} = -\sum_{\beta=1}^{N_{slip}} \frac{\partial \mathrm{Err}_2^{(\alpha)}}{\partial \dot{\gamma}^{(\beta)}} \cdot \Delta\dot{\gamma}^{(\beta)} \tag{106}$$

where $\Delta\dot{\gamma}^{(\beta)}$ is the change in the estimated value of the shearing rate on each slip system. As in the transform Newton iterations, the changes are added to the last estimated value (denoted iteration n), to give the new estimated transform rates (denoted n+1):

$$\left(\dot{\gamma}_{try}^{(\alpha)}\right)_{n+1} = \left(\dot{\gamma}_{try}^{(\alpha)}\right)_{n} + \Delta\dot{\gamma}^{(\alpha)} \tag{107}$$

With the updated values of $\dot{\gamma}_{try}^{(\alpha)}$, Equations (85) through (99) are recomputed. The re-calculated SSE_2 is then compared to SSE_{Ref}. In the event improvement is not achieved, the code reduces the time increment by half, and returns to the top of the algorithm to calculate the new smaller sub-increment, as was done in the event the transform error did not improve. If improvement is attained, then the SSE_2 error norm value is compared to the user-specified tolerance. If tolerance is not achieved, another Newton-Raphson iteration is performed by returning to Equation (85) with the new value of $\dot{\gamma}_{try}^{(\alpha)}$. If convergence has been achieved within tolerance, then the values for $\dot{\gamma}_{try}^{(\alpha)}$ are the accepted values for the current time step,

$$\dot{\gamma}_{t+\Delta t}^{(\alpha)} = \left(\dot{\gamma}_{try}^{(\alpha)}\right)_{n+1} \quad \text{if} \quad \mathrm{SSE}_2 \le \text{tolerance} \tag{108}$$

The shearing rates are then multiplied by the time increment, and used to update the plastic strains and the rate of plastic deformation with respect to stress tensor:

$$\Delta\gamma^{(\alpha)} = \dot{\gamma}_{t+\Delta t}^{(\alpha)} \cdot \Delta t \tag{109}$$

$$\underset{\sim}{E}_{t+\Delta t}^{p} = \underset{\sim}{E}_{t}^{p} + \sum_{\alpha=1}^{N_{slip}} \Delta\gamma^{(\alpha)} \cdot \left(\underset{\sim}{s}_{t+\Delta t}^{(\alpha)} \otimes \underset{\sim}{m}_{t+\Delta t}^{(\alpha)}\right)_{sym} \tag{110}$$

where $\left(\underset{\sim}{s}^{(\alpha)}_{t+\Delta t} \otimes \underset{\sim}{m}^{(\alpha)}_{t+\Delta t}\right)_{sym}$ is given by

$$\left(\underset{\sim}{s}^{(\alpha)}_{t+\Delta t} \otimes \underset{\sim}{m}^{(\alpha)}_{t+\Delta t}\right)_{sym} = \frac{1}{2}\cdot\left[\left(\underset{\sim}{s}^{(\alpha)}_{t+\Delta t} \otimes \underset{\sim}{m}^{(\alpha)}_{t+\Delta t}\right) + \left(\underset{\sim}{m}^{(\alpha)}_{t+\Delta t} \otimes \underset{\sim}{s}^{(\alpha)}_{t+\Delta t}\right)\right] \tag{111}$$

The rate of plastic deformation with respect to the Cauchy stress rate tensor

$$\frac{\partial \underset{\sim}{D}^{p}}{\partial \dot{\underset{\sim}{\sigma}}} = \sum_{\alpha=1}^{N_{slip}} \frac{\partial \underset{\sim}{D}^{p}}{\partial \dot{\gamma}^{(\alpha)}} \cdot \frac{\partial \dot{\gamma}^{(\alpha)}}{\partial \tau^{(\alpha)}} \cdot \frac{\partial \tau^{(\alpha)}}{\partial \underset{\sim}{\sigma}} \cdot \frac{\partial \underset{\sim}{\sigma}}{\partial \dot{\underset{\sim}{\sigma}}} \tag{112}$$

is combined with Equation (75) in calculating the tangent modulus, and where

$$\frac{\partial \underset{\sim}{D}^{p}}{\partial \dot{\gamma}^{(\alpha)}} = \left(\underset{\sim}{s}^{(\alpha)}_{t+\Delta t} \otimes \underset{\sim}{m}^{(\alpha)}_{t+\Delta t}\right)_{sym} \tag{113}$$

$$\frac{\partial \tau^{(\alpha)}}{\partial \underset{\sim}{\sigma}} = \left(\underset{\sim}{s}^{(\alpha)}_{t+\Delta t} \otimes \underset{\sim}{m}^{(\alpha)}_{t+\Delta t}\right)_{sym} \tag{114}$$

$$\frac{\partial \dot{\gamma}^{(\alpha)}}{\partial \tau^{(\alpha)}} = \frac{m \cdot \dot{\gamma}_0}{g^{(\alpha)}_{t+\Delta t}} \cdot \left| \frac{\tau^{(\alpha)}_{t+\Delta t} - \chi^{(\alpha)}_{t+\Delta t}}{g^{(\alpha)}_{t+\Delta t}} \right|^{m-1} \tag{115}$$

The martensitic plasticity portion of the time step is now complete, and the code begins final calculations for outputs and updating of state variables, which are passed on to the next step.

3.3.4.4 Updates for Future Time Steps and Outputs

Following both transform and plastic iterations, the output variables are prepared. When the gcn option is set to greater than one, the stresses, strains, total transform amount, and deformation rate derivatives are calculated for each grain, and then averaged over the number of grains in the element specified in the model. Once averaged, if the user selected more than one grain per element, the variables in Table 7 are sent to the UVARM ABAQUS user output subroutine for visualization of the data [1].

Table 7. User output variables at each integration point in ABAQUS.

$\underset{\sim}{E}^{p}$
$\underset{\sim}{E}^{tr}$
$\underset{\sim}{E}^{el}$
$\underset{\sim}{E}$
$\underset{\sim}{E}^{ie}$
V_{trans}
$\underset{\sim}{\sigma}$

The total inelastic strain, $\underset{\sim}{E}^{ie}$, is given by

$$\underset{\sim}{E}^{ie} = \underset{\sim}{E}^{tr} + \underset{\sim}{E}^{p} \tag{116}$$

After averaging and sending the output variables to the UVARM output subroutine, the state variables and grain orientations for each grain per element are stored for use in the next time step. These include the plastic, transform, and inelastic strains, the average total transform amount over all orientations, the Euler angles for each grain within the element, the plastic deformation gradients, drag stresses, back stresses, transform deformation gradients, critical driving stresses, and individual transform amounts. The state variables are stored in the order mentioned above and listed in Table 8. There is not a limit on the number of grains that can be assigned per element, but the state variable storage increases by 210 entries with each additional grain, so the memory and number of computations per element increases accordingly.

Table 8. State variable storage order for each integration point

$\underset{\sim}{E}^{p}$
$\underset{\sim}{E}^{tr}$
$\underset{\sim}{E}^{ie}$
V_{trans}
φ_{euler}, θ_{euler}, and ψ_{euler} for all grains
$\underset{\sim}{F}^{p}$ for all grains and slip systems
$g^{(\alpha)}$ for all grains and slip systems
$\chi^{(\alpha)}$ for all grains and slip systems
$\underset{\sim}{F}^{tr}$ for all grains and transformation systems
$f_{cr}^{(\lambda)}$ for all grains and transformation systems
$\xi^{(\lambda)}$ for all grains and transformation systems

Note that the state variables which are averaged over grain orientations are stored first, followed by those for which values are kept in all orientations. This is significant because as gcn gets larger, the size of the state variable storage also increases. By placing the averaged variables (for which there is only one entry regardless of gcn) first, the UVARM will choose the correct locations from the state variable array to gather all output data (since they do not change location as the array expands).

The final step of the code is to provide the tangent modulus for the time step, as shown in Figure 44. ABAQUS uses this for determining estimates of the deformation gradients in the next time step. For the discretized time step, the numerator and denominator can by divided by the time step, and hence the tangent modulus can be described by

$$\frac{d\underset{\sim}{\sigma}}{d\underset{\sim}{\varepsilon}} = \frac{d\left(\frac{\Delta\underset{\sim}{\sigma}}{\Delta t}\right)}{d\left(\frac{\Delta\underset{\sim}{E}}{\Delta t}\right)} = \frac{d\dot{\underset{\sim}{\sigma}}}{d\dot{\underset{\sim}{E}}} = \frac{d\dot{\underset{\sim}{\sigma}}}{d\underset{\sim}{D}} \tag{117}$$

where $\underset{\sim}{D}$ is the rate of change of the strain tensor with respect to time. The inverse of the tangent modulus can be formulated as the sum of the derivatives with respect to stress rates of the elastic, plastic, and transform strain rates.

$$\frac{d\underset{\sim}{D}}{d\dot{\underset{\sim}{\sigma}}} = \left(\frac{\partial\underset{\sim}{D}^{e}}{\partial\dot{\underset{\sim}{\sigma}}} + \frac{\partial\underset{\sim}{D}^{p}}{\partial\dot{\underset{\sim}{\sigma}}} + \frac{\partial\underset{\sim}{D}^{tr}}{\partial\dot{\underset{\sim}{\sigma}}} \right) \tag{118}$$

By combining Equations (117) and (118), and noting the following relation

$$\frac{\partial\underset{\sim}{D}^{e}}{\partial\dot{\underset{\sim}{\sigma}}} = \frac{\partial\underset{\sim}{E}^{e}}{\partial\underset{\sim}{\sigma}} = \underset{\sim}{C}^{-1} \tag{119}$$

the tangent modulus is constructed according to

$$\frac{d\underset{\sim}{\sigma}}{d\underset{\sim}{\varepsilon}} = \left(\underset{\sim}{C}^{-1} + \frac{\partial\underset{\sim}{D}^{p}}{\partial\dot{\underset{\sim}{\sigma}}} + \frac{\partial\underset{\sim}{D}^{tr}}{\partial\dot{\underset{\sim}{\sigma}}} \right)^{-1} \tag{120}$$

where all of the terms are as computed earlier in the code. All calculations in the material routine UMAT are now complete, and the subroutine exits and returns to ABAQUS.

3.3.5 Experimental Calibrations of Material Model

In order to implement the two-phase material model, it is necessary to determine all of the input parameters in Table 5. Some parameters can be chosen from published values in literature, while others require calibration to experimental data. Experimental

calibration requires both physical tests and a virtual test model with which to compare response curves.

3.3.5.1 Virtual Test Models

The micro-plasticity material model provides a localized response based on crystallographic orientation(s) of a given element. For comparison to experimental data of a homogeneous physical specimen, an averaged response of many grains is necessary. To facilitate this, a finite element model was constructed with 125 regions of 2 x 2 x 2 elements, each region being assigned a random set of Euler angles. Figure 47 illustrates the model's random orientation treatment, viewed from any orthogonal direction.

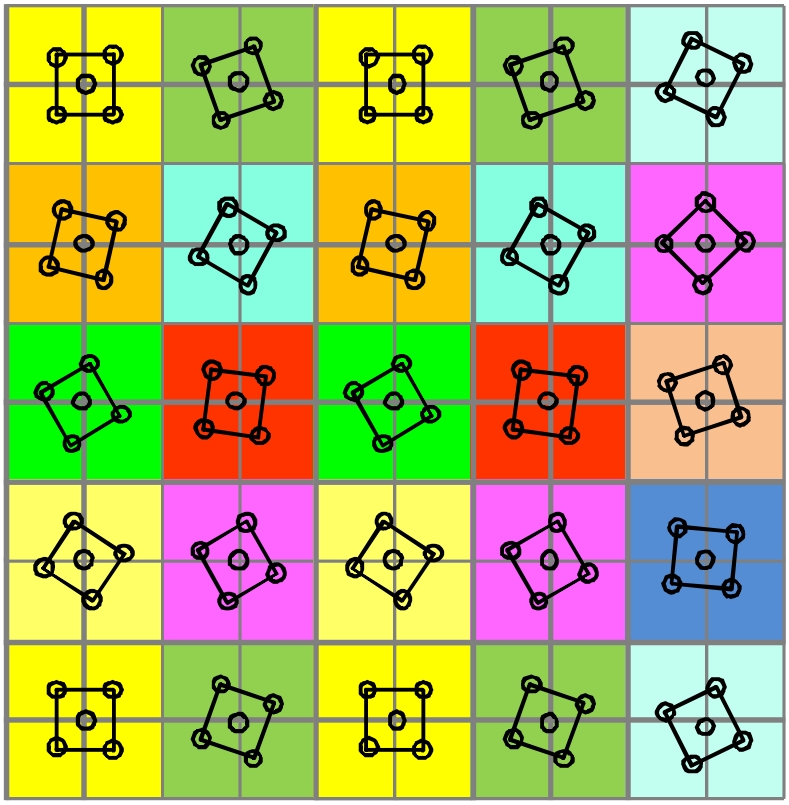

Figure 47. Orientation scheme for virtual test model.

Due to the non-uniform response of the different orientations, a simple prescribed-displacement boundary condition of faces will lead to artificial responses along those surfaces. To allow for localized deformations and measure the overall response of the grains collectively, periodic boundary conditions are applied to the model, as described by Zhang [59]. This entails creating a reference node in the model, which is linked to surface nodes on the desired surface via constraint equations, as depicted in Figure 48.

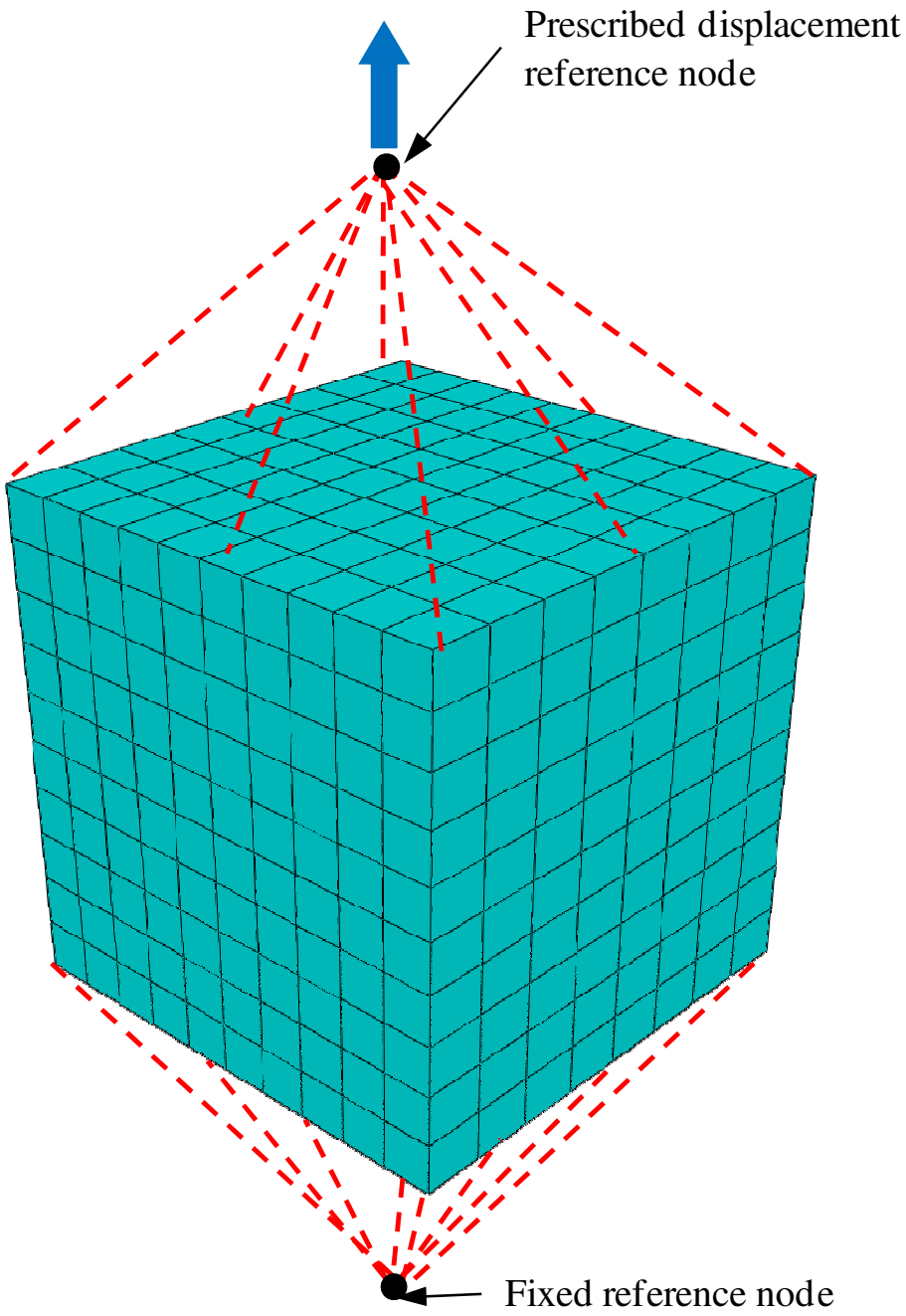

Figure 48. Periodic boundary condition scheme.

Rather than requiring all nodes to displace a prescribed amount on the surface, the collective movement of all tied nodes must resolve with the displacement of the reference node. The virtual uniaxial test is conducted by prescribing the displacement of the

reference node, and recording its reaction force. This is then translated into stress-strain data for the model using the dimensions of the cube. Reaction force is divided by the area of the face to return average uniaxial stress, and displacement of the reference node is divided by the cube side length to yield the axial strain in the model. Similarly, transverse strain is measured by taking the averaged displacements of lateral faces relative to one another, and dividing by cube side length. The incremental displacement of the reference node replicates a displacement-controlled experimental uniaxial test.

The resulting virtual model provides unique local strains, while delivering a response that is homogenized by the high number of orientations prescribed. A typical response under tensile loading is shown in Figure 49. Note the inhomogeneities in neighboring regions with different crystallographic orientations. Conventional J_2 plasticity would just predict a uniform strain field under tensile loading. The constraints resulting from the intergranular interactions lead to a highly heterogeneous stress and strain field.

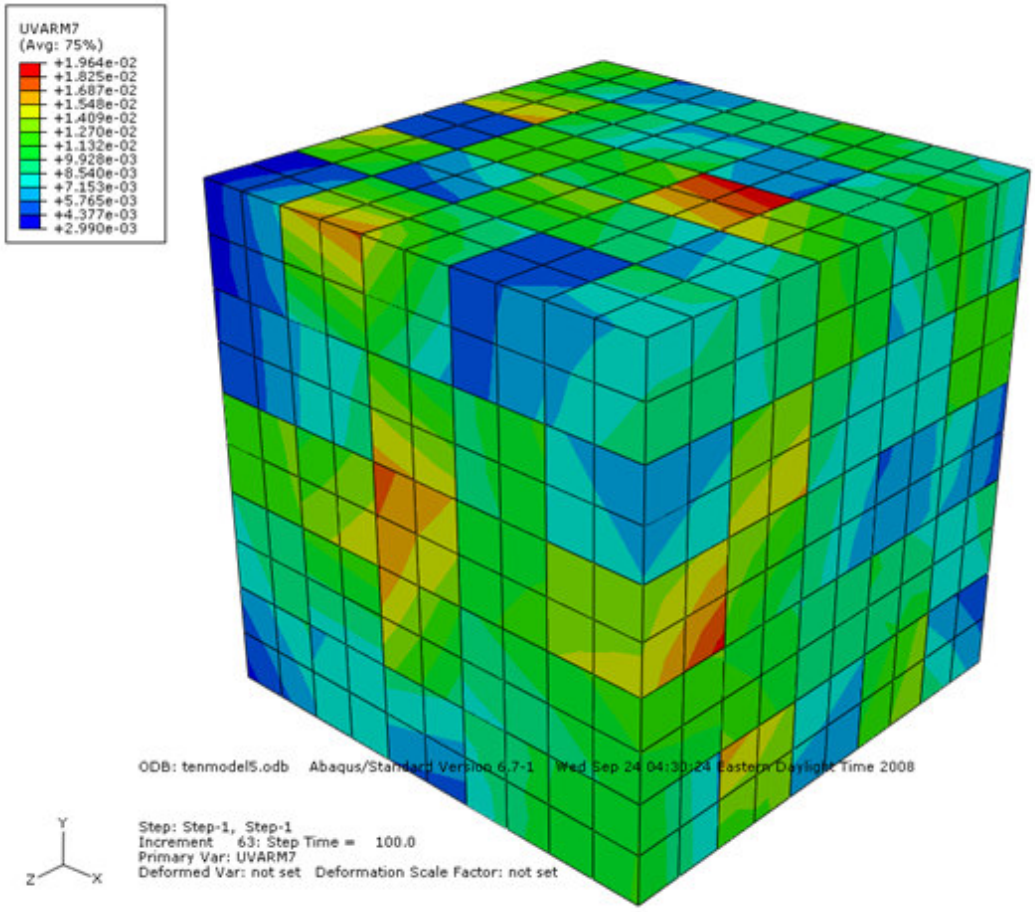

Figure 49. Effective total strain distribution at 1% total strain in a sample containing 35% initial RA during virtual tensile test.

For two-phase models, in addition to tracking all strains (total, elastic, plastic, and transform), the volume fraction evolution will be updated for all elements as loading causes transformations. Individual regions and elements will experience differing volume fraction evolutions locally, and as a whole the average amount transformed will be calculated for the virtual specimen. An example of a virtual tensile loading showing the volume fraction transformed austenite is given in Figure 50.

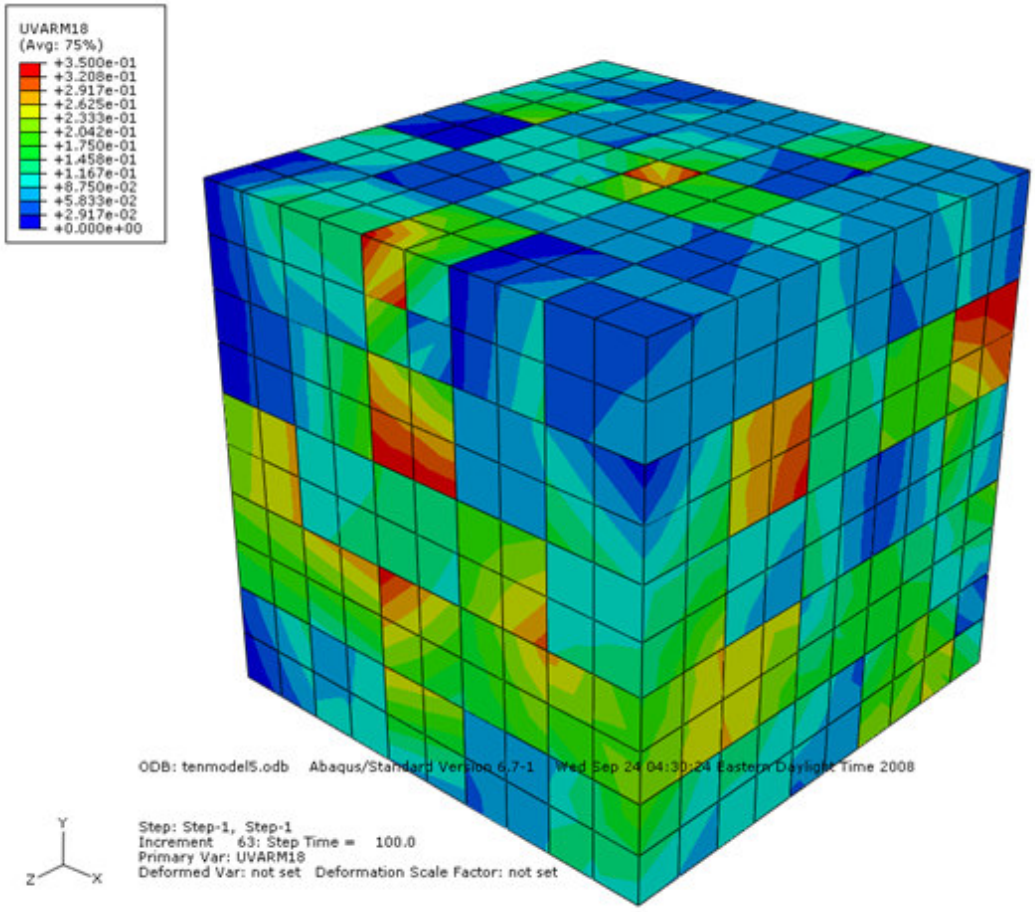

Figure 50. Volume fraction transformation at 1% total strain in a sample containing 35% initial RA during virtual tensile test.

Tensile and compressive physical tests are used for adjustment of parameters via virtual tensile and compressive testing with the periodic boundary virtual test model. In addition to these calibrations, it is of interest to observe the shearing behavior of the material models developed through a virtual simple shear test model. Physical shearing tests are difficult to perform, and thus these tests will not be for comparison to experimental data, but rather to ensure the developed models' behaviors are reasonable. They can be compared with conventional macro-plastic models such as the J_2 plasticity model, for reference. The simple shear model contains a set of 125 randomly oriented

elements, with constraints to simulate a simple shear case. The bottom of the cube will be constrained in all DOF's, while the top surface is fixed vertically (y-direction), and prescribed horizontal displacement (x-direction) in a manner similar to the tensile virtual test specimen via a tied reference node, as depicted in Figure 51. The z-normal faces are fixed in the z-direction. These boundary conditions create a simulation of simple shear behavior for the model.

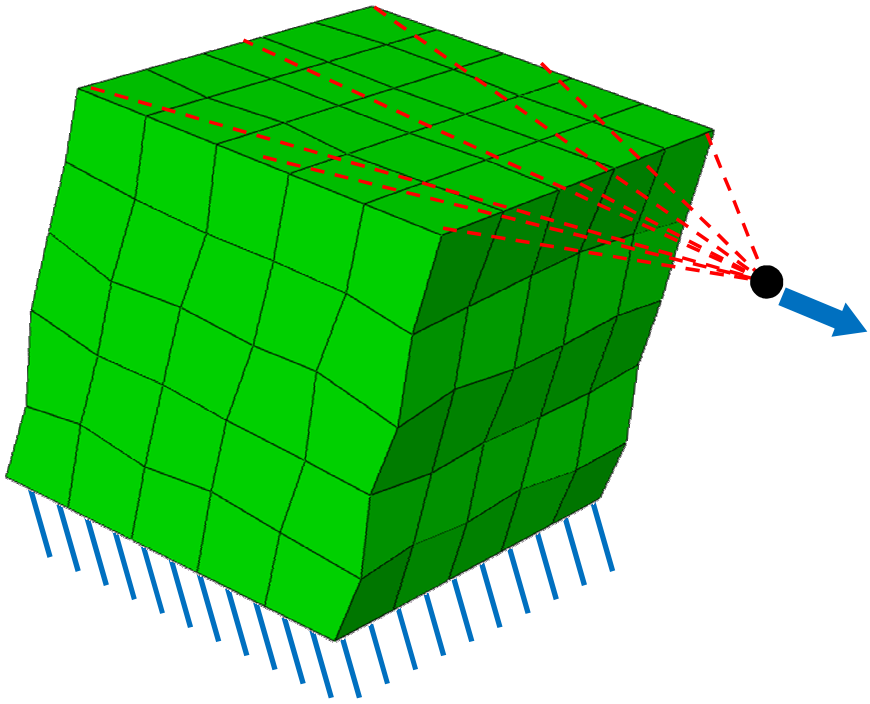

Figure 51. Virtual shear test model setup.

Like the tensile model, local responses will vary, with the aggregate behavior of the model being captured by the reference node's reaction loading to the specified displacements. An example of effective inelastic strain distribution during virtual shear model testing is shown in Figure 52.

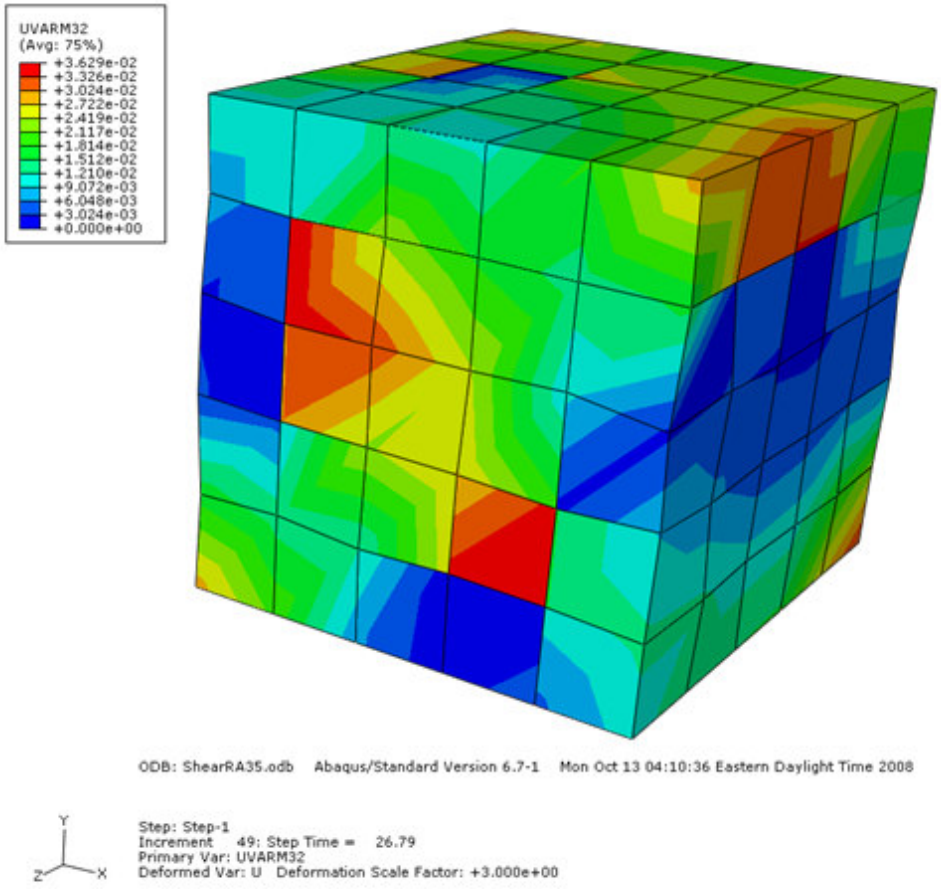

Figure 52. Effective inelastic strain distribution at 2.5% simple shear strain in a sample containing 35% initial RA during virtual shear test.

Volume fraction evolution is also tracked by the material model when enabled for two-phase behavior, and an example volume fraction evolution is shown in Figure 53. As with the tensile test model, localized transformations vary greatly depending on favorable orientation of the individual elements, and averaged volume fraction transformed can be tracked.

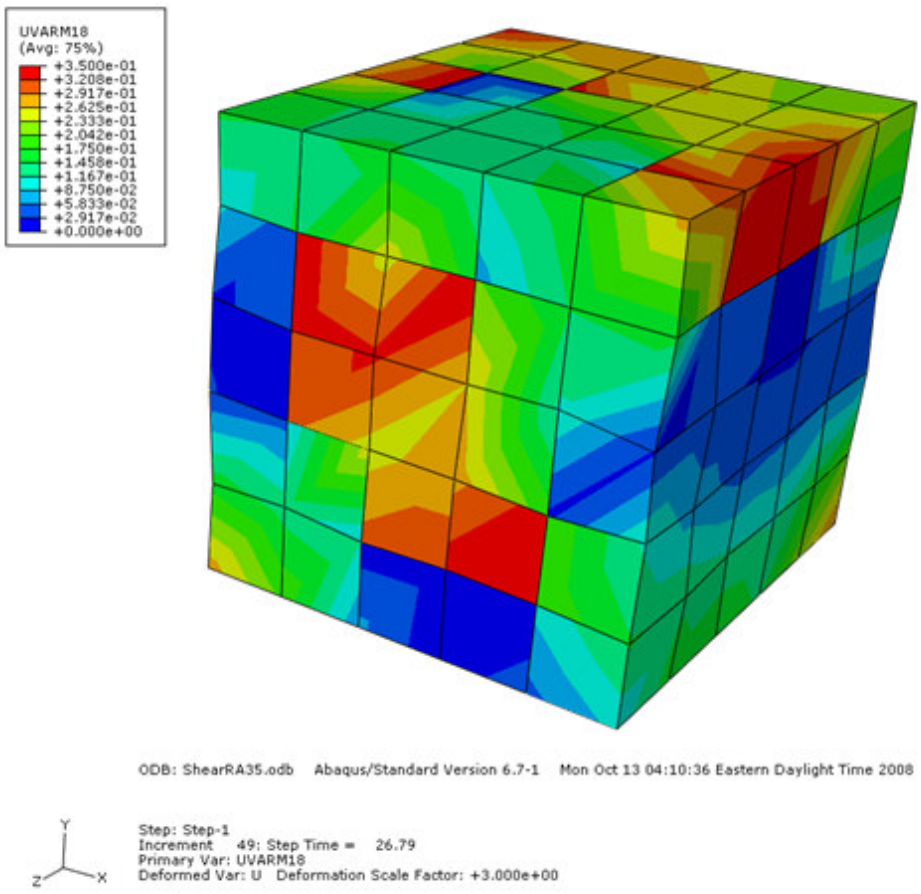

Figure 53. Volume fraction evolution at 2.5% simple shear strain in a sample containing 35% initial RA during virtual shear test.

3.3.5.2 Matching the Model to Test Data

The two-phase model requires constants to be fitted for both the crystal plasticity and transformation, which can be occurring simultaneously. Thus, the calibration process was performed in two steps.

Initially, the 4145 experimental data was matched with the model in single-phase mode ($RA_{initial}$ set to zero). Since the 4145 steel is highly martensitic, there are negligible transform effects and it can be used to calibrate the fully martensitic crystal plasticity

model. The experiments were conducted at room temperature and a strain rate of 10^{-4} s^{-1}, using a round dogbone specimen. A load cell captured force data, while diametrical and axial extensometers measured displacements. Using the ABAQUS UMAT routine, with martensite only, virtual tests in displacement-control were conducted to match the experimental curve as closely as possible. This involves taking initial guess values from parameters of similar steels, and using some trial-and-error to gauge the effect of varying each parameter on the curve's appearance. The calibrated model data is plotted versus experimental data in Figure 54.

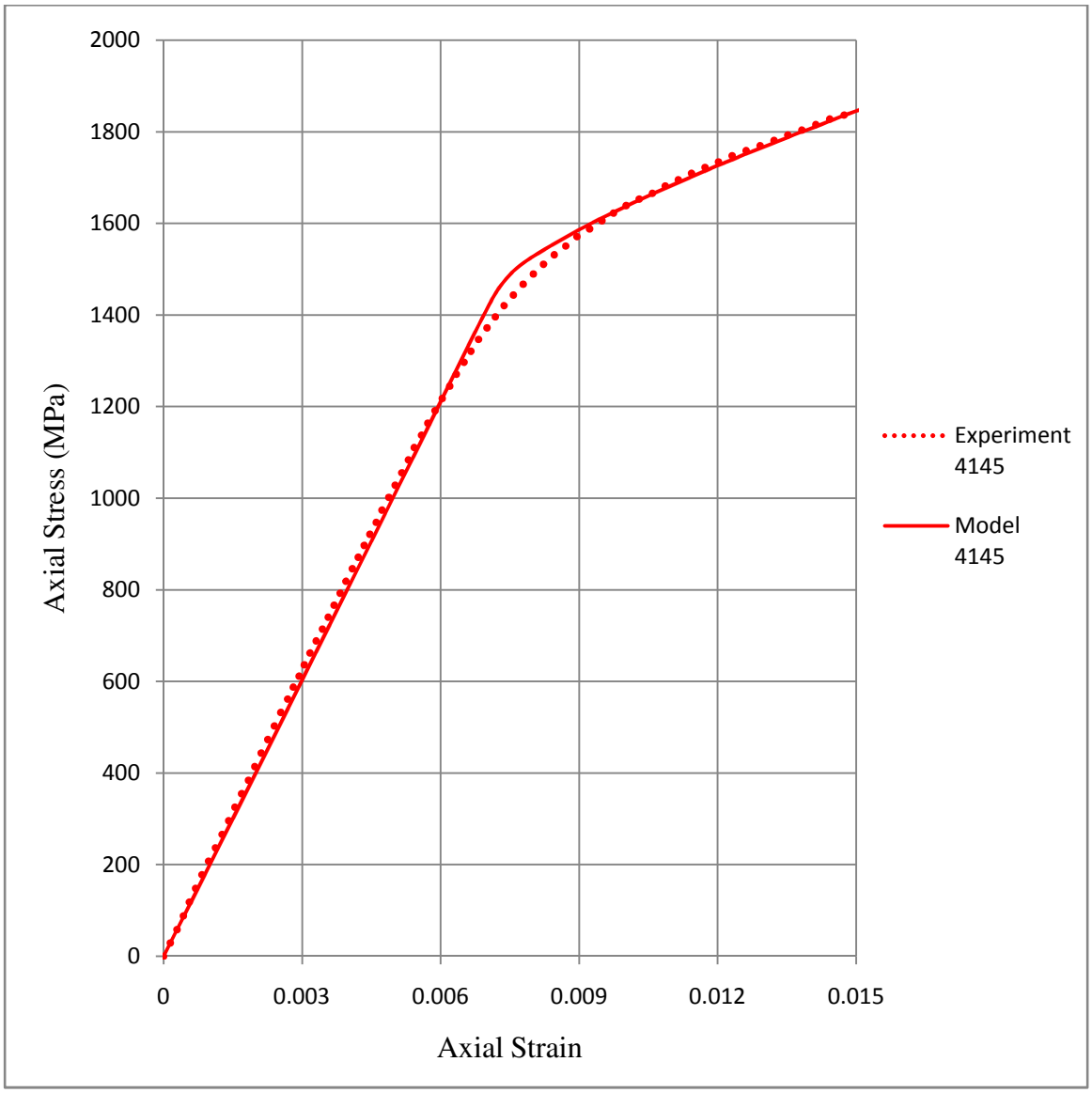

Figure 54. Calibration of 4145 steel.

After adjustment of the input parameters, the UMAT material model and virtual test model produce a response stress-strain curve that is very similar to the experimental data gathered. The numerical values of the parameters for the model can be found in Section 3.3.5.3 Calibrated Material Parameters, Table 9. A process of trial-and-error to make adjustments to the initial drag stress, $g_0^{(\alpha)}$, and direct isotropic hardening parameter,

H_{dir}, was employed in order to match visually with the experimental data. The calibrated martensite parameters of the code are then assumed to represent the behavior of the martensite phase in the two-phase material model.

The two-phase model including the austenite-martensite transform parameters are calibrated using the experimental response of three 41100 steels containing different amounts of retained austenite (35%, 22%, and 13% initial retained austenite). The parameters for the martensitic phase are held constant. Experimental tests were conducted in the same manner as the 4145 tests, with a strain rate of 10^{-4} s^{-1}, using round dogbone specimens. Comparison of the calibrated virtual tensile tests and experimental tests for each of the three 41100 cases is shown in Figure 55.

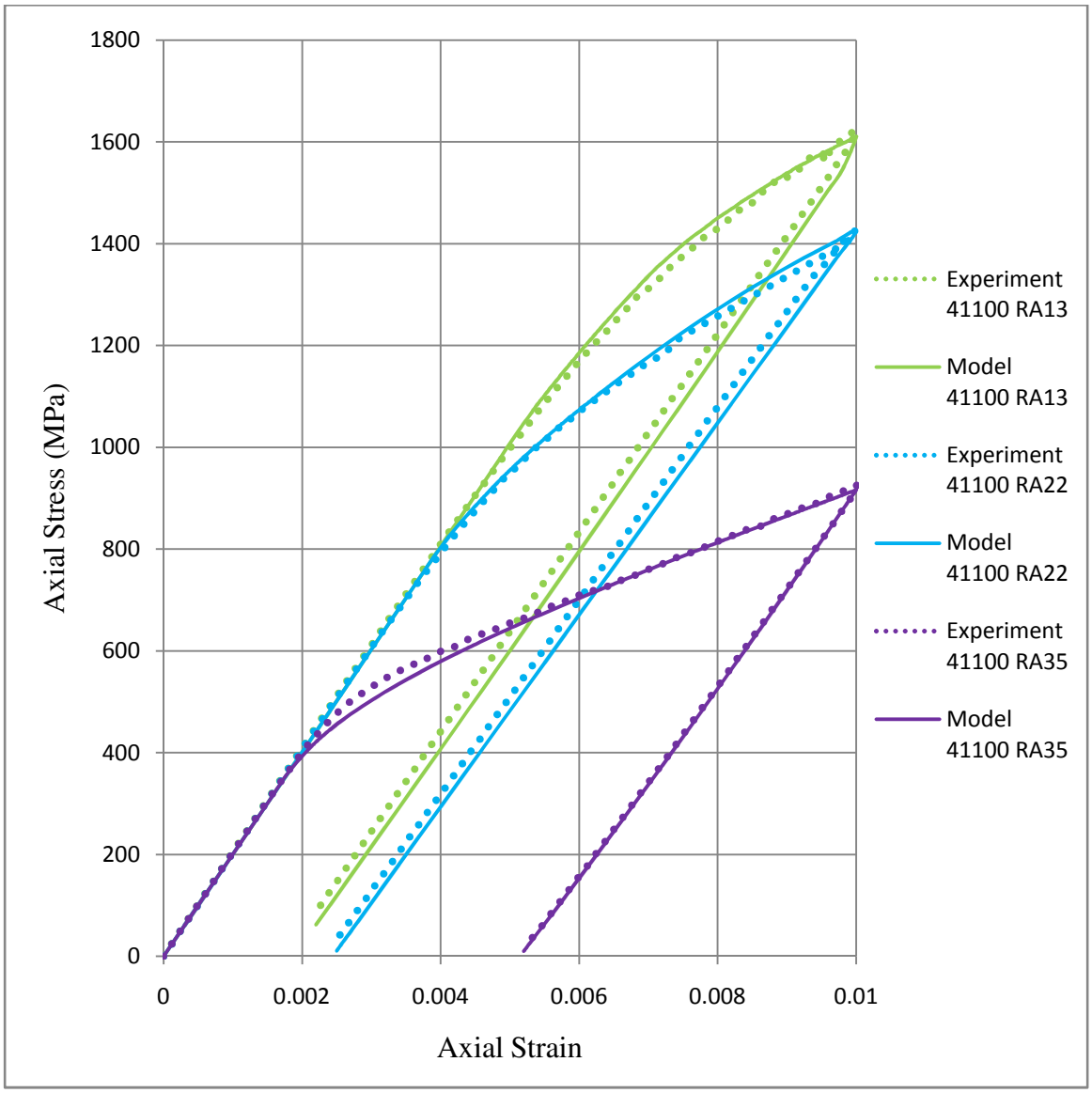

Figure 55. Two-phase crystal plasticity model calibration to 41100 steel containing different amounts of retained austenite.

The calibrated two-phase model matches well with the experimental data in the tensile test regime. Different values of the initial critical driving stress, $\left(f_{cr}^{(\lambda)}\right)_0$, and transform hardening coefficient, Q, are required for the different 41100 microstructures, while all other parameters are uniform over each initial volume fraction. In addition to

the stress-strain data, volumetric transform strain was compared for validation, and is displayed in Figure 56.

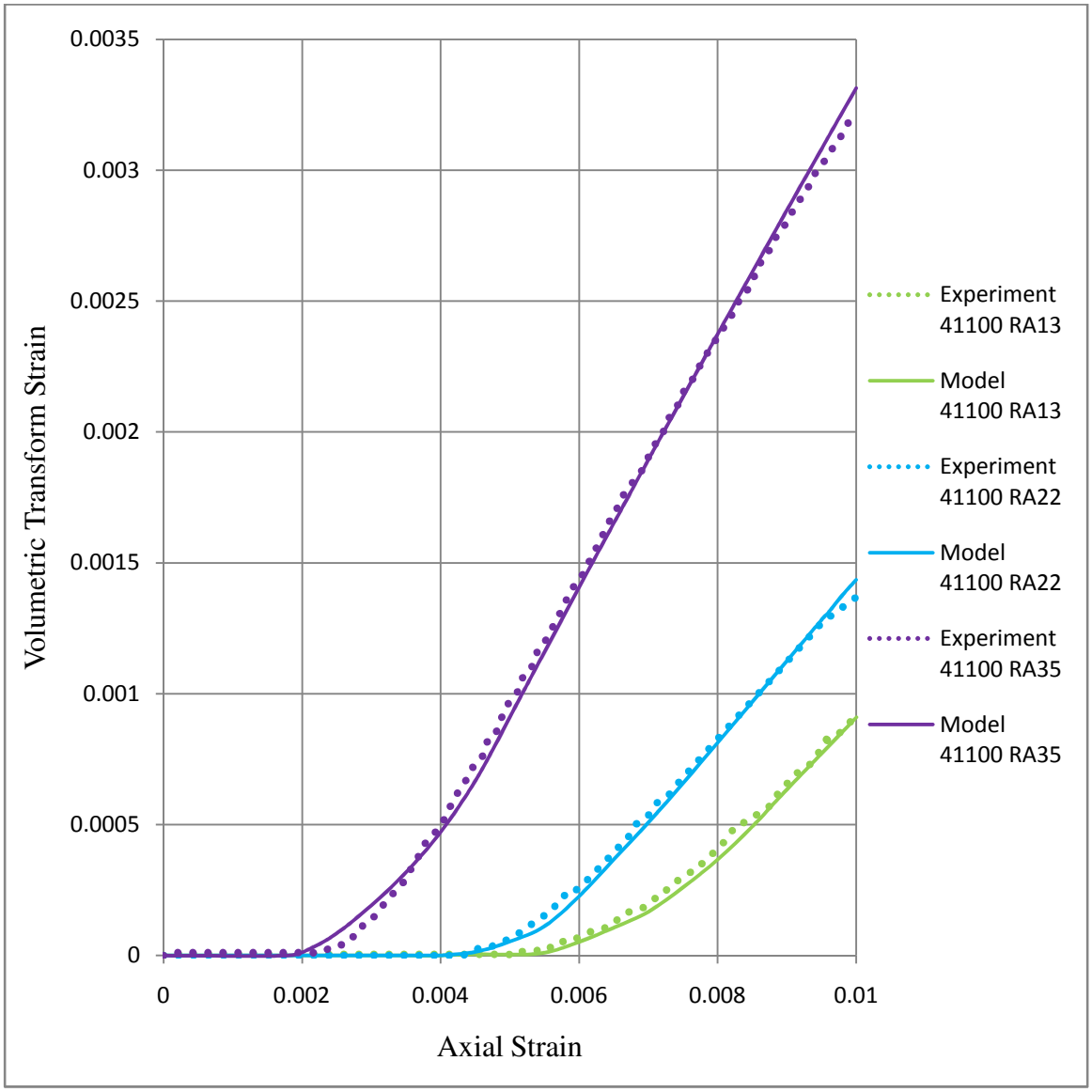

Figure 56. Volumetric transform strain comparison for 41100 steel.

The experimental values for volumetric transform strain were calculated based on the diametral and axial extensometer readings, subtracting the expected elastic strains. Virtual test data was collected by simply summing the normal transform strain

components. The data here also matches well with the experiments, further solidifying the reliability of the model.

Although it cannot be measured during the physical tests, the averaged volume fraction transform amount is of interest for comparison between initial volume fractions, and is plotted in Figure 57. For a model with homogenized response, it is expected that the averaging of the transform amounts of several grains should yield a curve similar in shape to the volumetric transform strain plots from Figure 56. As can be seen, the curves are of similar shape and trend. This is important to note because it strengthens the assumption that the virtual test specimen is sufficiently homogenized.

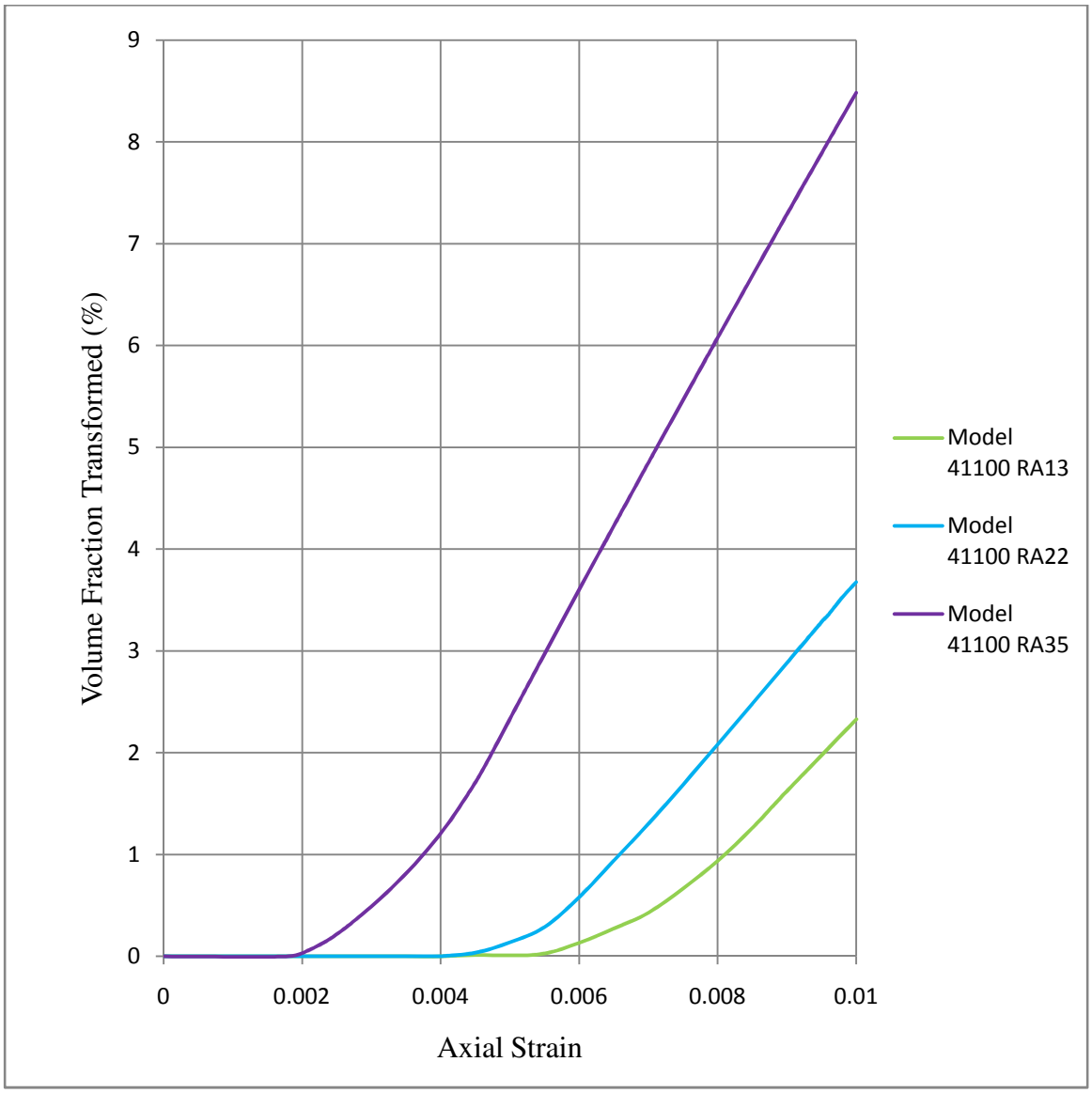

Figure 57. Volume fraction transform amounts of the virtual test models.

Compression testing was also performed to further compare experimental and virtual test behaviors. Although all parameters were calibrated via the tensile tests, the compression tests provide further validation of the model. The physical compression tests were run at the same rates as the tensile tests, and the virtual models used all the same parameters and setup, while simply reversing the displacement direction of the

reference node. Figure 58 gives a comparison of physical and virtual test data for the compression testing. The model delivers a response which accurately reflects the compressive behavior observed, as well as the tensile shown previously.

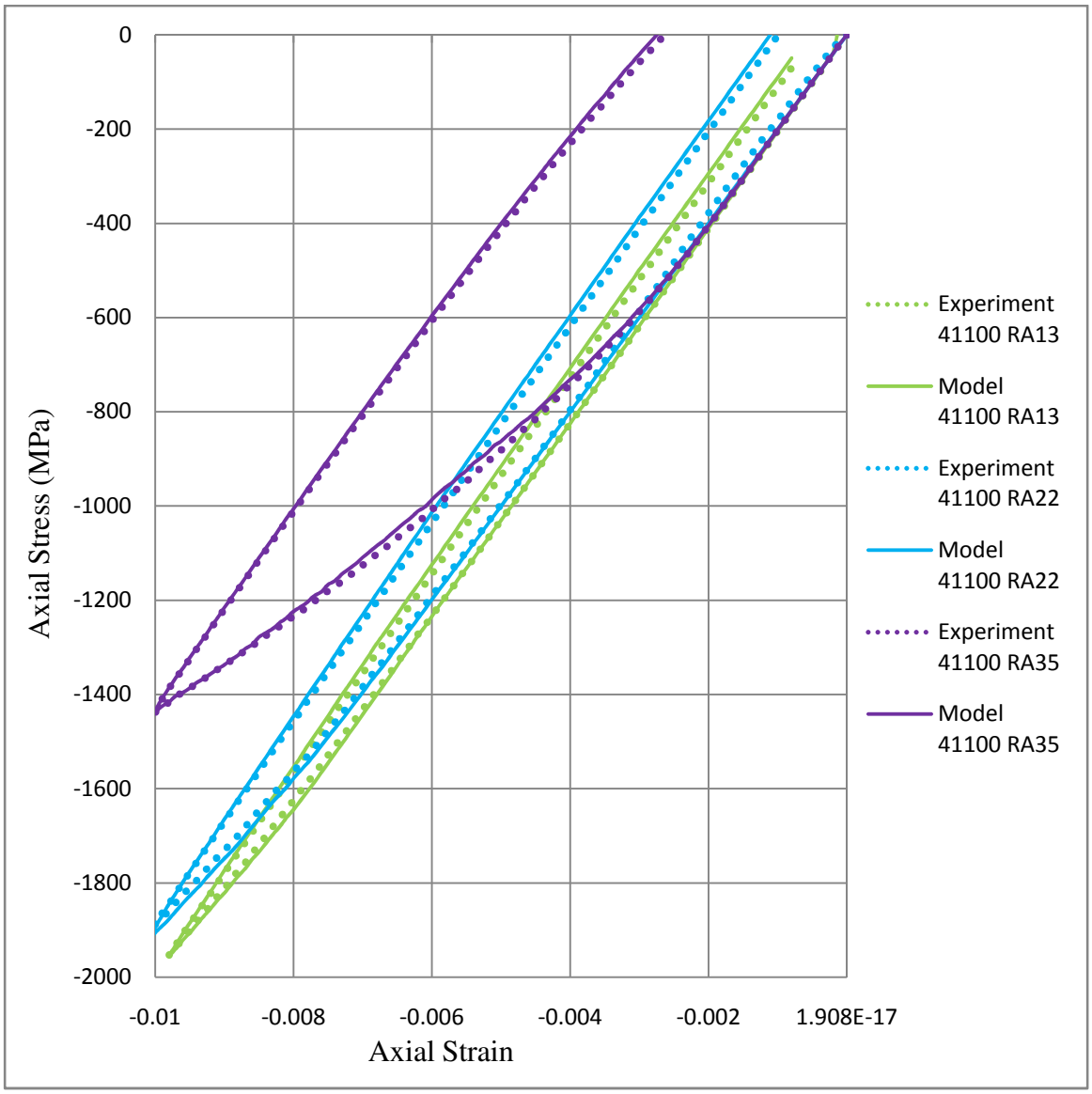

Figure 58. Compression response of 41100 steel with different amounts of retained austenite.

It should be noted that much less transform occurs in compression than in tension. This is due to the fact that many of the favorable loading situations for the transformation

driving stress are found in tensile states. This is clearly shown by the significantly smaller amounts of inelastic strain in the compression stress-strain plots than in the tensile ones.

In addition to the tension and compression comparison tests, a simple shear test was conducted on the virtual shear test model. Difficulties in performing shear tests preclude the production of physical comparison data here, but it is of interest to observe the behavior of the calibrated material model in a simple shearing state (Figure 59). During the virtual shear tests, the reference node reaction force is divided by the cross-section area to give the nominal shear stress, and the reference node prescribed lateral displacement divided by cube side length gives the nominal engineering shear strain.

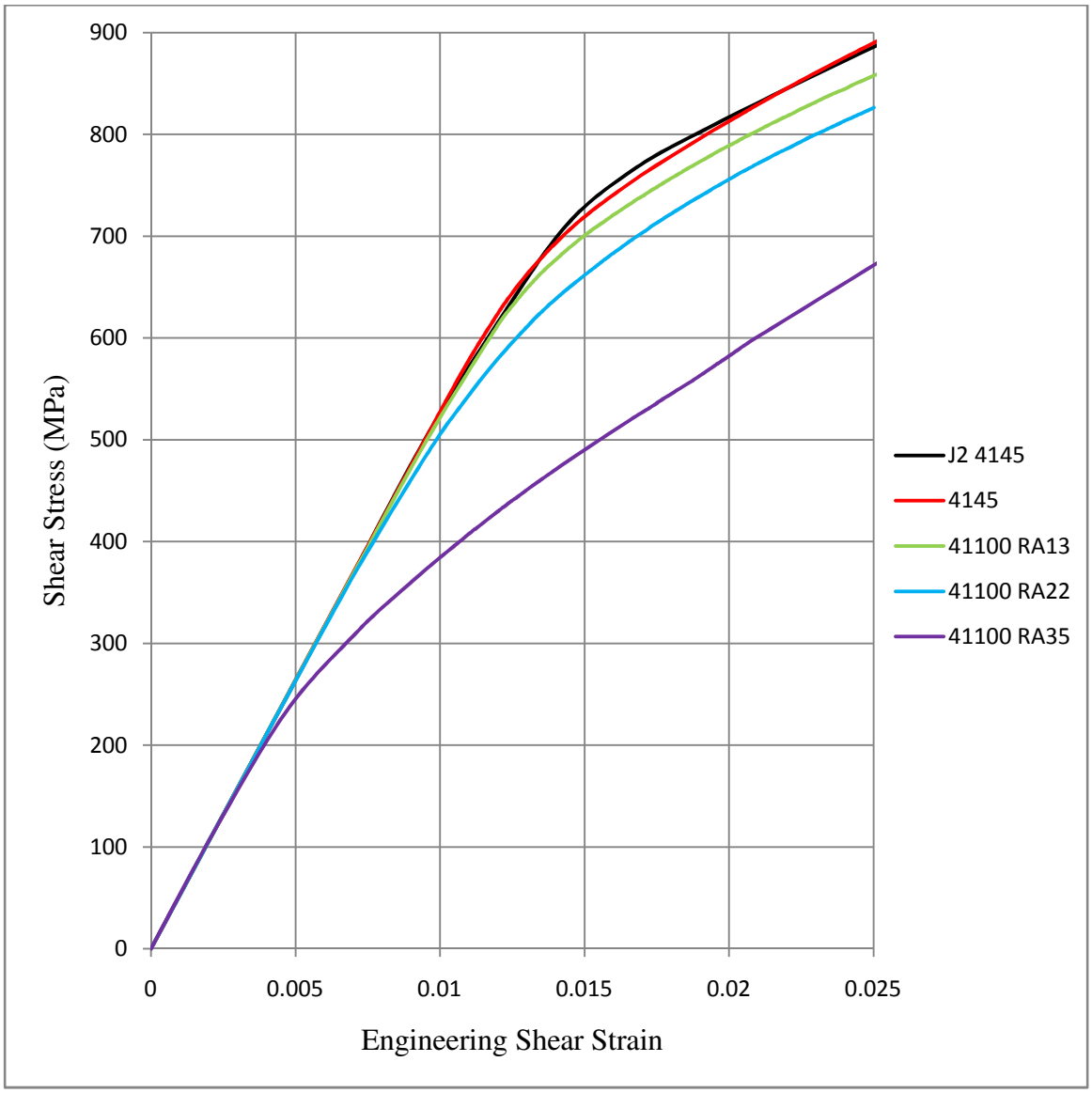

Figure 59. Simple shear test of the virtual models.

In addition to the two-phase and fully martensite crystal/transform plasticity models, a simple shearing test with J_2 macro-plasticity material formulation (built-in ABAQUS material model [1]) was performed for comparison purposes. The 4145 crystal plasticity model matches well with its J_2 counterpart. This indicates a good random

distribution in the virtual shear test model, as the advanced material provides an aggregate response similar to that of the homogenous J_2 model.

3.3.5.3 Calibrated Material Parameters

Shown in Table 9 are the parameters which were used to generate the virtual test plots shown in the previous section, with applicable units, if any, noted.

Table 9. Calibrated material model parameters.

Parameter	**4145**	**41100 RA13**	**41100 RA22**	**41100 RA35**
C_{11}^0	269230 MPa			
C_{12}^0	115384 MPa			
C_{44}^0	76923 MPa			
$\dot{\gamma}_0$	0.001 s^{-1}			
m	50			
$g_0^{(\alpha)}$	770 MPa			
H_{dir}	8500 MPa			
H_{dyn}	0			
$\chi_0^{(\alpha)}$	0 MPa			
A_{dir}	0 MPa			
A_{dyn}	0			
$RA_{initial}$	0	0.13	0.22	0.35
γ_T	N/A	0.1809		
ν_{tr}	N/A	0.17		
$\dot{\xi}_{max}$	N/A	0.003 s^{-1}		
$\left(f_{cr}^{(\lambda)}\right)_0$	N/A	120 MPa	87.4 MPa	40 MPa
Q	N/A	650 MPa	450 MPa	150 MPa

It is of interest to examine the trends in variation of $\left(f_{cr}^{(\lambda)}\right)_0$ and Q with respect to their associated initial volume fractions of austenite. Drawing a relationship between these three cases will enable interpolation of the material model to investigate desired

initial volume fractions between the gathered data points. Shown in Figure 60 is a plot of the critical driving stress, $\left(f_{cr}^{(\lambda)}\right)_0$, versus initial volume fraction.

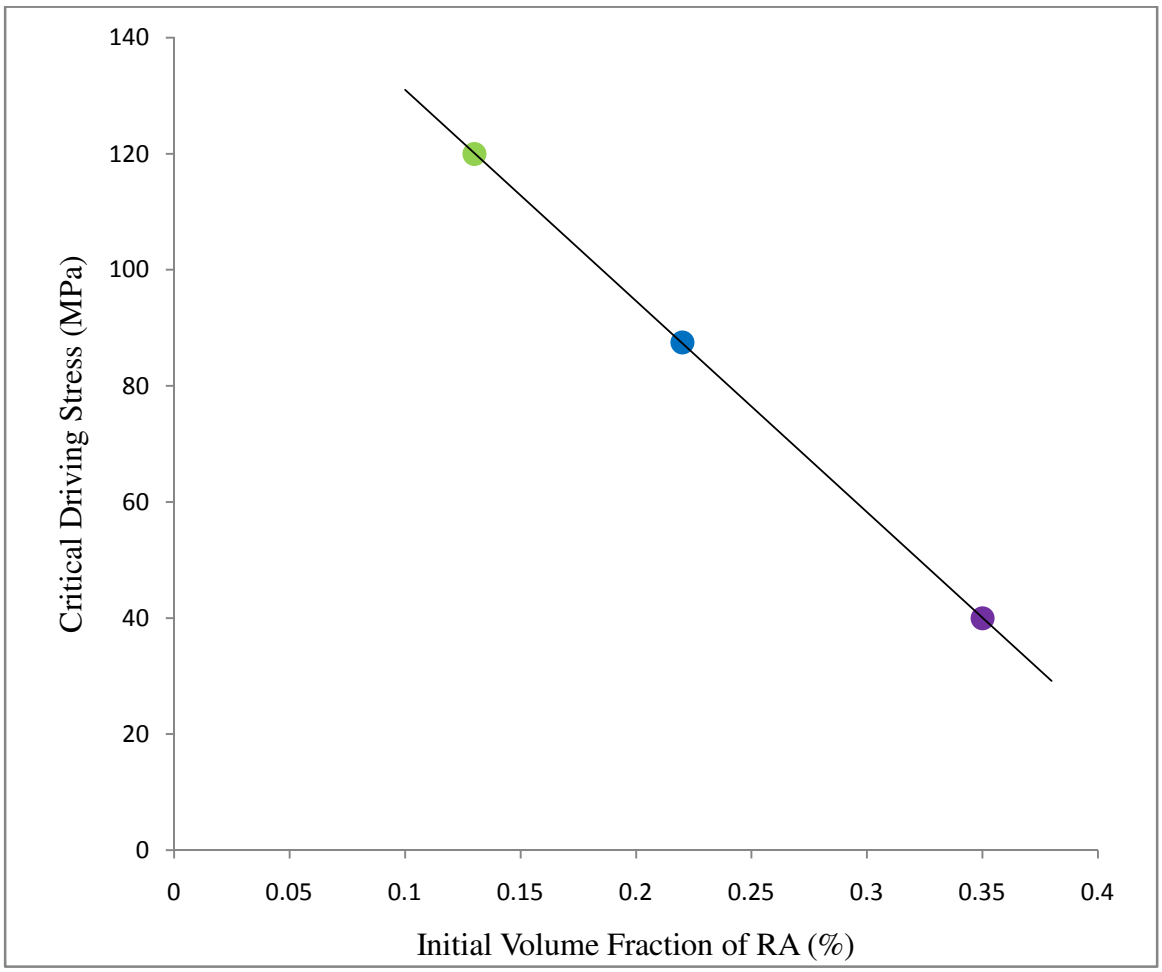

Figure 60. Critical driving stress - initial volume fraction relationship.

The trend indicated by these data points is clearly linear in nature. Thus, if a simulation were desired to be run with an initial volume fraction lying in between the calibrated data sets, a linear interpolation may be assumed. The formulation for initial critical driving stress, $\left(f_{cr}^{(\lambda)}\right)_0$, as a function of initial volume fraction of retained austenite, $RA_{initial}$, is

$$\left(f_{cr}^{(\lambda)}\right)_0 = \left(167.38 - 363.76 \cdot RA_{initial}\right) MPa \quad (121)$$

Similarly, the trend between transform hardening coefficient, Q, and initial volume fraction was also investigated, and is depicted in Figure 61.

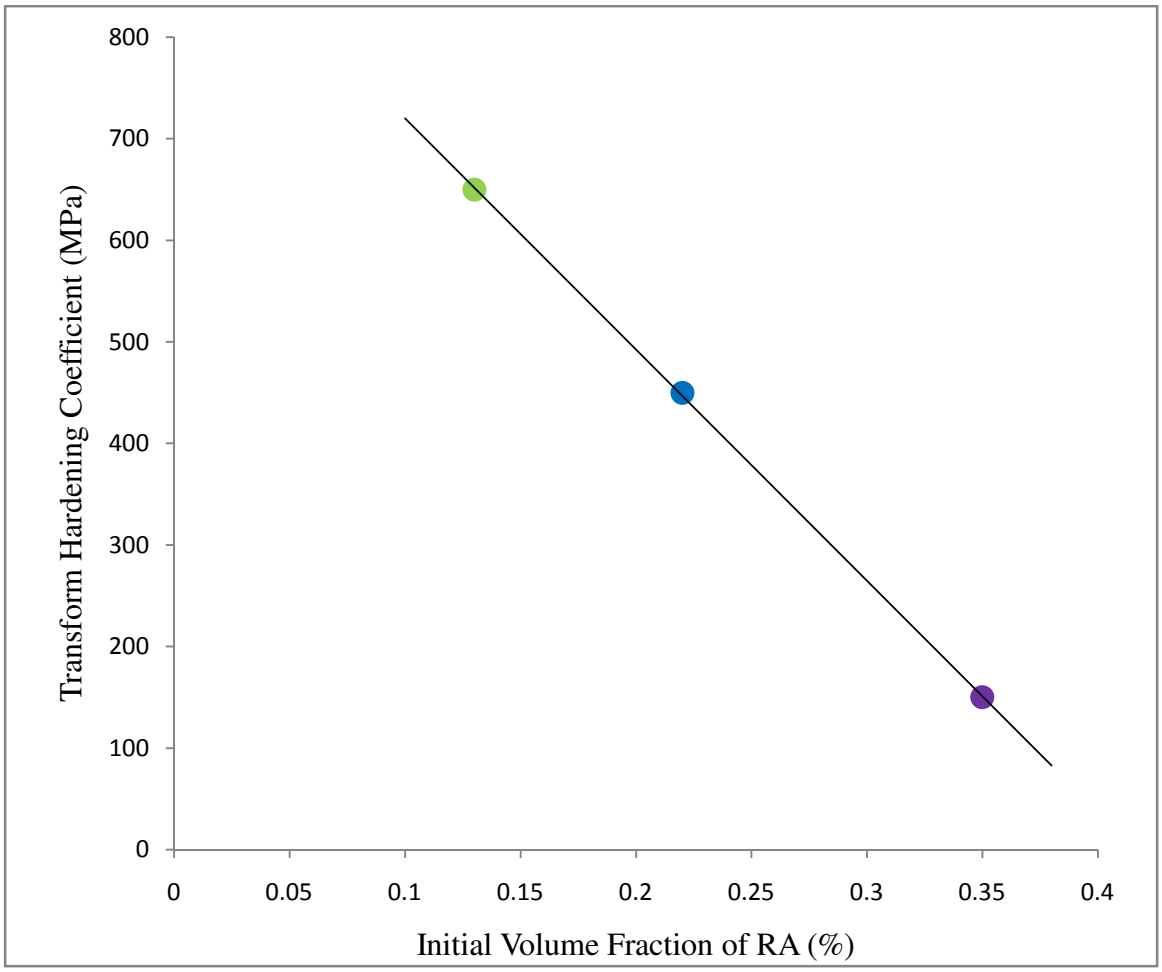

Figure 61. Transform hardening coefficient - initial volume fraction relationship.

This parameter also demonstrated a linear relation with respect to initial volume fraction. The formulation for transform hardening coefficient, Q, as a function of initial volume fraction of retained austenite, $RA_{initial}$, is

$$Q = \left(947.55 - 2275.2 \cdot RA_{initial}\right) MPa \quad (122)$$

CHAPTER 4: DEMONSTRATION CASES

The tools developed in this work are useful in examining a number of rolling contact fatigue scenarios, including relating microstructural parameters to fatigue indicators. The new method is novel in both its 3-D geometric finite element model, and the two-phase material model with transformation. Presented here are two demonstration cases that emphasize the new utility of both parts of this method over previous models. The first, a study of the effect of inclusion orientation on relative fatigue performance, highlights the utility of the 3-D geometric modeling tools. The second, an investigation of initial retained austenite volume fraction's influence on relative fatigue performance, showcases the versatility of the two-phase hybrid material model. These cases are but two of the many useful prospective investigations made possible by the novelty of this project.

4.1 Inclusion Orientation Effects Study

One of the key factors in subsurface spall formation is the orientation of inclusions present in the base metal matrix. For this demonstration, a J_2 plasticity model with isotropic hardening representing 4145 martensitic steel is used. The aluminum oxide (Al_2O_3) inclusions are given a rectangular shape, with dimensions 10 x 10 x 50 μm. The properties for the base metal and inclusion are as listed in Table 2. Hardening follows the 4145 response curve, with interpolation points given in Table 3. The interface between the inclusion and matrix is set to be perfectly bonded. Of particular interest in bearing design are inclusions oriented in the y-z plane, with the long axis of

the inclusion lying in this plane (known as “out-of-plane”), as shown in Figure 62. These have been favored orientations of inclusions for propensity of fatigue crack nucleation, as observed in historical data tracking historical failures of bearing components [11].

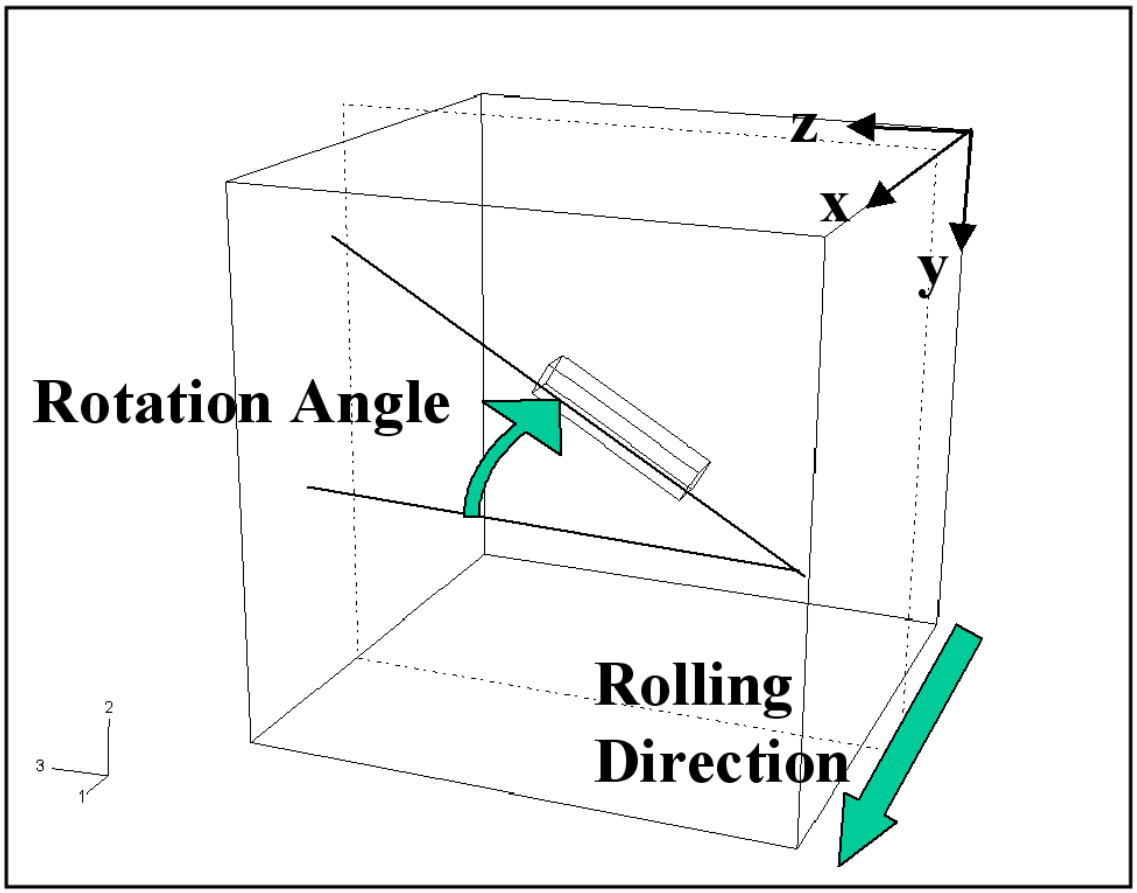

Figure 62. Out-of-plane inclusion orientation for the orientation effect study.

As previously shown in Figure 3, x is the rolling direction, y is the depth direction, and z is the cylindrical roller axis direction. A two-dimensional model in the x-y plane cannot account for such inclusion orientations, and thus is a unique feature to a three-dimensional model such as the one presented here.

The applied Hertzian loading is based on a maximum contact pressure of 2.68 GPa, correlating to a contact half-width of 344 μm, based on a radius of 12.83 mm and a

bearing load of 1448 kN. The cyclically applied bearing stresses are calculated at the depth of maximum Tresca stress, occurring at 267 μm. Nine load steps per pass were conducted, as shown in Figure 23, and three full passes were made with the simulation. The small-scale volume element model was used, with an elastic inclusion and elasto-plastic matrix zone and tetrahedral elements, as depicted in Figure 22. The dimensions and mesh densities for the model are given in Table 10. Note that mesh density increases near the inclusion, where plastic strain accumulation is largest. Tetrahedral elements (ABAQUS code C3D4) were used for meshing [1].

Table 10. Dimensions of zones and mesh for inclusion orientation study.

Zone	**Outer Dimensions**
Inclusion	50 x 10 x 10 μm
Base Metal Matrix	150 x 150 x 150 μm
Mesh Region	**Nominal Mesh Element Size**
Inclusion	1.25 μm
Matrix Inner Boundary	1.25 μm
Matrix Outer Edges	15 μm

Simulations were conducted for different inclusion orientations in 15-degree increments from zero to ninety degrees for the angle depicted in Figure 62. This was accomplished via the aforementioned UTRACLOAD routine which rotates the applied rolling contact loads to the desired orientation, thus eliminating the need for re-meshing. The routine utilizes a tensor rotation scheme as given by Equation (34) to apply the appropriate traction boundary conditions for the desired rotation angle.

The total three-pass equivalent plastic strain accumulation for rotation angles of 15, 30, 45, 60, 75, and 90 degrees is shown in Figure 63, from left to right and top to bottom, respectively.

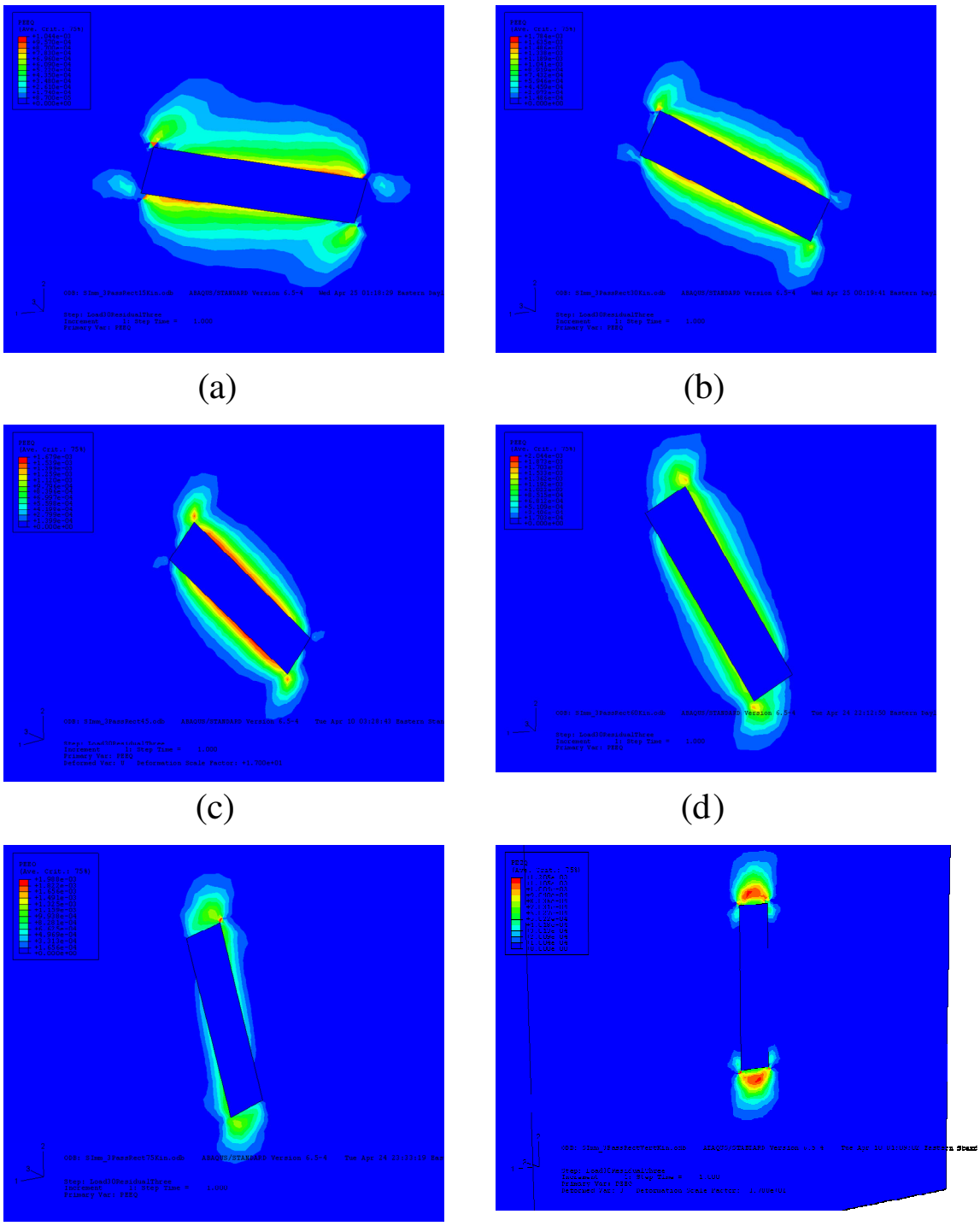

Figure 63. Equivalent plastic strain accumulation over three passes for (a) 15 degrees, (b) 30 degrees, (c) 45 degrees, (d) 60 degrees, (e) 75 degrees, and (f) 90 degrees orientations.

Although the load rotation method was used in this study, the coordinate systems for the contours in Figure 63 have been rotated to the same global orientation for easier visual comparison. The areas of maximum plastic strain in all orientations tend to occur above and below the inclusion. Much of this plastic strain will reach a shakedown and not accumulate after the first pass, so it is of interest to examine the ERPSI (Equation (28)), a fatigue indicator parameter, for the third pass at each orientation. Shown in Figure 64 are the third-pass ERPSI for 15, 30, 45, 60, 75, and 90 degrees.

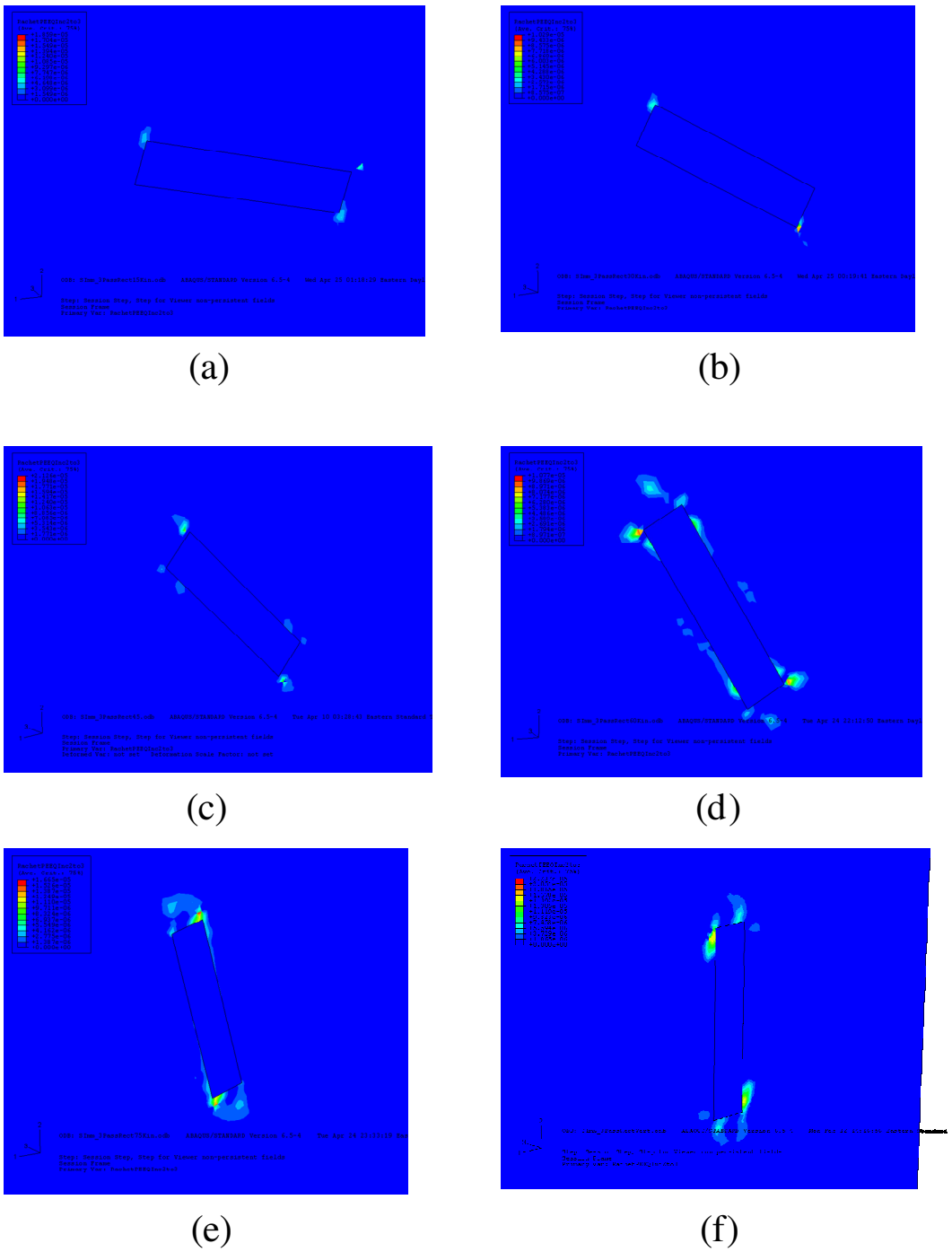

Figure 64. Third-pass ERPSI for (a) 15 degrees, (b) 30 degrees, (c) 45 degrees, (d) 60 degrees, (e) 75 degrees, and (f) 90 degrees orientations.

The accumulation of the ERPSI tends to occur at opposing diagonal corners of the inclusions at all orientations. Shown in Figure 65 is the maximum ERPSI versus inclusion orientation.

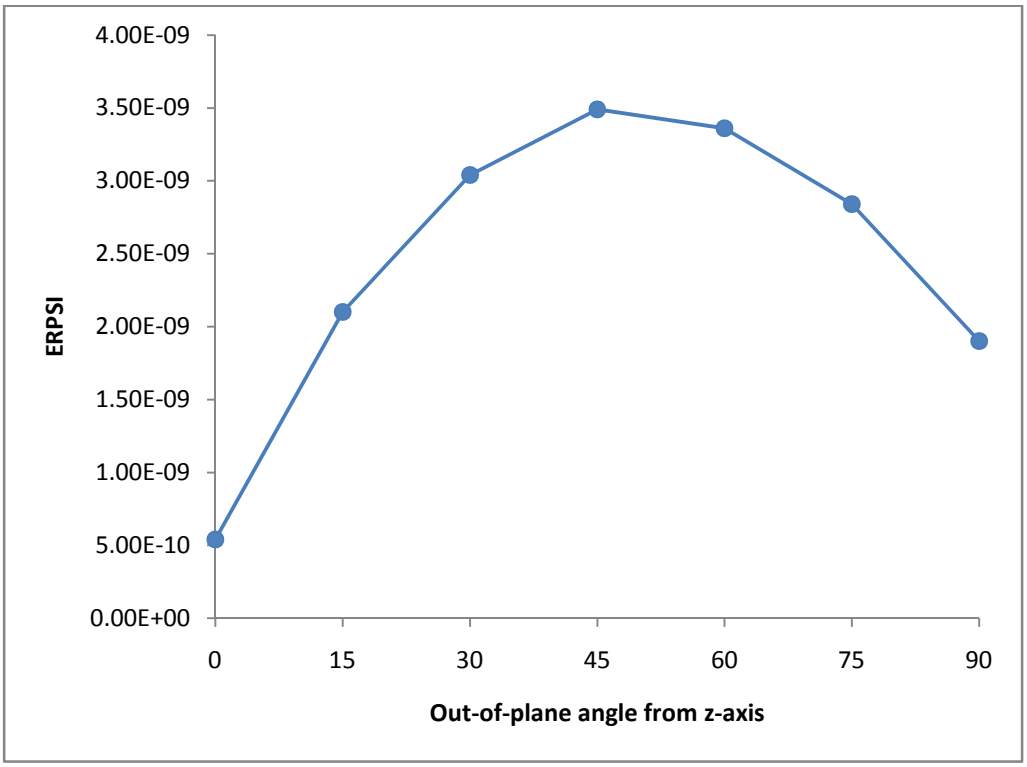

Figure 65. Third-pass ERPSI versus out-of-plane orientation of inclusion.

The highest ERPSI accumulation and therefore lowest corresponding relative fatigue life occurs at forty-five degrees, with a steep gradient at lower angles and shallower at higher angles. This FIP is indicative of the highly localized plastic behavior found surrounding the inclusion.

The Fatemi-Socie parameter in Equation (31) was calculated in the regions immediately surrounding the inclusion based on the plastic strain accumulation during the third roller pass, and this fatigue indicator exhibits similar behavior to that of the

ERPSI. An averaging of local values of adjacent elements of the Fatemi-Socie parameter using the plastic strain increment of the third pass is plotted versus the inclusion orientation angle in Figure 66.

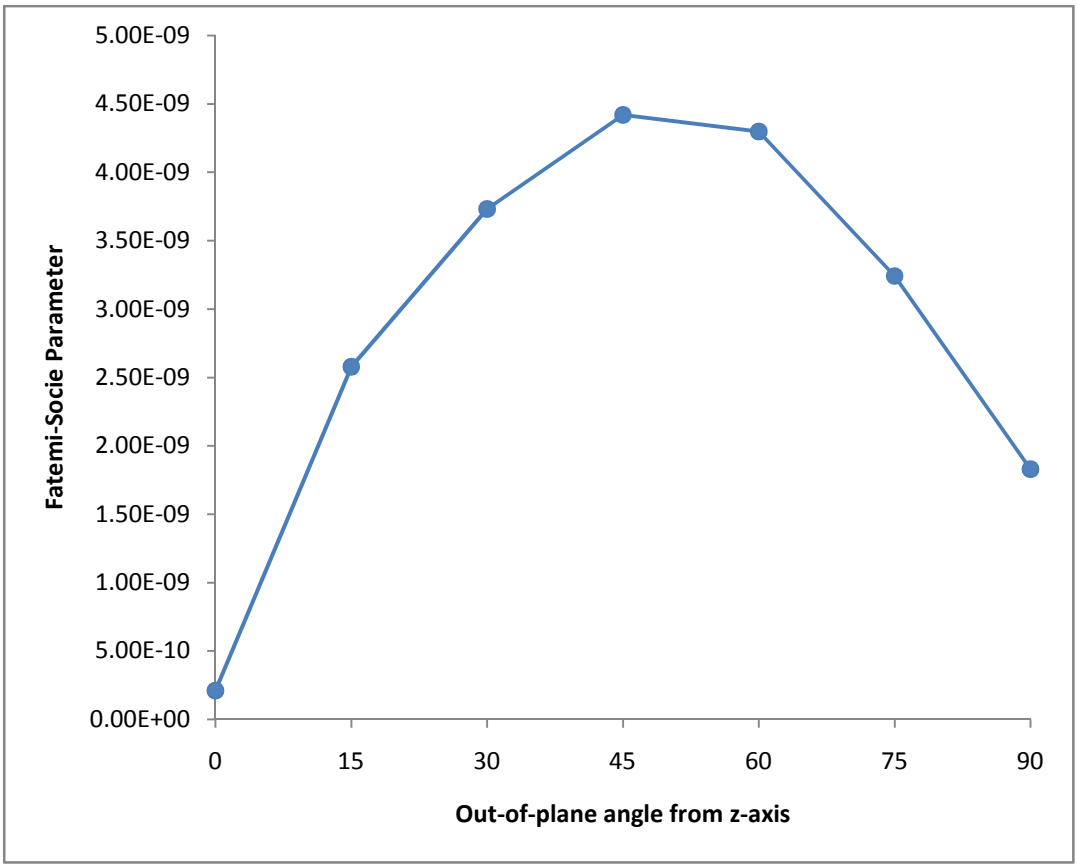

Figure 66. Fatemi-Socie parameter for third pass versus out-of-plane orientation of inclusion.

These results indicate that an out-of-plane inclusion angle in the range of forty-five to sixty degrees yields the highest value of the fatigue indicator parameter, and thus the highest likelihood for nucleation of a fatigue crack at the inclusion corresponding inclusion depth, translating to a lower relative fatigue life than other orientations within that plane. This corresponds well with historical data that a moderate to steep out-of-plane inclusion angle produces the highest rates of bearing failures and lower life spans

[11]. Both the ERPSI and the Fatemi-Socie fatigue indicator parameters exhibit similar behavior in this case, and they both indicate trends consistent with historical data. Therefore, in the case of inclusion orientation, the ERPSI and the Fatemi-Socie parameter are effective measures of relative fatigue life.

4.2 Retained Austenite Effects Study

To showcase the utility of the new two-phase material model, an investigation of the effect of initial volume fraction of retained austenite on the fatigue performance was conducted. An elongated inclusion 10 x 10 x 50 μm with axis oriented in the z-direction was modeled at the depth of the maximum Tresca stress, with an applied Hertzian loading of 2.026 GPa, corresponding to a contact half-width of 260 μm. This loading was selected as representative of that of a typical bearing bench test.

The small-scale volume element model was again used, but for this study utilizes the three-zone partitioned meshing scheme as depicted in Figure 24 and Figure 25. An inner elastic inclusion zone (as shown in Figure 24) is surrounded by the microplasticity zone (shown in Figure 25), which utilizes the new hybrid material model developed in Section 3.3. Outside of the elastic-plastic zone, an outer isotropic elastic zone of base metal exists to smooth the transition of the applied Hertzian loading to the elastic-plastic region. The dimensions and mesh densities for the model are given in Table 11. Rather than a staggered mesh density as used in the previous demonstration study with tetrahedral elements, the solid brick elements (ABAQUS code C3D8R [1]) used here require a uniform mesh density with the partition method.

Table 11. Dimensions of zones and mesh for retained austenite study

Zone	**Outer Dimensions**
Inclusion	50 x 10 x 10 μm
Elastic-Plastic Base Metal	110 x 70 x 70 μm
Elastic Base Metal	150 x 150 x 150 μm
Mesh Region	**Nominal Mesh Element Size**
All	5 μm

The metal matrix elements surrounding the inclusion are each given random lattice orientations to simulate a random texture as would be expected in the initial as-processed material. The gcn option is set to one, giving a mesh with one grain per element.

Shown in Figure 67 are comparison views of the plastic strain distribution for the J_2 homogeneous plasticity model at 2.68 GPa peak Hertzian contact pressure (in both a refined mesh, and the coarser block mesh required for the crystal plasticity model), and for a crystal plasticity model at 2.026 GPa peak Hertzian contact pressure. The block meshing provides a coarser distribution of plastic strain, but of the same shape and pattern as that of the more fine tetrahedral mesh. The use of block elements is well-suited for the crystal plasticity model, which provides a more inhomogeneous distribution of plastic strains than that given by the J_2 model.

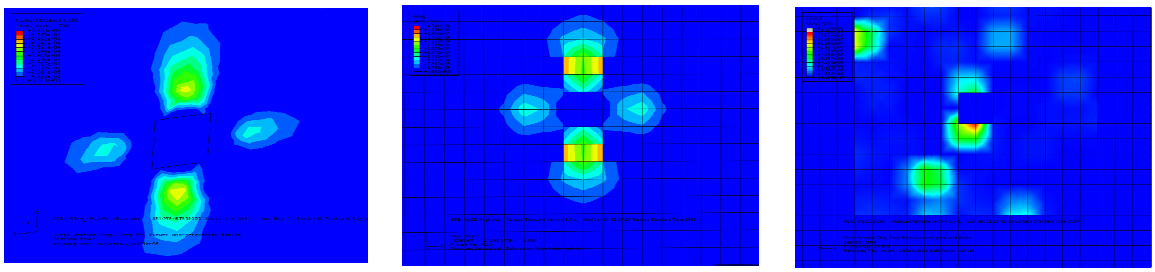

(a) (b) (c)

Figure 67. Plastic strain response for (a) J_2 fine mesh, p_0 = 2.68GPa, (b) J_2 block mesh, p_0 = 2.68GPa, (c) Crystal plasticity block mesh, p_0 = 2.026GPa.

It is of interest to note that the J_2 plasticity model does not capture any localized plastic strains at the 2.026 GPa peak pressure because the localized response remains below the macroscopic yield strength. This indicates the utility of using the crystal plasticity model in capturing localized plastic strains not detected by a macroplasticity model.

To demonstrate the crystal plasticity model's advantages, three-pass rolling contact simulations were conducted with different initial volume fractions of retained austenite between 0 and 22%, which is typically the largest percentage found in practical bearing manufacturing [11]. The material parameters for input into the ABAQUS UMAT are those calibrated via the experiments and laid out in Table 9. All parameters used remain the same, except for the initial critical driving stress, $\left(f_{cr}^{(\lambda)}\right)_0$, and the direct hardening parameter of transformation, Q. These parameters vary with initial retained austenite according to Equations (121) and (122), respectively. Given for reference in Table 12 are the values of these two parameters for the different initial volume fractions examined.

Table 12. Transformation parameters for each used initial volume fraction of retained austenite.

Initial volume fraction of retained austenite	$\left(f_{cr}^{(\lambda)}\right)_0$ (MPa)	Q (MPa)
0%	N/A	N/A
4%	152.8	856.5
7%	141.9	788.3
10%	131	720
13%	120	650
16%	109.2	583.3
19%	98.3	516.7
22%	87.5	450

The effects of retained austenite content on material response are significant. Large amounts of transformation in the material from austenite to martensite cause a volume expansion from face-centered to approximately a body-centered lattice structure. This induces additional compressive residual stresses locally that depend on the microstructure. These simulations suggest that this has the effect of increasing the local accumulation of plastic strains. Since the Hertzian rolling contact loading produces a compressive stress state, the two loadings (applied and residual) compound together, and add to the resolved shear stresses which activate the slip systems.

For better visualization of fatigue indicator parameters, transformation amounts, and residual stresses in this study, all figures will shown only the elastic-plastic region identified in Figure 25. Additionally, the figures afford a view of the region immediately

surrounding the inclusion via a cut along the y-z plane. All of the simulations utilize the same mesh, with a variation of the material parameters given in Table 12. Thus, the orientation of the elements is uniform for all cases, since the random orientations chosen by the ABAQUS UMAT are based on a formulation containing the element number. Using the same mesh gives the same distribution of grain orientations. Shown in Figure 68, Figure 69, and Figure 70 are contour plots of the third-pass effective ratcheting plastic strain increment (ERPSI), as defined by Equation (28), for 0%, 13%, and 22% initial retained austenite.

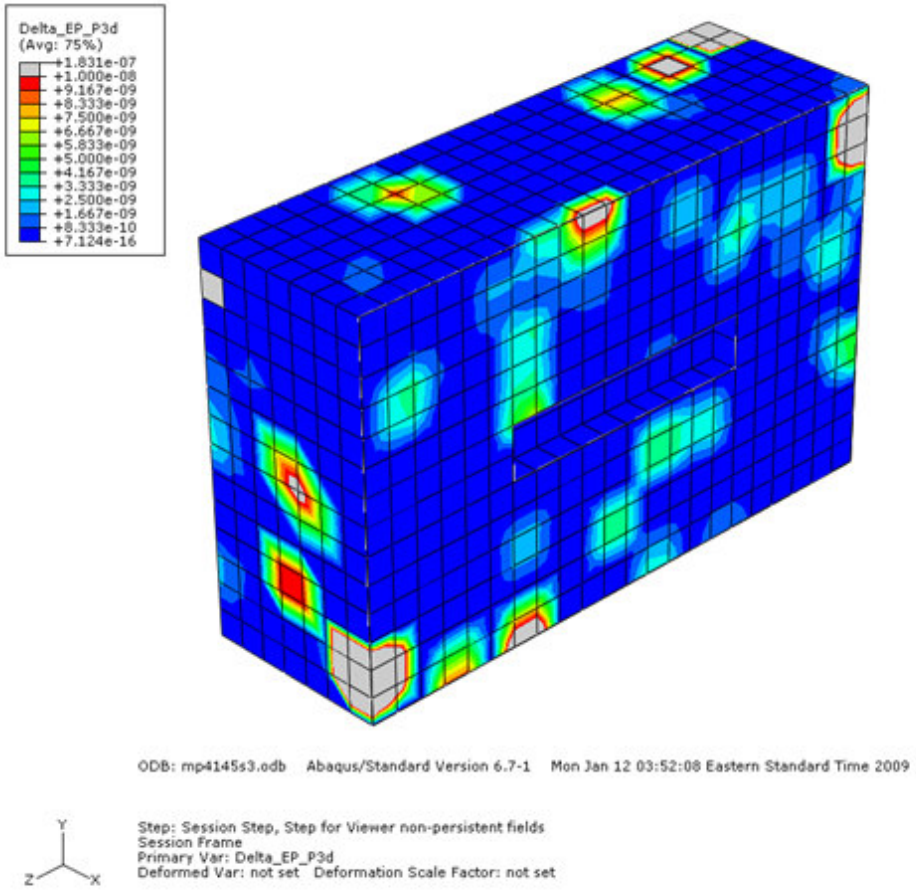

Figure 68. Third-pass ERPSI for 0% initial volume fraction of retained austenite.

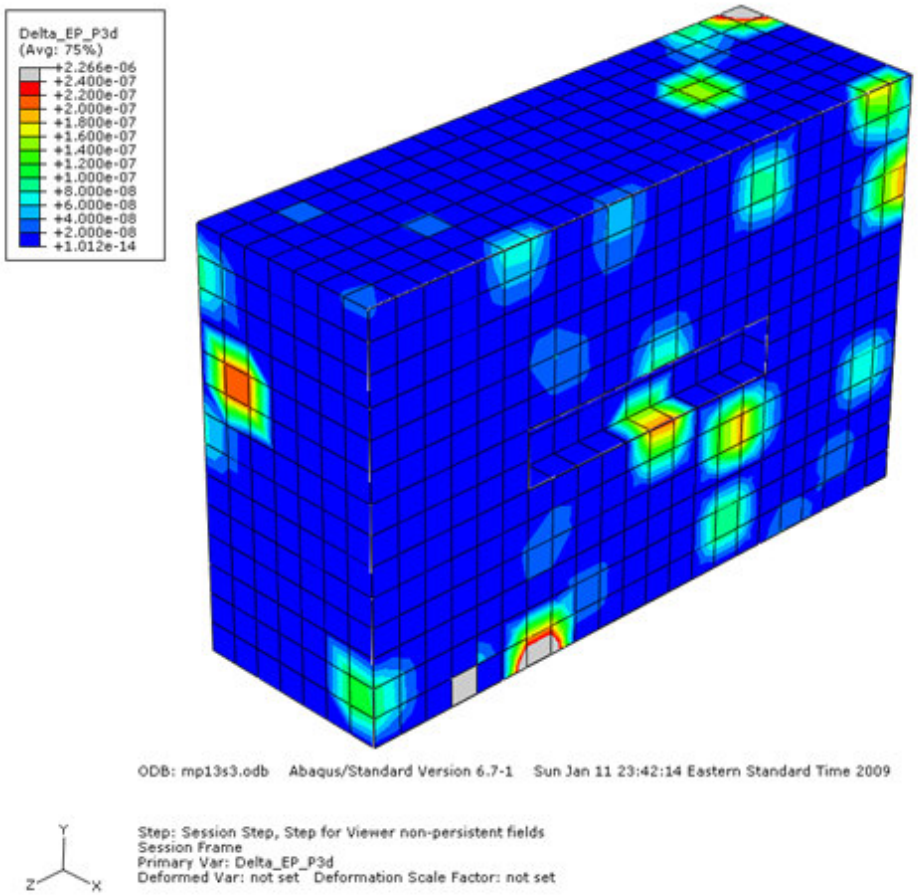

Figure 69. Third-pass ERPSI for 13% initial volume fraction of retained austenite.

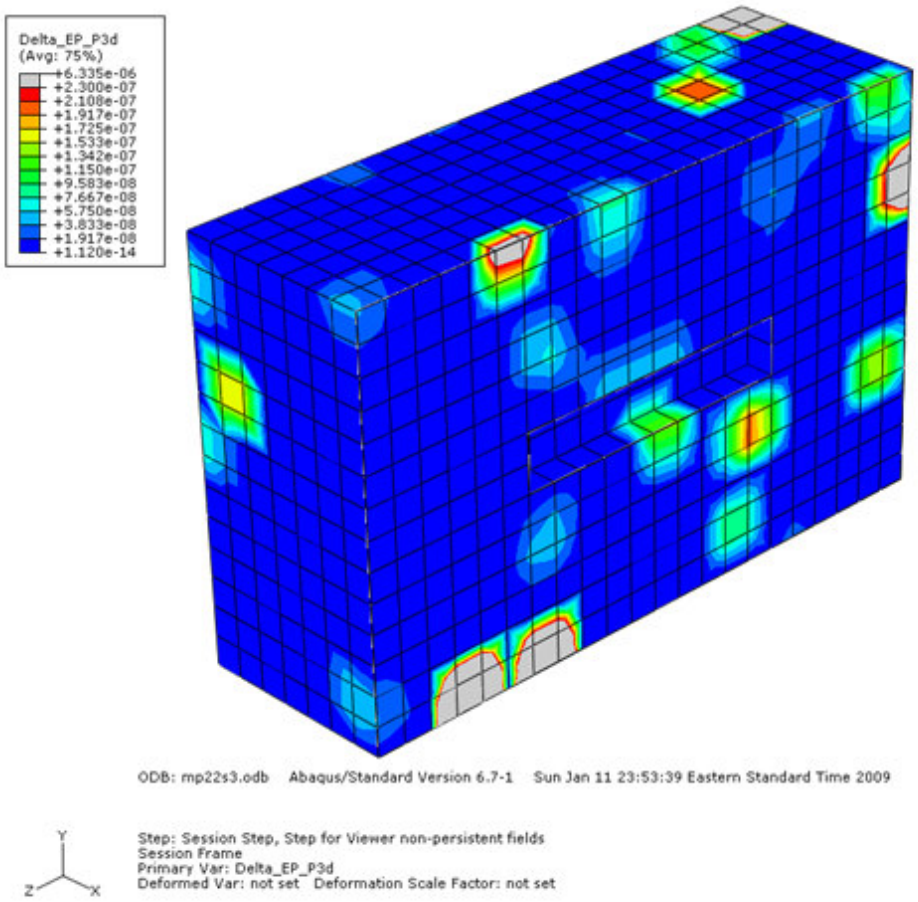

Figure 70. Third-pass ERPSI for 22% initial volume fraction of retained austenite.

Due to the differences in response of the isotropic elastic elements surrounding the crystal plasticity region, some edge effect exists within one element of the boundary. This is visible in the contours presented, along the outer edges of the microplastic zone. Thus, the data collected for graph comparisons does not include the outer-most crystal plasticity elements. The variation in ERPSI with initial volume fraction is shown in Figure 71. Two values are presented, the maximum ERPSI found in the region (excluding elements on the outer-most boundary), and the average value of this FIP for the crystal plasticity region (also excluding the outer-most boundary).

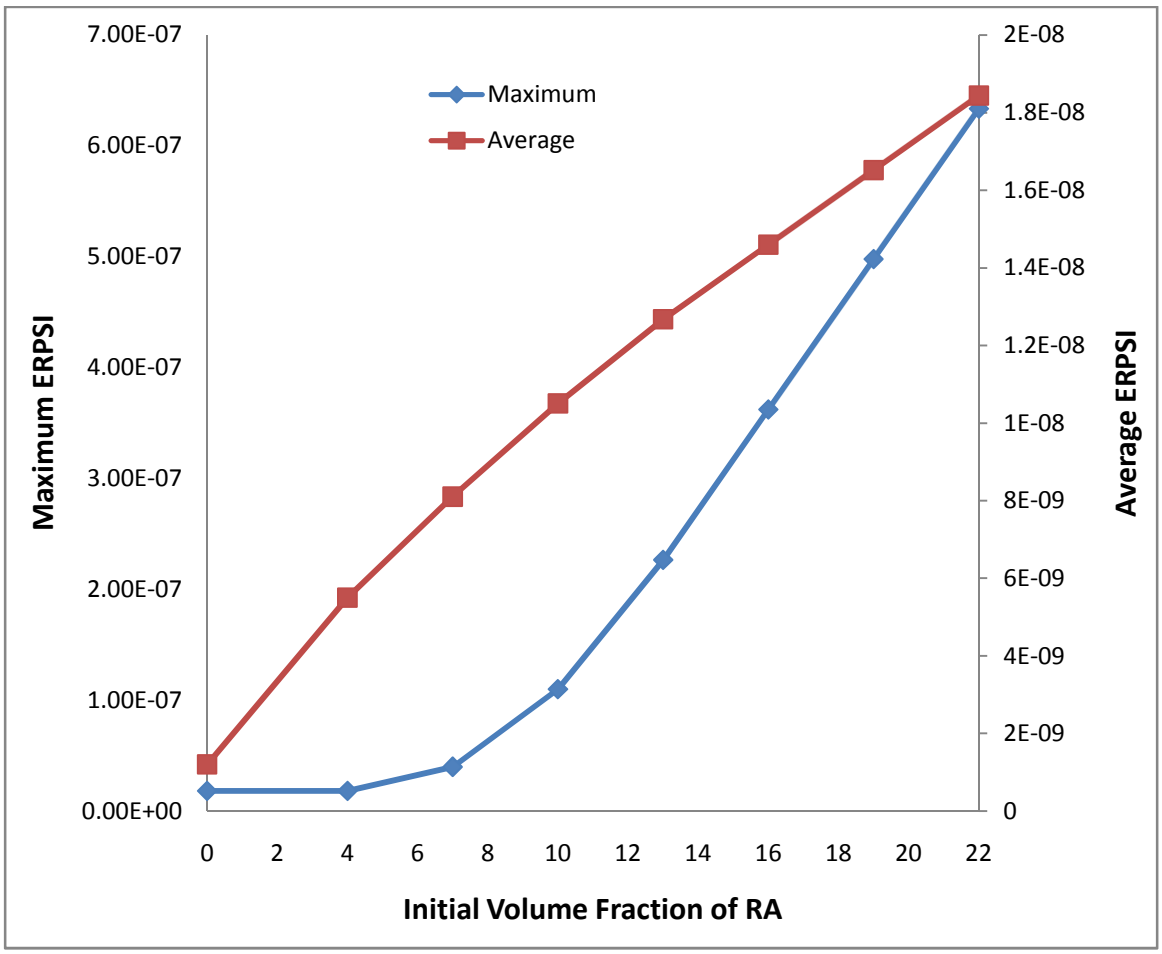

Figure 71. ERPSI vs. initial volume fraction of retained austenite.

The trend for both the maximum and average values is an increase with an increase in initial volume fraction, with some differences. The average value of the ERPSI climbs fairly steadily with increasing RA. The maximum ERPSI exhibits a steeper rate of climb following a period of minimal change in the smallest RA amounts. This can be attributable to the threshold value of the critical driving stress reaching a value at which the propensity for transform approaches the propensity for martensitic plasticity, in the approximate range of 4% to 7% RA.

Shown in Figure 72, Figure 73, and Figure 74 are comparison views of the Fatemi-Socie Parameter (Equation (31)), which was calculated over the third pass for 0%, 13%, and 22% initial retained austenite. The edge effects are again apparent in these contours, and amounts given in the comparison graphs exclude those elements' values.

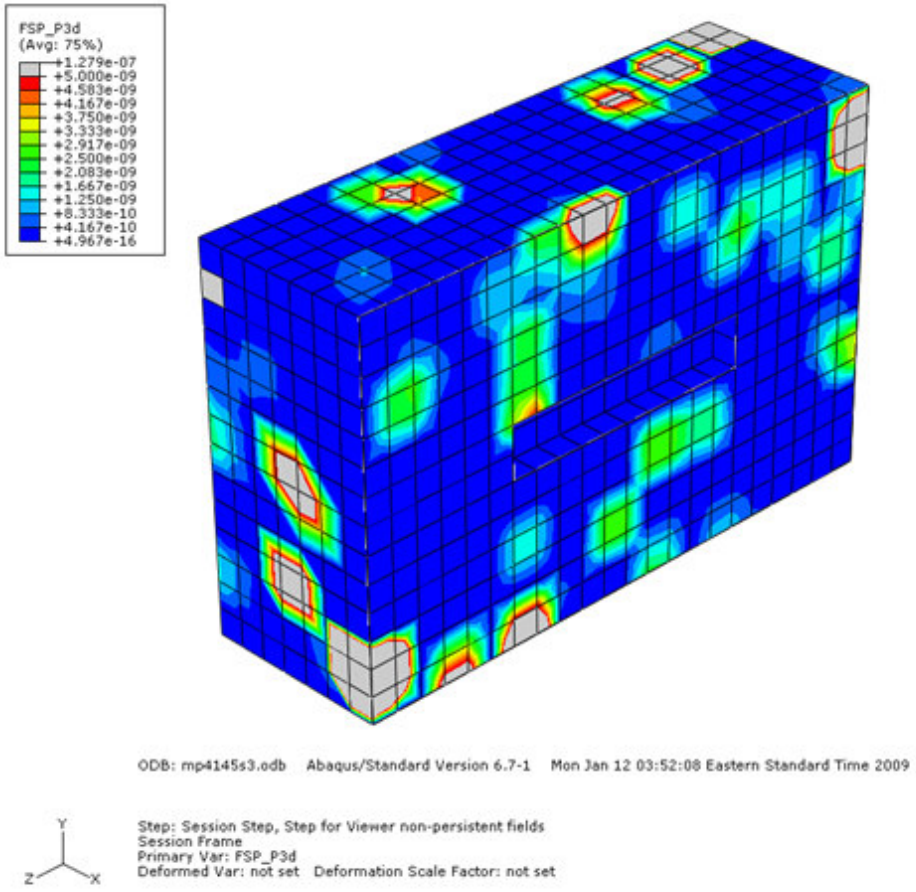

Figure 72. Third-pass Fatemi Socie parameter for 0% initial volume fraction of retained austenite.

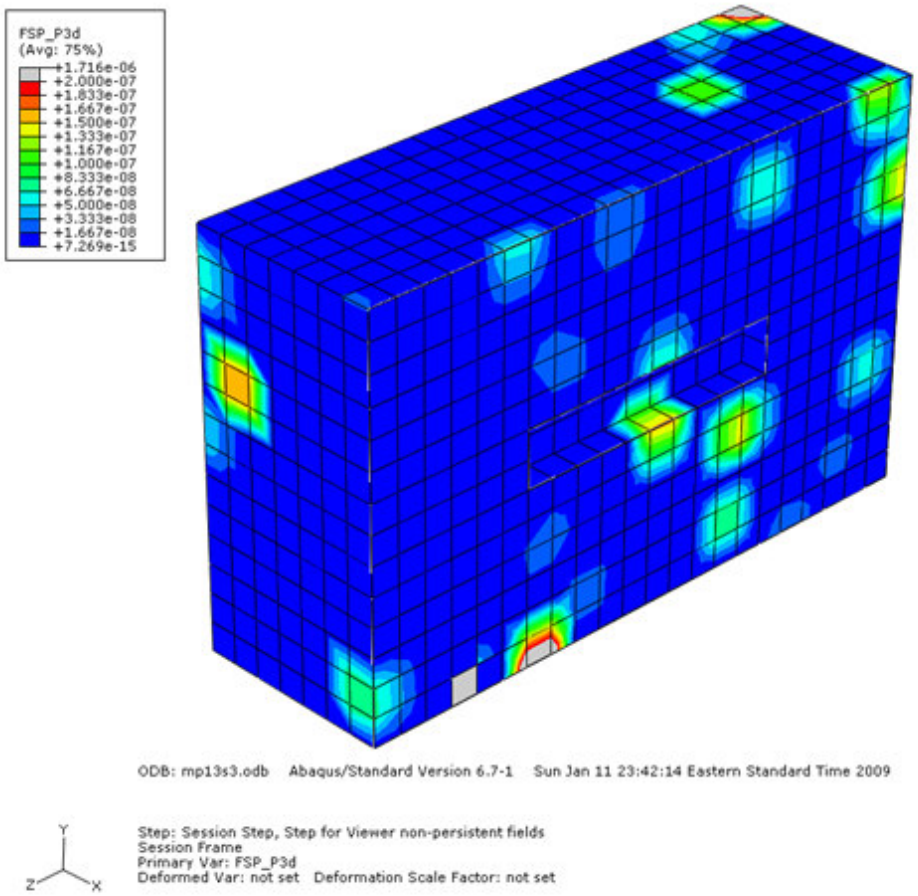

Figure 73. Third-pass Fatemi Socie parameter for 13% initial volume fraction of retained austenite.

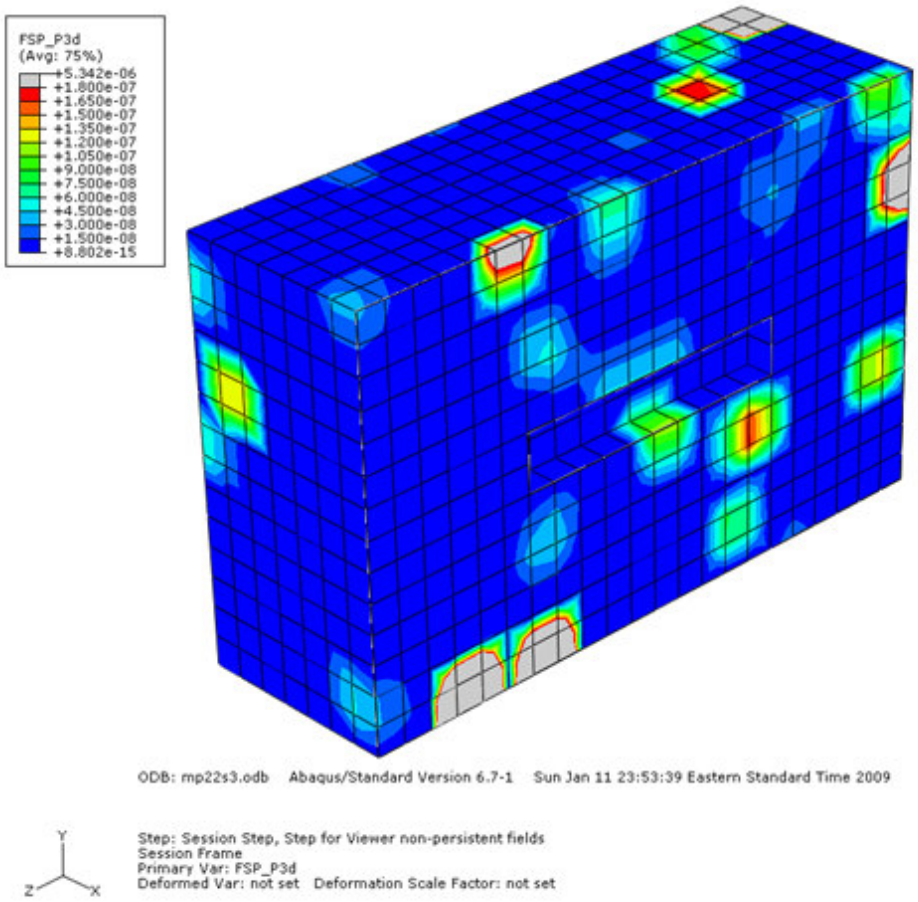

Figure 74. Third-pass Fatemi Socie parameter for 22% initial volume fraction of retained austenite.

Note that the magnitude and extent of this fatigue performance metric also increases with increasing retained austenite, indicating fatigue life degrades with increasing retained austenite. Figure 75 shows the maximum and average values of the two of the Fatemi-Socie Parameter as a function of initial retained austenite.

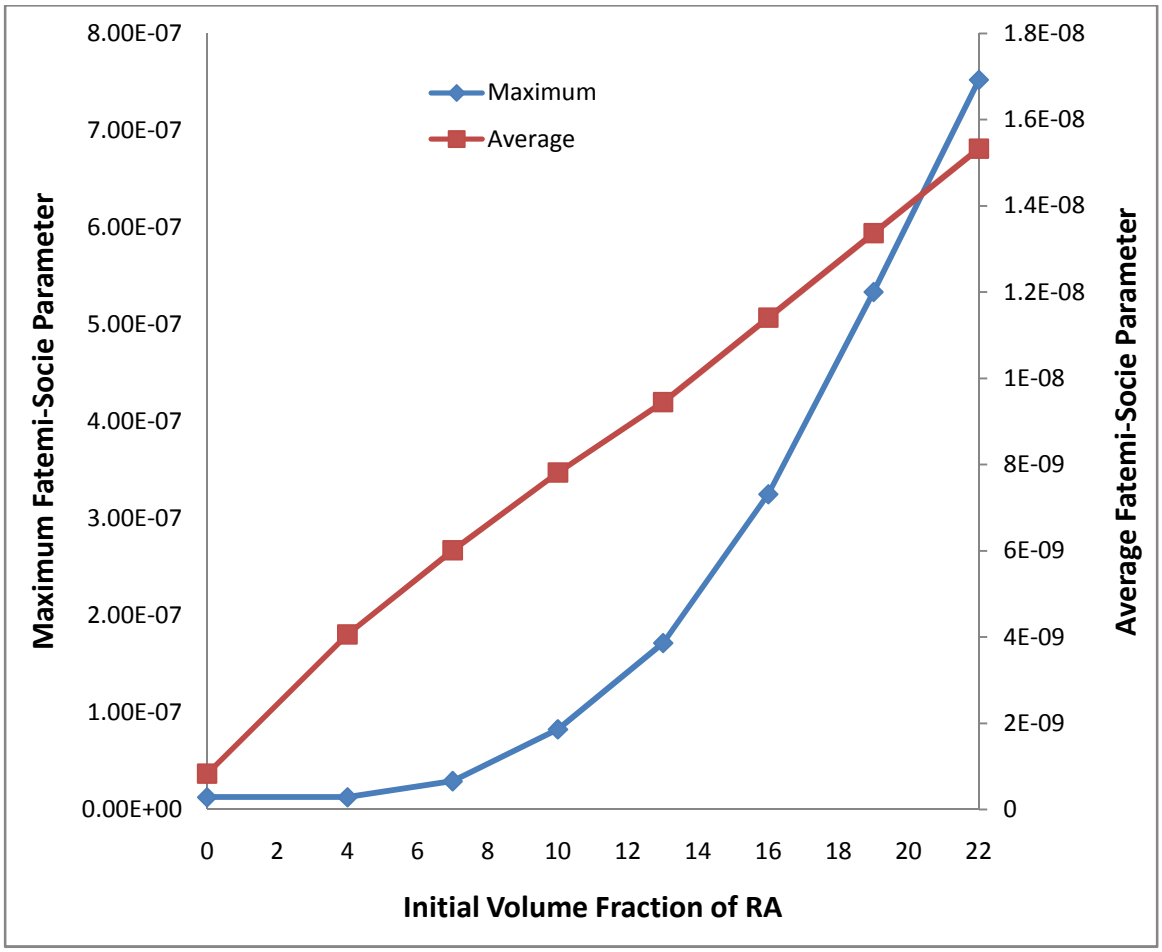

Figure 75. Fatemi-Socie parameter vs. initial volume fraction of retained austenite.

The maximum and average value data points present a pattern closely resembling the ERPSI graphs. Thus, the two FIPs suggest similar trends, with fatigue performance degrading with increasing levels of retained austenite.

In addition to the plastic strain accumulation, it is of interest to examine the transformation strain and the evolution of the volume fraction of retained austenite during the rolling contact fatigue cycles. Shown in Figure 76 and Figure 77 are contour plots of the volumetric transform strain accumulated for 13% and 22% initial retained austenite.

All data points for both the maximum and average value of the volumetric transform strain are shown in Figure 78 versus percentage of initial retained austenite.

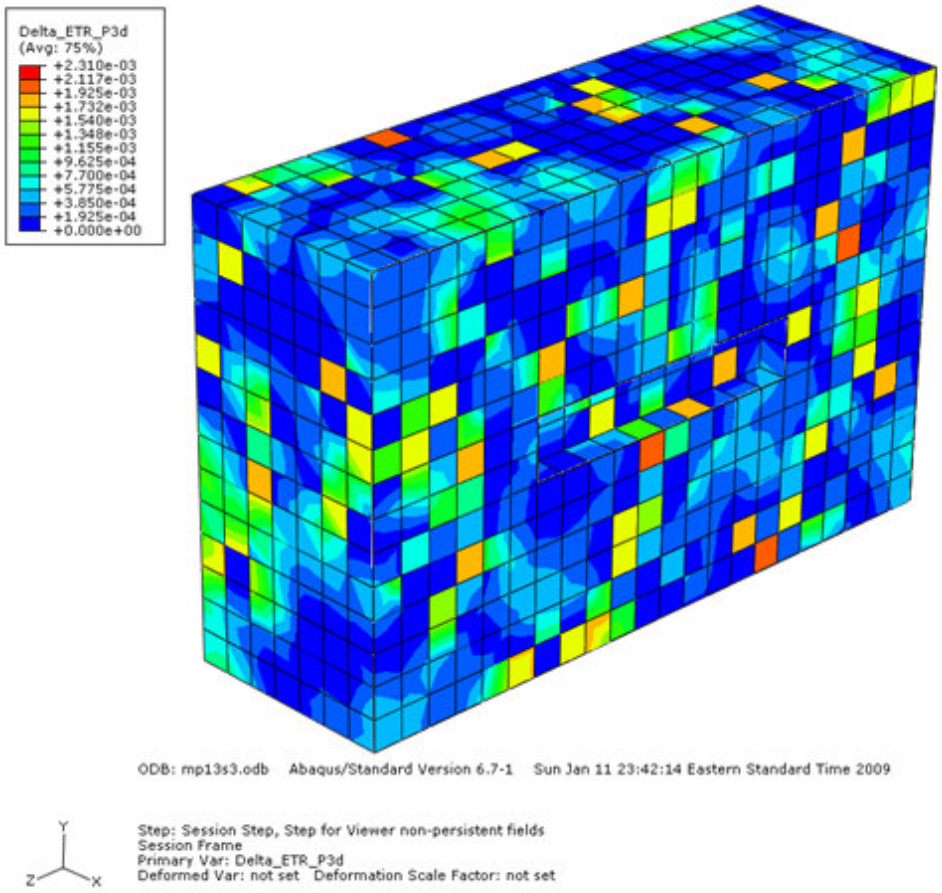

Figure 76. Volumetric transform strain for 13% initial volume fraction of retained austenite.

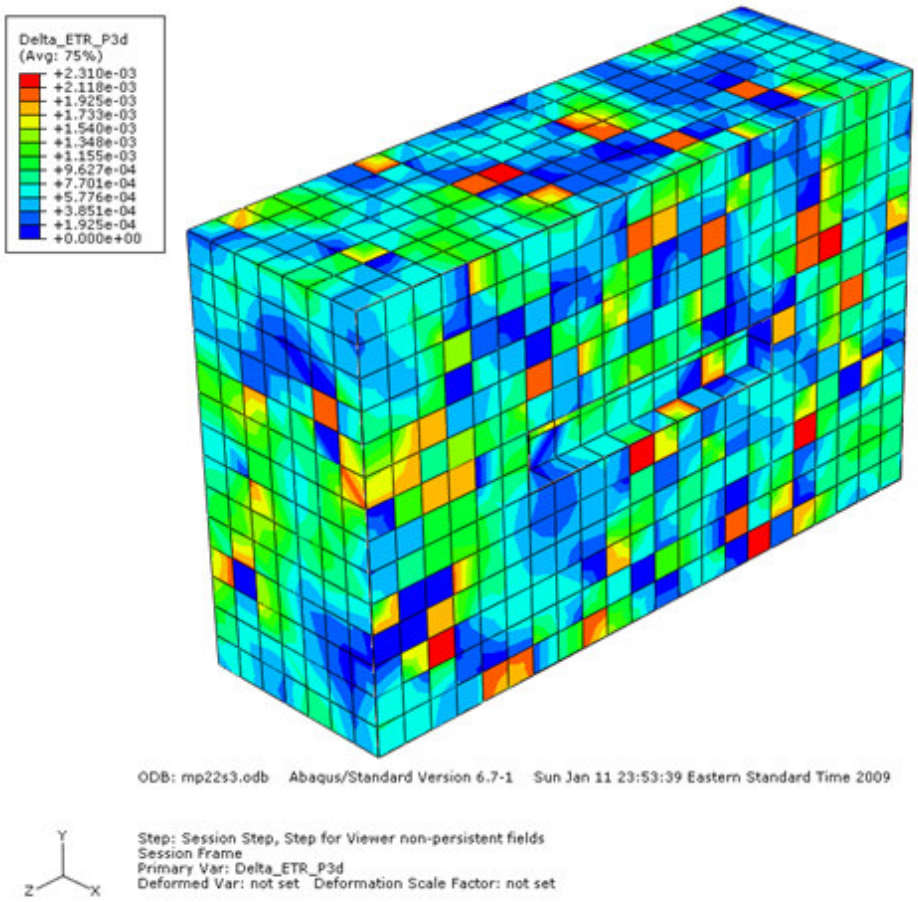

Figure 77. Volumetric transform strain for 22% initial volume fraction of retained austenite.

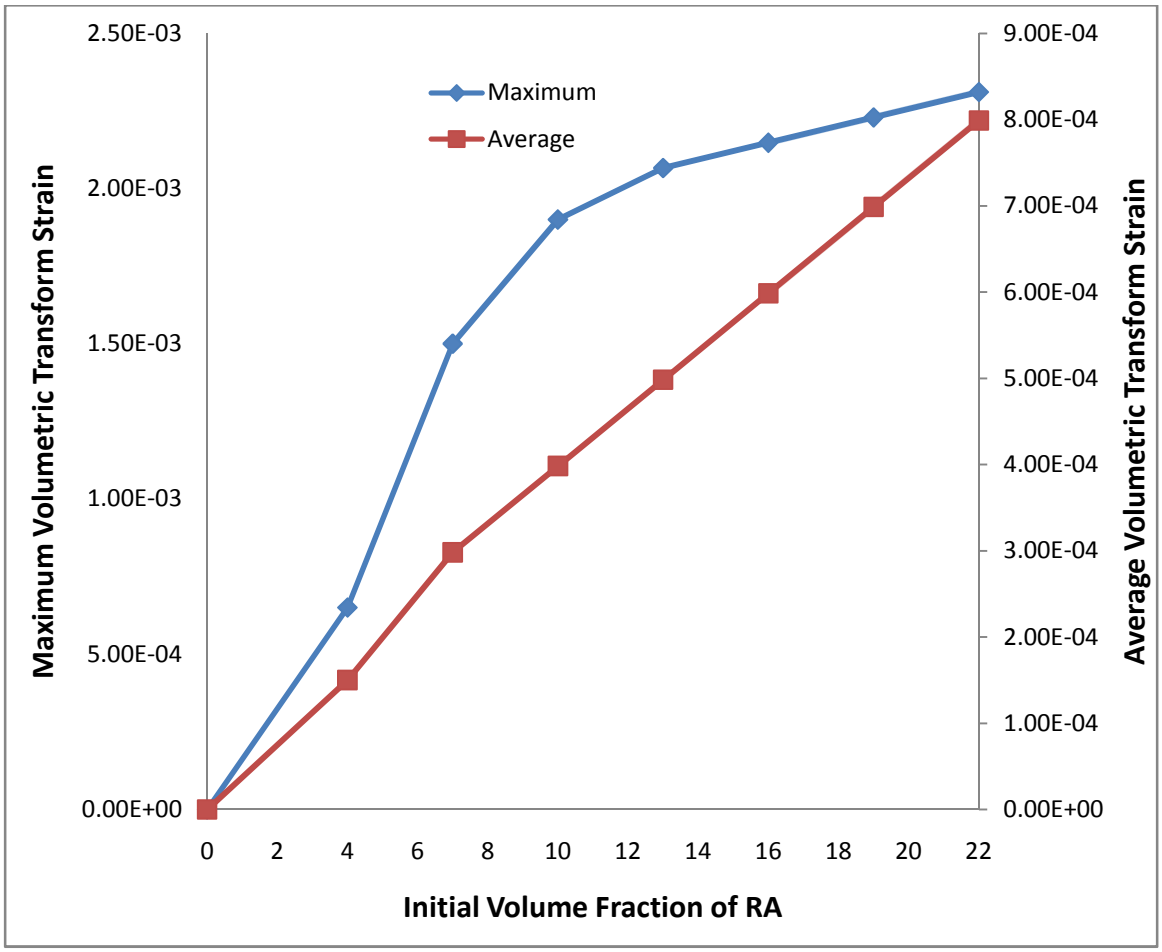

Figure 78. Volumetric transform strain vs. initial volume fraction of retained austenite.

As expected, there is an increase in transformation strain with increasing initial retained austenite, as there is a decrease in the threshold for transformation with increasing austenite. The left-hand side of both graphs is anchored at the origin, as no transformation can occur in the 0% initial RA case.

It is also of interest to examine the amount and distribution of transformation occurring in the crystal plastic region, expressed as a percentage of the whole volume that has transformed per element, in total over the three passes. Shown in Figure 79 and Figure 80 are contour plots of the percentage of transformation by volume fraction.

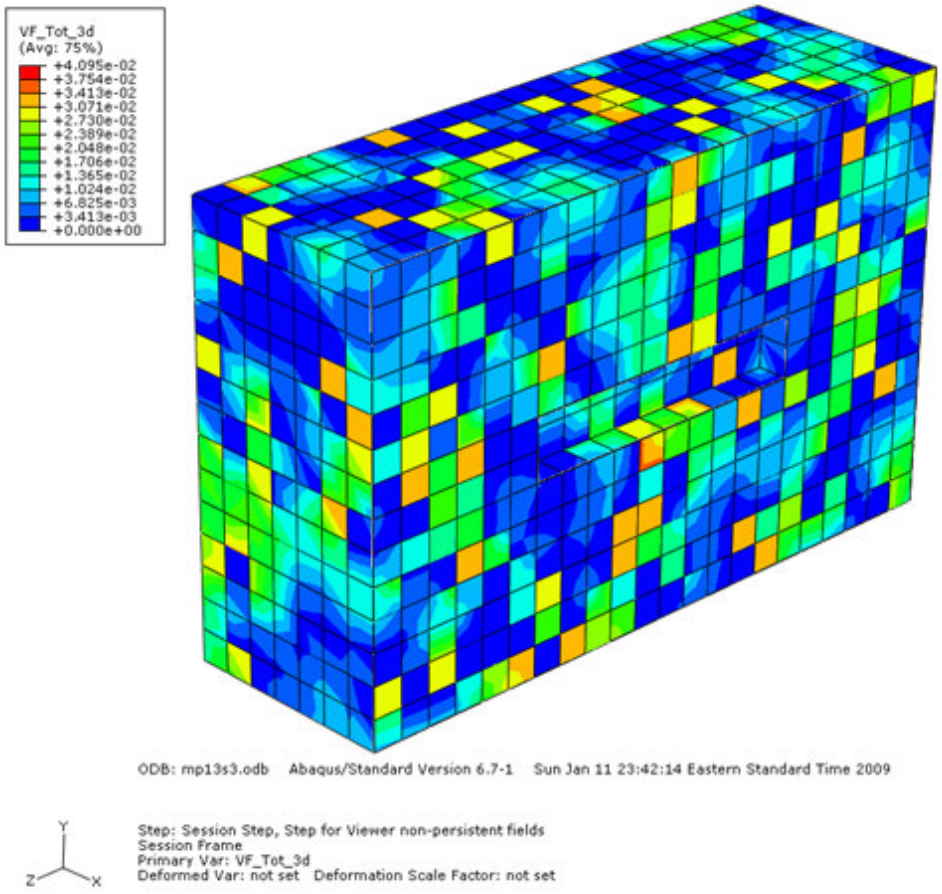

Figure 79. Volume fraction transformed for 13% initial volume fraction of retained austenite.

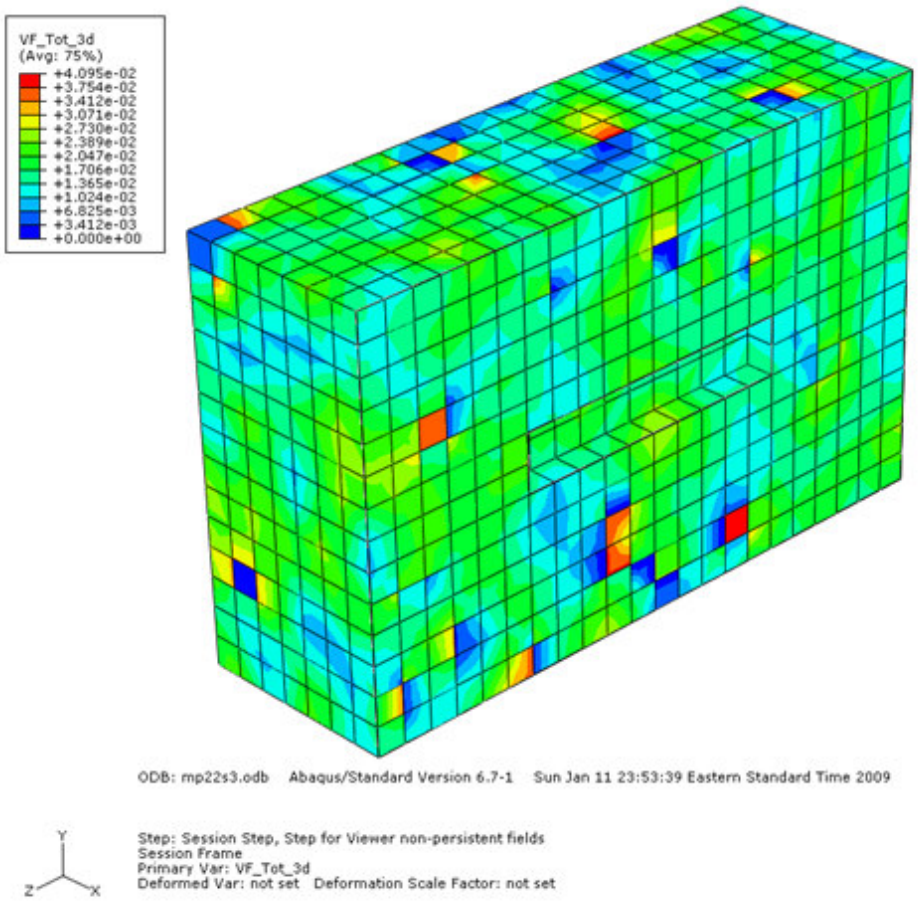

Figure 80. Volume fraction transformed for 22% initial volume fraction of retained austenite.

Of interest to note is that while some localized regions in both cases exhibit maximum transformation near 4%, there is much more comprehensive transformation occurring in the higher retained austenite case. This is apparent in the maximum and average percentages of volume fraction transformed that are shown in Figure 81, versus percentage of initial retained austenite. While the maximum values seem to reach a saturation value between 3.5% to 4% when the initial retained austenite is greater than 10%, the average value is more distinctive, with a steadier rate of climb with initial volume fraction.

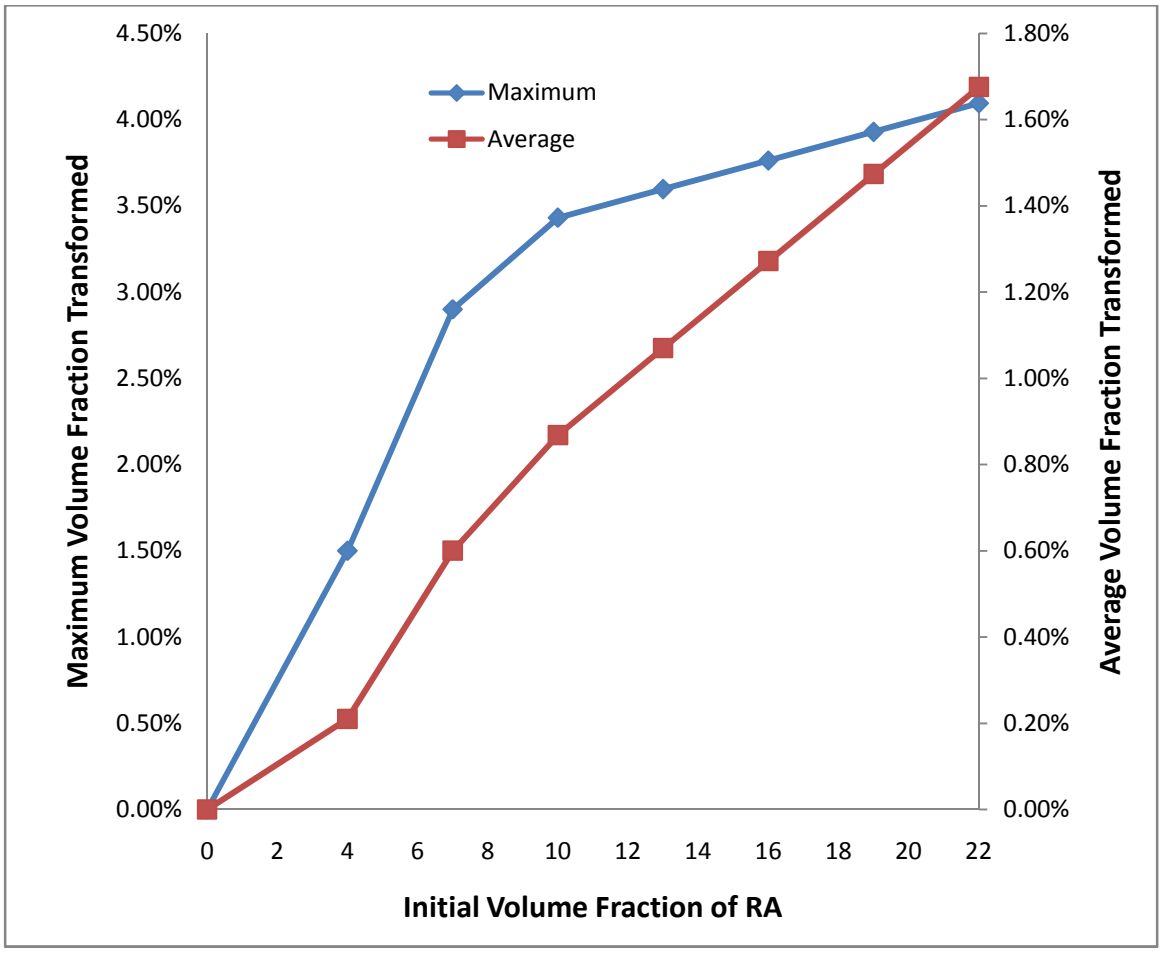

Figure 81. Volume fraction transformed vs. initial volume fraction of retained austenite.

The residual stress field is also of interest to examine. The contours of the von Mises effective residual stresses for 0%, 13%, and 22% initial retained austenite for a step with no applied loading following the third roller pass are given in Figure 82, Figure 83, and Figure 84.

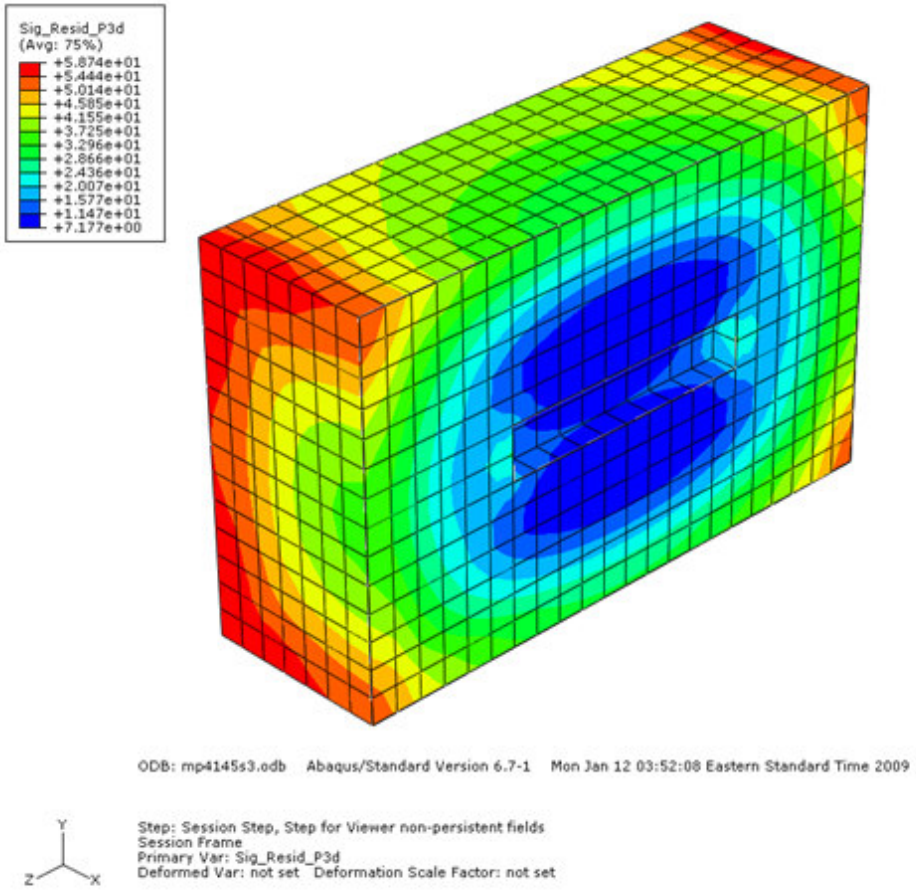

Figure 82. Von Mises effective residual stress for 0% initial volume fraction of retained austenite.

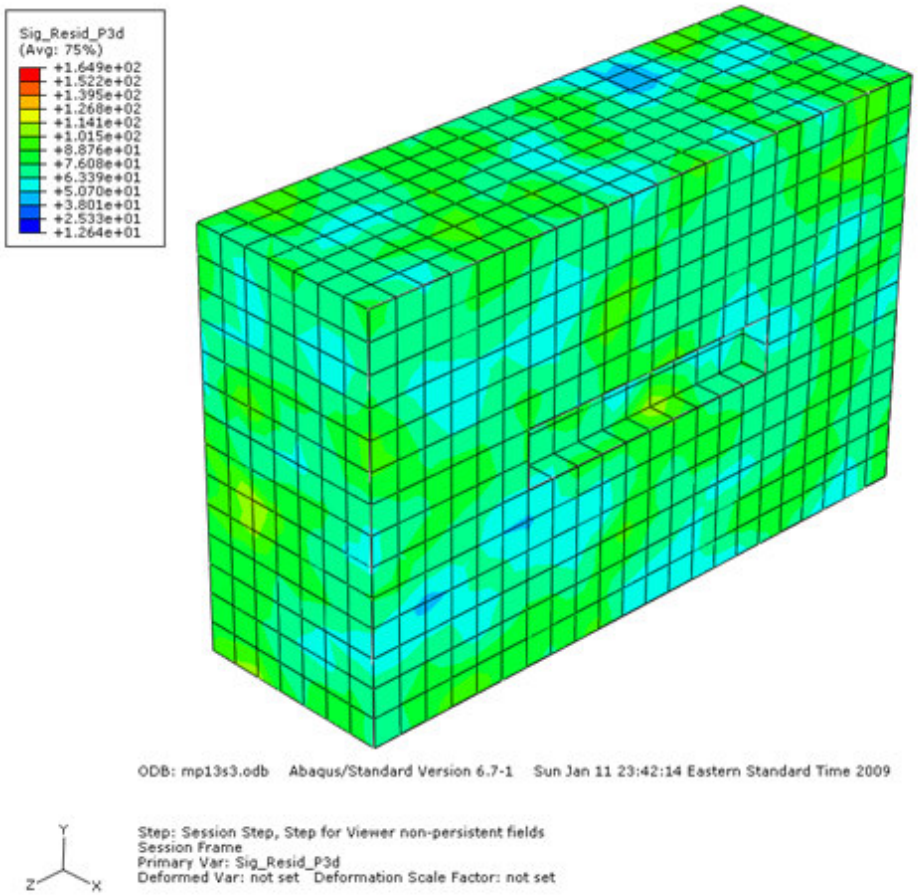

Figure 83. Von Mises effective residual stress for 13% initial volume fraction of retained austenite.

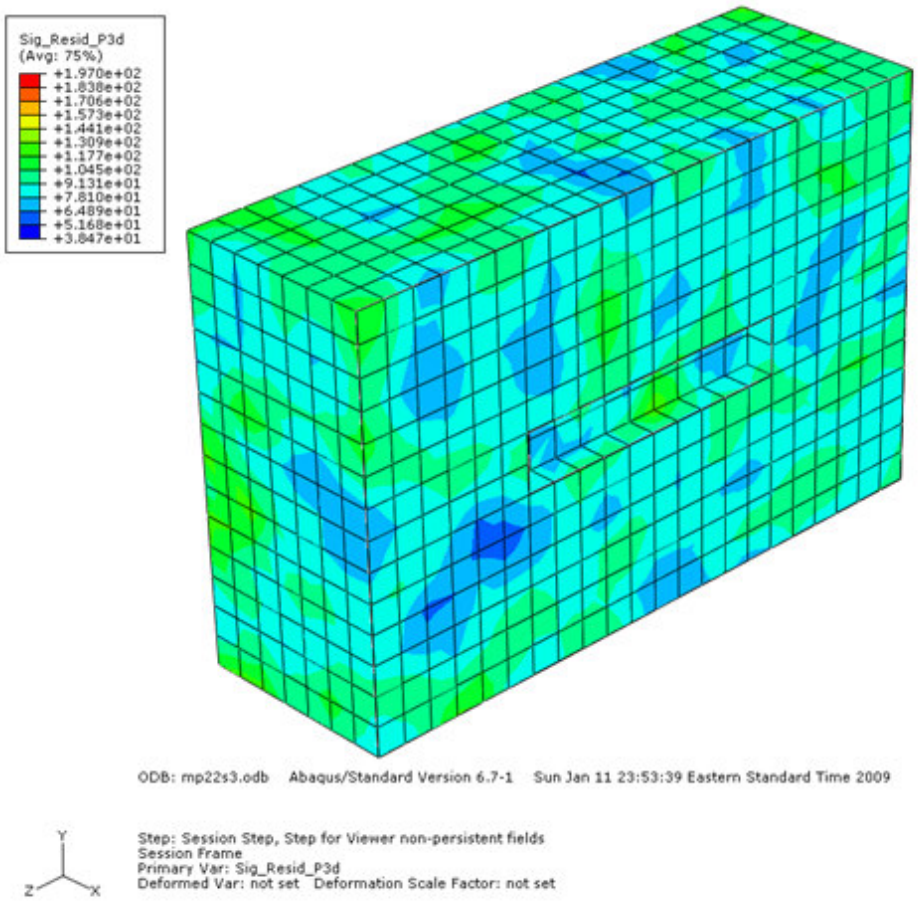

Figure 84. Von Mises effective residual stress for 22% initial volume fraction of retained austenite.

All data points for both the maximum and average value of the effective residual stress are shown in Figure 85 versus percentage of initial retained austenite. It can be seen that for the case of no initial retained austenite, the von Mises effective residual stress is greatly reduced surrounding the inclusion, due to the high state of hydrostatic stress that the inclusion creates. The transformation of retained austenite results in more von Mises effective residual stress, caused by an inhomogeneous pattern in the transformation strains. This also leads to a negation of the inclusion's effect on the residual stress field.

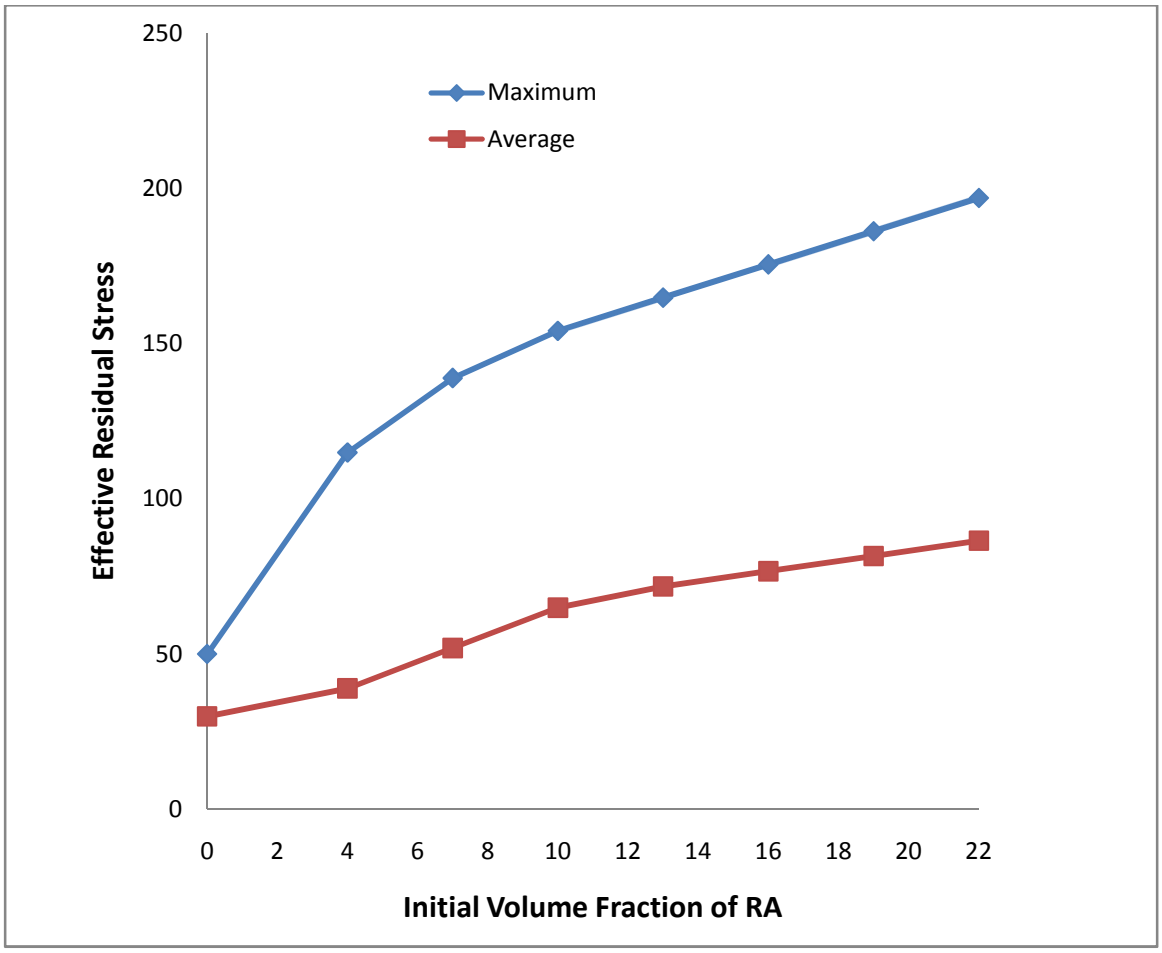

Figure 85. Von Mises effective residual stress vs. initial volume fraction of retained austenite.

The hydrostatic residual stresses are shown in Figure 86, Figure 87, and Figure 88 for 0%, 13%, and 22% initial retained austenite, respectively.

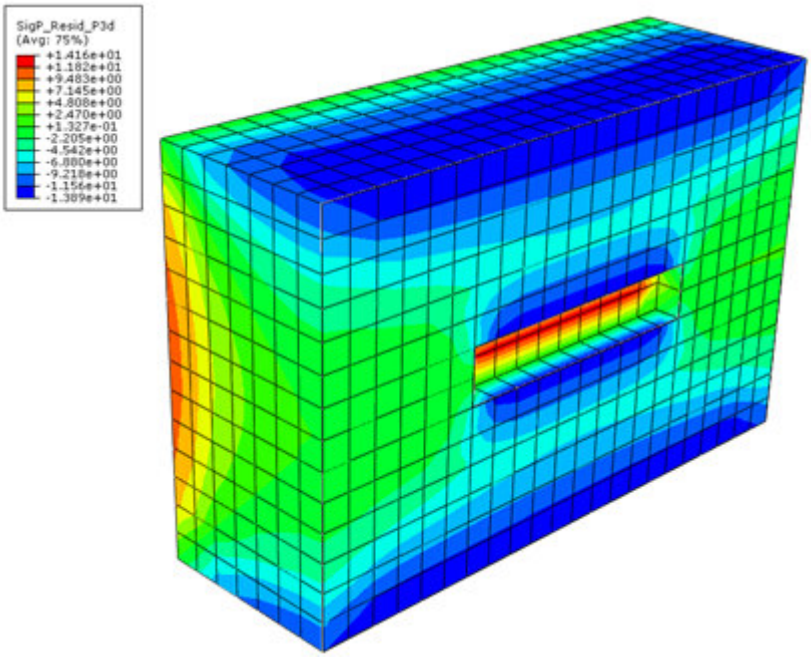

(a)

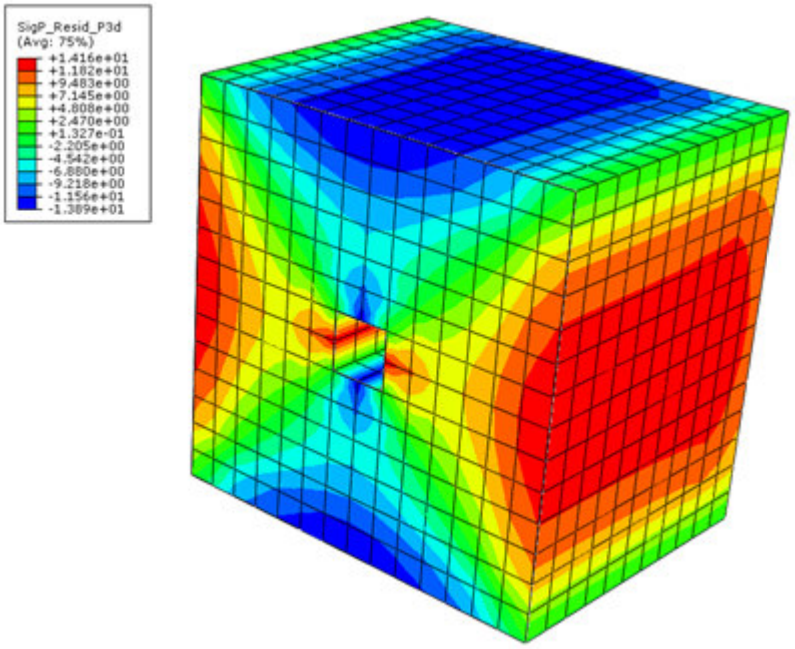

(b)

Figure 86. Hydrostatic residual stress for 0% initial volume fraction of retained austenite for (a) x-plane normal cut view, and (b) z-plane normal cut view.

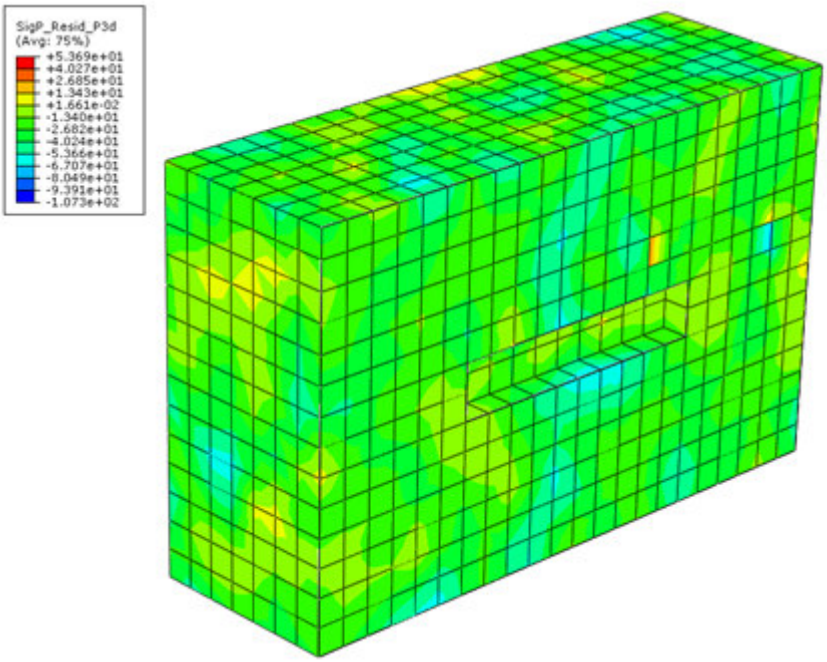

(a)

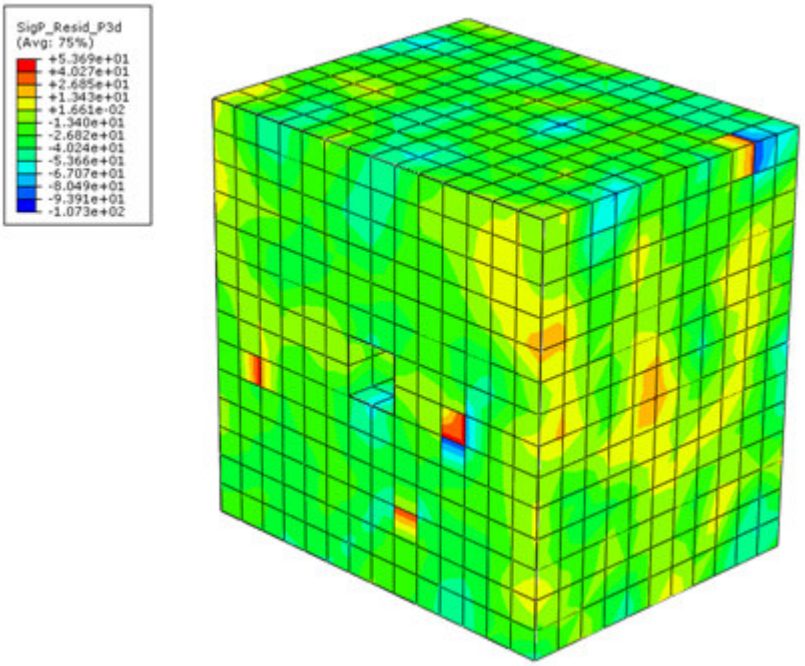

(b)

Figure 87. Hydrostatic residual stress for 13% initial volume fraction of retained austenite for (a) x-plane normal cut view, and (b) z-plane normal cut view.

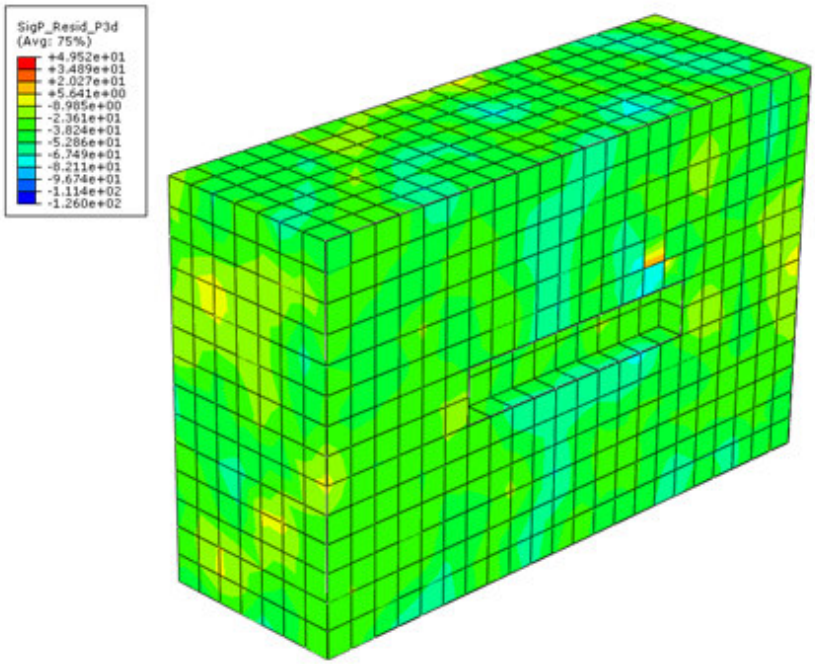

(a)

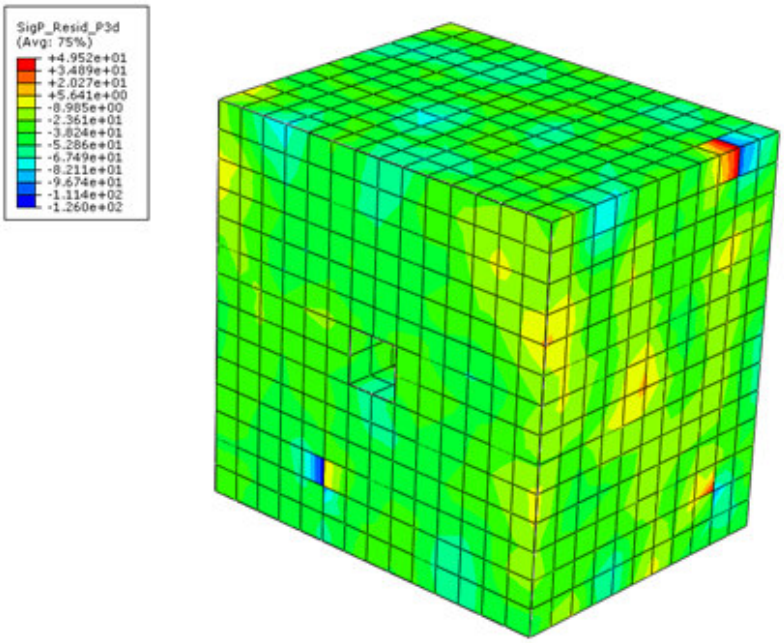

(b)

Figure 88. Hydrostatic residual stress for 22% initial volume fraction of retained austenite for (a) x-plane normal cut view, and (b) z-plane normal cut view.

As with the case of the von Mises effective residual stress, the hydrostatic stress in the 0% initial retained austenite case exhibits a very regular-shaped pattern, where the inclusion is the central driving feature. The 13% and 22% retained austenite cases present a more inhomogeneous response, with the transformation strains playing a significant role in the residual stresses compared with the inclusion. Note that the "hot spots" for the hydrostatic residual stresses tend to occur in areas other than immediately adjacent to the inclusion in these cases. The maximum positive, maximum negative, and average values of the hydrostatic residual stresses are shown in Figure 89 versus percentage of initial retained austenite.

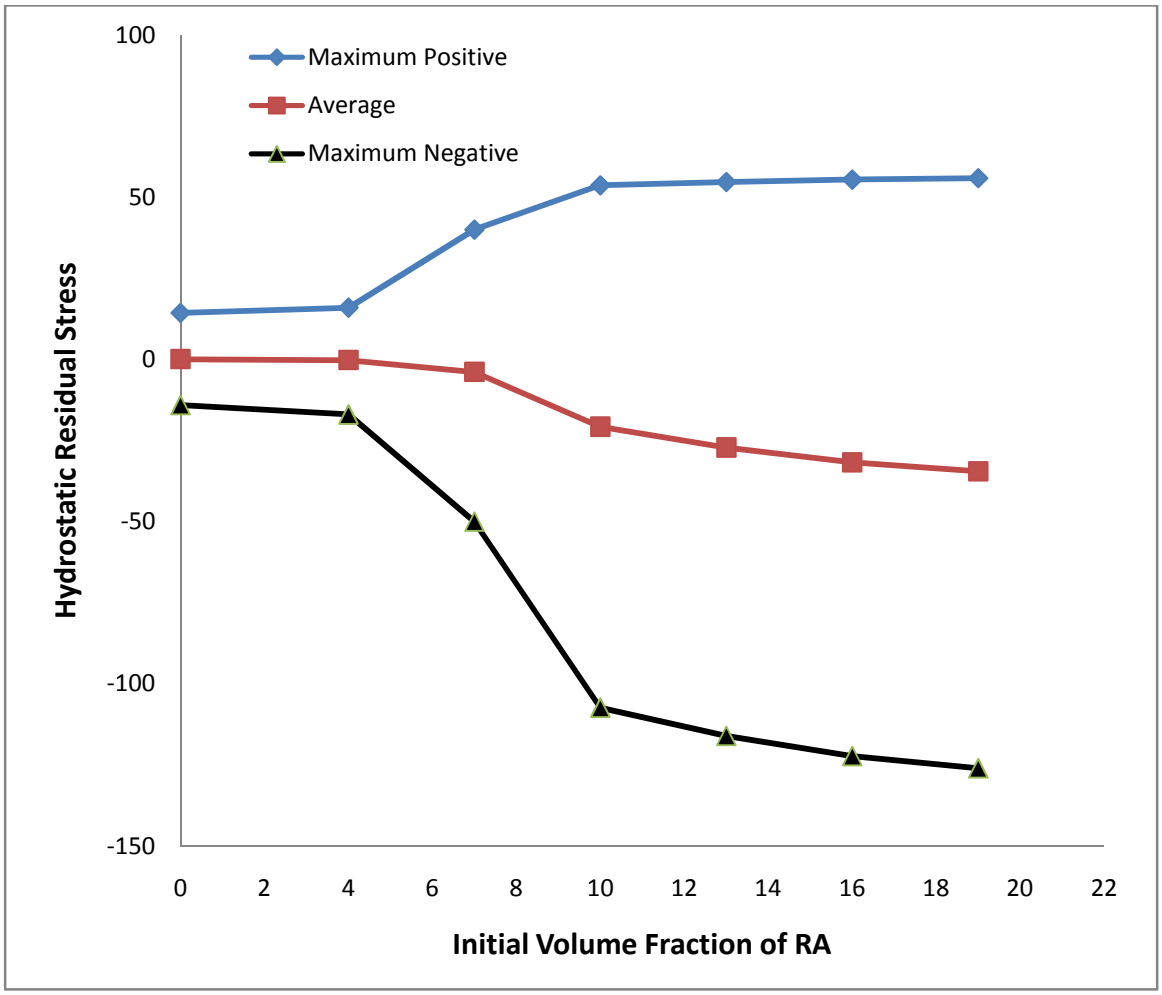

Figure 89. Hydrostatic residual stress vs. initial volume fraction of retained austenite.

The hydrostatic state of stress at 0% initial retained austenite, as depicted in Figure 86, shows the compressive stress state above and below, and tensile stress state to the sides of the inclusion. The symmetry of the positive and negative contours nets an average hydrostatic residual stress of approximately zero for the entire local region, however, as the maximum positive and negative values are nearly equal. This pattern continues until 4% to 7% retained austenite, where previously it was shown that significant portions of the austenite become susceptible to transformation. At initial volume fractions above this portion, we see a shift in the magnitude difference between the positive and negative maximum values, with the negative (compressive) maximums becoming much larger. The average value also becomes compressive, as is expected because the transformation of retained austenite causes a volume expansion, thereby compressing grains adjacent to high-transformation areas.

Of importance in this demonstration case is that the polycrystalline structure leads to localized plastic strain accumulation in regions that are not necessarily immediately adjacent to the inclusion. For the 4145 (0% RA) case, the inclusion is the primary stress riser as indicated by the patterns in Figure 82 and Figure 86. For the retained austenite cases (Figure 83, Figure 84, Figure 87 and Figure 88), localized transformations cause much more distributed residual stresses, due to the inhomogeneity in the transformation fields. Transformation of the retained austenite increases the heterogeneity of the residual stress field, and it also tends to have a blunting effect on the inclusion's ability to induce plastic strain accumulation. The high residual stresses imposed by the volume fractions transformed does nevertheless raise the fatigue indicator parameters (ERPSI and

Fatemi-Socie parameter) to higher values than when the steel is fully martensitic and the inclusion is the primary driver for fatigue crack nucleation.

This is a key finding of the demonstration case. The increased presence of retained austenite gives way to higher fatigue indicator parameter values and thus lower relative fatigue life, due to the presence of the large volumetric expansion strain of transformation which occurs during the rolling contact fatigue passes. Previous numerical models for rolling contact fatigue have not been able to demonstrate this, though historical data does find a correlation between increased retained austenite and reduced bearing component life [11].

The fatigue indicators examined, ERPSI and the Fatemi-Socie parameter, exhibit similar patterns in both the maximum value and average value curves against initial retained austenite, as seen in Figure 71 and Figure 75. This indicates that ratcheting and cyclic plastic drivers both contribute significantly, and are both effective measures of the microstructures' effect on relative performance when studying volume fraction effects, as in this demonstration.

CHAPTER 5: CONCLUSIONS

5.1 Advances and Innovations

The approach presented here is designed to determine the relative rolling contact fatigue performance as a function of microstructural attributes. Several challenges were addressed. First, fully three-dimensional finite element modeling allows for end effects to be captured that were not previously possible with two-dimensional plane-strain models. This additional capability provides for a more realistic assessment of inclusion morphology and arbitrary orientations.

Due to the nature of the volume-element model, the fatigue indicator parameters can be efficiently calculated for inclusion concentrations at a given depth within the bearing race. By modeling the cyclic deformation in detail only near the inclusion, much computational time can be saved over larger finite element models that include material up to the surface. The prescribed traction boundary conditions, based on the subsurface stress state, can be calculated for any arbitrary orientation by matrix rotation, thus giving the user the ability to mesh only once for a given inclusion shape, and alter the traction conditions to simulate different depths and orientations of the inclusion. The demonstration case in Section 4.1 has given the effect of out-of-plane inclusion orientation on relative fatigue performance, which was previously unattainable with two-dimensional finite element models.

Two crystal plasticity models were developed: a fully martensite model based on quenched and tempered 4145 steel response and a hybrid model that includes both martensite and austenite phases with additional internal state variable to track the volume fraction of retained austenite. By accounting for stress-assisted transformation of the volume fraction evolution of the retained austenite, the residual stress state due to the inelastic transform strains are accounted for and their effect on subsequent accumulation of the cyclic plastic strains is determined. Thus, important links between the initial volume fraction of retained austenite and fatigue indicator parameters (and thus relative fatigue performance) considering initial phase distributions can be drawn with this approach. The demonstration case in Section 4.2 highlights the utility of this material model. It was shown that increased amounts of initial retained austenite caused higher accumulations of plastic strains, as well as large compressive residual stresses, blunting the effect of the inclusion but inducing higher candidate driving forces for fatigue crack nucleation.

The fatigue indicator parameters examined included a ratcheting-based parameter (ERPSI), as well as a critical-plane approach parameter driven by plastic shear strain amplitude (Fatemi-Socie). Both of these parameters exhibited similar behavior in relation to the microstructural variables in the demonstration cases, indicating that both ratcheting and cyclic behavior are important to the rolling contact fatigue scenarios presented, and both should be examined via the respective fatigue indicator parameters for determination if certain microstructural situations may promote one mechanism of crack nucleation over the other.

5.2 Recommendations for Future Work

Given the highly modular state of the tools developed in this method, the techniques lend themselves to other uses. The dual-phase transform material model can be placed in any geometric problem, and is not unique to the bearing loading case. Other austenitic-martensitic dual-phase steels can be calibrated to use the formulation as well. Such would be the case with gear and TRIP steels, as the two are similar in microstructural nature. The geometric model simulating the rolling contact loading for bearings can similarly be teamed with a completely different material model as needed, for the case of ceramic bearings for example. This is a key feature of this method: its modularity.

Another additional feature that could be added to the material model would be temperature dependence. This could involve alteration of the current parameters as a function of steady-state temperature, and/or inclusion of a thermal expansion deformation gradient in the formulation. For many bearing applications, the service temperature is of primary concern. Thus, if a customer desired to use bearings in a range of temperature environments, the usefulness of altering material parameters based on temperature is quite apparent. This would require further test data for implementation: elevated-temperature tensile and compressive tests would be required to determine the impact of the elevated temperatures on the stress-strain response and material parameters would be re-calibrated based on these curves. Then, relationships could be drawn between the yielding and hardening parameters in order to make them a function of the service temperature. In addition, thermal expansion measurements would need to be made to

allow for thermal expansion strains to be introduced into the model as a function of temperature. Inclusion of dependence on temperature could capture the effects of different elastic-plastic behavior of the base metal, the thermodynamic driver for stress-assisted transformation, as well as additional residual stresses caused by the expansion of the bearing material under a temperature increase.

Another microstructural feature which could be examined is carbon content variations with depth, such as that associated with case hardening. A scheme for examining this phenomena is depicted in Figure 90.

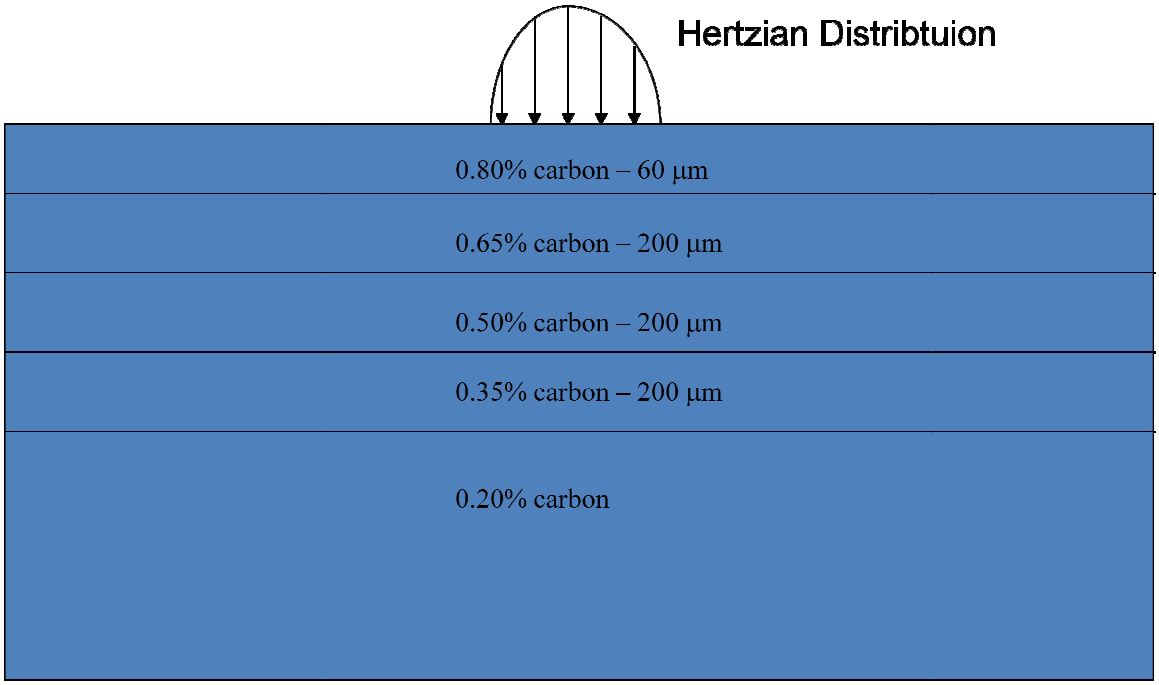

Figure 90. Carbon content variation scheme for possible use with the sub-model.

In order to implement this into the model, material response curves would need to be generated for samples with several carbon contents, with other parameters (such as retained austenite) being kept as consistent as possible. The material model would then be fit to each of the curves, noting the adjustments necessary in the material parameters.

Comparison of this data and how the carbon content affects the yielding and hardening parameters would allow for making these a function of the carbon content, specified as an input in the ABAQUS UMAT.

Within the geometric model, further modifications are possible. One such usage would be for gear loadings and tractive rolling, in which a tangential loading component would be added to the applied traction state. This would be fairly simple to implement, as it involves a further set of singular integral equations added to the stress state already calculated from the normal surface contact. Tests would need to be conducted to determine the effective frictional coefficient between the two contact surfaces, and this parameter would be required as an input in the UTRACLOAD subroutine in ABAQUS. The tractive loads would then be superimposed as boundary conditions along with those caused by normal contact loading.

In addition, an area of interest to examine would be the state of adhesion between the inclusion and the base metal matrix. Currently, studies with this model have used an assumed perfectly-bonded interface between the two regions. However, the geometric finite element model can be adapted to allow for a partially de-bonded inclusion interface, or even a cracked inclusion. Within these de-bonded areas, different frictional characteristics can be applied, from frictionless to rough contact. Thus, the model could aid in determination of the worst-case scenario regarding grain-inclusion interface conditions within the steel.

The influence of texture formed during rolling is another area that could be investigated. As observed by Voskamp [56], the type of texture formed, as a function of loading and temperature, can have a significant effect on spall formation. Creation of a

numerical model to track texture, and whether its formation makes the microstructure less resistant to fatigue, would be of interest to develop.

The many studies and modifications possible with this method of rolling contact fatigue modeling represent a significant contribution to analysis in the field, and allow for future studies that further the understanding of the influence of the microstructure of the material on the fatigue performance.

APPENDIX A: MARTENSITIC CRYSTAL PLASTICITY SLIP SYSTEMS

Slip System	$\underset{\sim}{s}_L^{(\alpha)}$ (Slip direction vector in local coordinates) [33]			$\underset{\sim}{m}_L^{(\alpha)}$ (Slip plane normal direction vector in local coordinates) [33]		
1	-0.57735	0.57735	0.57735	0.707107	0.707107	0
2	0.57735	-0.57735	0.57735	0.707107	0.707107	0
3	0.57735	0.57735	0.57735	0.707107	-0.70711	0
4	0.57735	0.57735	-0.57735	0.707107	-0.70711	0
5	0.57735	0.57735	-0.57735	0.707107	0	0.707107
6	-0.57735	0.57735	0.57735	0.707107	0	0.707107
7	0.57735	0.57735	0.57735	0.707107	0	-0.70711
8	0.57735	-0.57735	0.57735	0.707107	0	-0.70711
9	0.57735	0.57735	-0.57735	0	0.707107	0.707107
10	0.57735	-0.57735	0.57735	0	0.707107	0.707107
11	0.57735	0.57735	0.57735	0	0.707107	-0.70711
12	-0.57735	0.57735	0.57735	0	0.707107	-0.70711
13	0.57735	0.57735	-0.57735	0.408248	0.408248	0.816497
14	0.57735	-0.57735	0.57735	-0.40825	0.408248	0.816497
15	-0.57735	0.57735	0.57735	0.408248	-0.40825	0.816497
16	0.57735	0.57735	0.57735	0.408248	0.408248	-0.8165
17	0.57735	-0.57735	0.57735	0.408248	0.816497	0.408248
18	0.57735	0.57735	-0.57735	-0.40825	0.816497	0.408248
19	0.57735	0.57735	0.57735	0.408248	-0.8165	0.408248
20	-0.57735	0.57735	0.57735	0.408248	0.816497	-0.40825
21	-0.57735	0.57735	0.57735	0.816497	0.408248	0.408248
22	0.57735	0.57735	0.57735	-0.8165	0.408248	0.408248
23	0.57735	0.57735	-0.57735	0.816497	-0.40825	0.408248
24	0.57735	-0.57735	0.57735	0.816497	0.408248	-0.40825
25	0.57735	0.57735	-0.57735	0.267261	0.534522	0.801784

26	0.57735	-0.57735	0.57735	-0.26726	0.534522	0.801784
27	-0.57735	0.57735	0.57735	0.267261	-0.53452	0.801784
28	0.57735	0.57735	0.57735	0.267261	0.534522	-0.80178
29	0.57735	-0.57735	0.57735	0.267261	0.801784	0.534522
30	0.57735	0.57735	-0.57735	-0.26726	0.801784	0.534522
31	0.57735	0.57735	0.57735	0.267261	-0.80178	0.534522
32	-0.57735	0.57735	0.57735	0.267261	0.801784	-0.53452
33	0.57735	0.57735	-0.57735	0.534522	0.267261	0.801784
34	0.57735	-0.57735	0.57735	-0.53452	0.267261	0.801784
35	-0.57735	0.57735	0.57735	0.534522	-0.26726	0.801784
36	0.57735	0.57735	0.57735	0.534522	0.267261	-0.80178
37	0.57735	-0.57735	0.57735	0.534522	0.801784	0.267261
38	0.57735	0.57735	-0.57735	-0.53452	0.801784	0.267261
39	0.57735	0.57735	0.57735	0.534522	-0.80178	0.267261
40	-0.57735	0.57735	0.57735	0.534522	0.801784	-0.26726
41	-0.57735	0.57735	0.57735	0.801784	0.267261	0.534522
42	0.57735	0.57735	0.57735	-0.80178	0.267261	0.534522
43	0.57735	0.57735	-0.57735	0.801784	-0.26726	0.534522
44	0.57735	-0.57735	0.57735	0.801784	0.267261	-0.53452
45	-0.57735	0.57735	0.57735	0.801784	0.534522	0.267261
46	0.57735	0.57735	0.57735	-0.80178	0.534522	0.267261
47	0.57735	0.57735	-0.57735	0.801784	-0.53452	0.267261
48	0.57735	-0.57735	0.57735	0.801784	0.534522	-0.26726

APPENDIX B: AUSTENITIC TRANSFORMATION SYSTEMS

Transform System	$\hat{\underset{\sim}{b}}_L^{(\alpha)}$ (Transformation direction vector in local coordinates) [50]			$\underset{\sim}{n}_L^{(\alpha)}$ (Habit plane normal vector in local coordinates) [50]		
1	-0.1906	0.6311	-0.7520	0.1711	-0.5666	-0.8060
2	0.1906	-0.6311	-0.7520	-0.1711	0.5666	-0.8060
3	-0.6311	0.1906	-0.7520	0.5666	-0.1711	-0.8060
4	0.6311	-0.1906	-0.7520	-0.5666	0.1711	-0.8060
5	0.1906	0.6311	-0.7520	-0.1711	-0.5666	-0.8060
6	-0.1906	-0.6311	-0.7520	0.1711	0.5666	-0.8060
7	-0.6311	-0.1906	-0.7520	0.5666	0.1711	-0.8060
8	0.6311	0.1906	-0.7520	-0.5666	-0.1711	-0.8060
9	-0.1906	-0.7520	0.6311	0.1711	-0.8060	-0.5666
10	0.1906	-0.7520	-0.6311	-0.1711	-0.8060	0.5666
11	-0.6311	-0.7520	0.1906	0.5666	-0.8060	-0.1711
12	0.6311	-0.7520	-0.1906	-0.5666	-0.8060	0.1711
13	0.1906	-0.7520	0.6311	-0.1711	-0.8060	-0.5666
14	-0.1906	-0.7520	-0.6311	0.1711	-0.8060	0.5666
15	-0.6311	-0.7520	-0.1906	0.5666	-0.8060	0.1711
16	0.6311	-0.7520	0.1906	-0.5666	-0.8060	-0.1711
17	-0.7520	0.1906	-0.6311	-0.8060	-0.1711	0.5666
18	-0.7520	-0.1906	0.6311	-0.8060	0.1711	-0.5666
19	-0.7520	0.6311	-0.1906	-0.8060	-0.5666	0.1711
20	-0.7520	-0.6311	0.1906	-0.8060	0.5666	-0.1711
21	-0.7520	-0.1906	-0.6311	-0.8060	0.1711	0.5666
22	-0.7520	0.1906	0.6311	-0.8060	-0.1711	-0.5666
23	-0.7520	0.6311	0.1906	-0.8060	-0.5666	-0.1711
24	-0.7520	-0.6311	-0.1906	-0.8060	0.5666	0.1711

REFERENCES

[1] ABAQUS, 2005, Hibbitt, Karlsson, and Sorensen, Inc, Providence, Rhode Island, v 6.5.

[2] Ahmed, R., 2002, "Rolling Contact Fatigue," ASM Handbook, RJ Shipley and WT Becker, eds., ASM International, 11 6E , pp. 941–956.

[3] Ambrico, J., and Begley, M., 2000, "Plasticity in fretting contact", Journal of the Mechanics and Physics of Solids, **48**, 2391.

[4] Araujo, J., et al., 2004, "The use of Multiaxial fatigue models to predict fretting fatigue life of componenets subjected to different contact stress fields", Fatigue Fract. Engr. Mater. Struct., **27**, 967.

[5] Asaro, R.J., 1983, "Micromechanics of Crystals and Polycrystals," *Advances in Applied Mechanics*, Vol. 23, San Diego: Academic Press.

[6] Becker, P., 1981, "Microstructural Changes Around Non-Metallic Inclusions Caused by Rolling Contact Fatigue of Ball Bearing Steels", Metals Technology, Vol. 8, No. 6, 234.

[7] Bhargava, V., et al., 1985, "An Elastic-Plastic Finite Element Model of Rolling Contact", Journal of Applied Mechanics, Vol. 52, 67.

[8] Bhattacharyya, S., Ghosh, S., and Rattan, G., 2000, "Effect of Pre heat Treatment and Quenching on the Quality Characteristics of SAE-52100 Bearing Steel.

[9] Christ, H., et al., 1992, "Fatigue Behavior of Three Variants of the Roller Bearing Steel SAE 52100", Fatigue Fract. Engr. Mater. Struct., Vol. 15, No. 9, 855.

[10] Courbon, J., et al., 2003, "Influence of inclusion pairs, clusters, and stringers on the lower bound of the endurance limit of bearing steels", Tribology International, **36**, 921.

[11] Damm, E., Sawamiphakdi, K., Glaws, P., and Wilmer, M., Verbal Communications, Timken Research Center.

[12] Date, H., 2005, "Simple Estimation of Deformation-Induced Martensite in Stainless Steel", Key Engineering Materials, Vol. 297-300 I, 500.

[13] Fatemi, A., and Kurath, P., 1988, "Multiaxial Fatigue Life Predictions Under the Influence of Mean-Stresses", Jnl. of Engineering Materials and Technology, Vol. 110.

[14] Fatemi, A., and Socie, D., 1988, “A Critical Plane Approach to Multiaxial Fatigue Damage Including Out-of-phase Loading”, Fatigue Fract. Engr. Mater. Struct., Vol. 11, No 3., 149.

[15] Fourgeres, R., et al., 2002, “A New Physically Based Model for Predicting the Fatigue Life Distribution of Rolling Bearings”, ASTM STP 1419.

[16] Gall, K. and Sehitoglu, H., 1999, “The role of texture in tension-compression asymmetry in polycrystalline NiTi”, International Journal of Plasticity, 15, 69-92.

[17] Ghosh, G., Olson, G., 1994, “Kinetics of F.C.C. -> B.C.C. Heterogeneous Martensitic Nucleation – I. The Critical Driving Force for Athermal Nucleation”, ACTA Metallurgica et Materialia, Vol. 42, No. 10, 3361.

[18] Goh, C.-H., Wallace, J.M., Neu, R.W. and McDowell, D.L., 2001. Polycrystal Plasticity Simulations of Fretting Fatigue. International Journal of Fatigue 23, Supplement 1, S423- S435.

[19] Goh, C.-H., McDowell, D.L., and Neu, R.W. 2005, “Plasticity in polycrystalline fretting fatigue contacts”, Journal of the Mechanics and Physics of Solids, **54**, 340.

[20] Hallberg, H., Hakansson, P., and Ristinmaa, M., 2007, “A Constitutive Model for the Formation of Martensite in Austenitic Steels Under Large Strain Plasticity”, International Journal of Plasticity, Vol. 23, No. 7., 1213.

[21] Johnson, K.L. 1985, Contact Mechanics, pp. 99-104, Cambridge Univ. Press, Cambridge.

[22] Kabo, E. and Ekberg, A., 2005, “Material Defects in Rolling Contact Fatigue of Railway Wheels – the Influence of Defect Size”, Wear, **258**, 1194.

[23] Kapoor, A., 1994, "A Re-evaluation of the Life to Rupture of Ductile Metals by Cyclic Plastic Strain." Fatigue and Fracture of Engineering Materials and Structures, 17, 201-219.

[24] Karaman, I., Sehitoglu, H., Maier, H., and Balzer, M., 1998, “Stress-State Effects on the Stress-Induced Martensitic Transformation of Carburized 4320 Steels”, Metallurgical and Materials Transactions, 29A, 427.

[25] Kumar, A., et al., 1989, “Elasto-plastic Finite Element Analyses of Two-Dimensional Rolling and Sliding Contact Deformation of Bearing Steel”, Journal of Tribology, Vol 111., 309.

[26] Lamagnère, P., et al., 1996, “Nanoindentation investigation of the Young's modulus of porous silicon,” J. Appl. Phys., 80, 3772.

[27] Lormand, G., Meynaud, P., Vincent, A., Baudry, G., Girodin, D., and Dudrange, G. 1998, “From Cleanliness to Rolling Fatigue Life of Bearings – A New Approach”, ASTM STP 1327, 55.

[28] Lundberg, G. and Palmgren, A., 1947, Dynamic Capacity of Roller Bearings, ACTA Polytechnica, Vol. 1, No. 3, pp 1-50.

[29] Martin, J., et al., 1966, “Microstructural Alterations of Rolling Bearing Steel Undergoing Cyclic Stressing”, Journal of Basic Engineering, 555.

[30] Martin, T., Borgese, S., and Eberhardt, A., 1965, “Microstructure Alterations of Rolling Bearing Steel Undergoing Cyclic Stresses,” ASME Preprint 65-WA/CF-4, presented at the Winter Annual ASME Meeting, Chicago, November 1965.

[31] Mayeur, J.R., McDowell, D.L., and Neu, R.W., 2008, "Crystal plasticity simulations of fretting of Ti-6Al-4V in partial slip regime considering effects of texture." Computational Materials Science, 41, 356-365.

[32] McDowell, D., 2007, “Simulation-based strategies for microstructure-sensitive fatigue modeling”, Materials Science and Engineering, 468.

[33] McGinty, R., 2001, “Multiscale Representation of Polycrystalline Inelasticity”, PhD Thesis, Georgia Institute of Technology, Atlanta, GA.

[34] McGinty, R.D. and McDowell, D.L., 1999, "Multiscale polycrystal plasticity." Journal of Engineering Materials and Technology, 121(2), 203-209.

[35] McGinty, R.D. and McDowell, D.L., 2006, "A semi-implicit integration scheme for rate independent finite crystal plasticity." International Journal of Plasticity, 22, 996-1025.

[36] Melander, A., 1997, “A finite element study of short cracks with different inclusion types under rolling contact fatigue load”, Int. Journal of Fatigue, Vol. 19, No. 1, 13.

[37] Morrissey, R. J., McDowell, D. L., and Nicholas, T., 2001, "Microplasticity in HCF of Ti-6Al-4V." International Journal of Fatigue, 23(Suppl. 1), S55-S64.

[38] Murakami, Y. and Endo, T., 1980, ``Effect of small defects on the fatigue strength of metals," Int. J. Fatigue 2, 23-30.

[39] Murakami, Y., and Beretta, S., 1999, “Small Defects and Inhomogeneities in Fatigue Strength: Experiments, Models, and Statistical Implications”, AMS **2:2**, 123.

[40] Neu, R.W. and Sehitoglu, H., 1994, "Measurement of Transformation Strain During Fatigue Testing." In: Automation in Fatigue and Fracture Testing and Analysis, ASTM STP 1231, C. Amzallag, ed., American Society for Testing and Materials, 581-597.

[41] Osterlund, O. Vingsbo, L. Vincent and P. Guiraldenq, 1982, "Butterflies in fatigued ball bearings – formation mechanisms and structure," Scand. J. Metall., 1982, 11, 23–32.

[42] Prasannavenkatesan, R., Zhang, J., McDowell, D. L., Olson, G. B., and Jou, H.-J., 2009, "3D modeling of subsurface fatigue crack nucleation potency of primary inclusions in heat treated and shot peened martensitic gear steels." International Journal of Fatigue.

[43] Raje, N., Sadeghi, F., Rateick, R.G., and Hoeprich, M.R. 2007, "Evaluation of Stresses Around Inclusions in Hertzian Contacts Using the Discrete Element Method", Journal of Tribology, **129**, 283.

[44] Ringsberg, J., et al, 2000, "Prediction of Fatigue Crack Initiation for Rolling Contact Fatigue", Int. Journal of Fatigue, **22**, 205.

[45] Sakai, T., 2006, "Crack Initiation Mechanism of Bearing Steel in Very High Cycle Fatigue", 16th European Conference of Fracture.

[46] Sauger et al., 2000, "Tribologically transformed structure in fretting", International Journal of Solids and Structures Vol. 45, No. 16, pp 4562-4573.

[47] Socie, D., 1987, "Multiaxial Fatigue Damage Models", Journal of Engineering Materials Technology, **109**, 293.

[48] Socie, D., 1993, "Critical Plane Approaches for Multiaxial Fatigue Damage Assessment", Advances in Multiaxial Fatigue, ASTM STP 1191, 7.

[49] Stringfellow, R., Parks, D., and Olson, G., 1992, "A Constitutive Model for Transformation Plasticity Accompanying Strain-Induced Martensitic Transformations in Metastable Austenitic Steels", ACTA Metallurgica et Materialia, Vol. 40, No. 7, 1703.

[50] Suiker, A., and Turtletaub, S., 2005, "Computational modelling of plasticity induced by martensitic phase transformations", Int. J. Numer. Meth. Engineering, 63, 1655–1693.

[51] Tjahjanto, D., Turtletaub, S., Suiker, A., and Van Der Zwaag, S., 2006, "Modelling of the Effects of Grain Orientation on Transformation-Induced Plasticity in Multiphase Carbon Steels", Modelling and Simulation in Materials Science and Engineering, Vol. 14, No. 4, 617.

[52] Turtletaub, S., Suiker, A., 2006, “Grain Size Effects in Multiphase Steels Assisted by Transformation-Induced Plasticity”, International Journal of Solids and Structures, Vol. 43, No. 24, 7322.

[53] Vincent, A., 1998, “From White Etching Areas around Inclusions to Crack Nucleation in Bearing Steels under Rolling Contact Fatigue,” Bearing Steels: Into the 21st Century, ASTM STP 1327, pp. 109-123.

[54] Vincent, A., Lormand, G., Girodin, D., Elghazal, H., Hamnel, A., 2002, “Local elasto-plastic properties of bearing steels determined by nano-indentation measurements”, ASTM Special Technical Publication, n **1419**, 427.

[55] Voskamp, A.P., 1985, "Material Response to Rolling Contact Loading." Journal of Tribology, 107, 359-366.

[56] Voskamp, A. and Mittemeijer, E., 1996, “Crystallographic Preferred Orientation Induced by Cyclic Rolling Contact Loading”, Metallurgical and Materials Transactions, Vol. 27A, 3445.

[57] Voskamp, A., 1998, “Fatigue and Material Response in Rolling Contact,” Bearing Steels: Into the 21st Century, ASTM STP 1327, J.J.C. Hoo and W.B.Green, Eds., American Society for Testing and Materials, pp. 152-166.

[58] Wells, M. et al., 1999, “Rolling Contact Fatigue Behavior of Pyrowear 675”, Surface Engineering, Vol. 15, No. 4, 321.

[59] Zhang, M., 2007, “Crystal Plasticity Modeling of Ti-6Al-4V in Cyclic and Fretting Fatigue Analysis”, PhD Thesis, Georgia Institute of Technology, Atlanta, GA.

[60] Zhang, M., Neu, R.W., and McDowell, D.L., 2009, "Microstructure-sensitive modeling: Application to fretting contacts," International Journal of Fatigue, submitted for review.

[61] Zhang, J., Prasannavenkatesan, R., Shenoy, M. M., and McDowell, D. L., 2009, "Modeling fatigue crack nucleation at primary inclusions in carburized and shot-peened martensitic steel." Engineering Fracture Mechanics, submitted for review.

VITA

Erick Shaw Alley was born in Libertyville, IL on 20 June 1980. After moving a few times early in life as part of a Navy family, he spent most of his childhood years growing up in Charleston, SC. He attended the University of South Carolina, Columbia, earning a Bachelor of Science in Mechanical Engineering in 2002, and a Masters in Mechanical Engineering in 2003. After a period of full-time employment in the defense sector, he came to the Georgia Institute of Technology for pursuit of a Doctor of Philosophy degree in Mechanical Engineering.

Outside of his academic interests, Erick is an avid outdoor recreation enthusiast, and enjoys SCUBA, rock climbing, and camping. Erick is an SSI Master Diver, and also enjoys flying general aviation aircraft.